AFML-TR-66-249

UNCLASSIFIED

AN EXPERIMENTAL INVESTIGATION OF DYNAMIC CRACK PROPAGATION IN PLASTIC AND METALS

Wayne Metcalf Beebe
California Institute of Technology

Technical Report AFML-TR-66-249

JUNE 1966

Graduate Aeronautical Laboratories
California Institute of Technology
Pasadena, California

UNCLASSIFIED

AFML-TR-66-249

AN EXPERIMENTAL INVESTIGATION OF DYNAMIC CRACK PROPAGATION IN PLASTIC AND METALS

Wayne Metcalf Beebe
California Institute of Technology

Technical Report AFML-TR-66-249

JUNE 1966

Air Force Materials Laboratory
Research and Technology Division
Air Force Systems Command
Wright-Patterson Air Force Base, Ohio

FOREWORD

The experimental work described in this report was sponsored by the U. S. Air Force Materials Laboratory, Wright-Patterson Air Force Base, under Contract AF 33(615)-2186, Project 7350, "Kinetics of Metal Fracture." The cooperation and support of Dr. P. K. Dai, Cognizant Program Scientist, is greatly appreciated. The report describes crack propagation experiments with plastic and metal. A high speed framing camera, which was developed under a previous Air Force Contract, was employed in certain phases of the program.

Many individuals have contributed to this project, which was conducted under the general supervision of Professor M. L. Williams. Professor E. E. Sechler contributed many helpful suggestions. The complex electronic system in the high speed camera and in the control and recording equipment associated with the experiments were designed by M. E. Jessey. R. D. Luntz, C. A. Hemphill and E. Mead assisted in many phases of the experimental work. Mrs. E. Fox and Mrs. R. Duffy were responsible for typing the manuscript. The Aeronautics Machine Shop under the supervision of G. Carlson machined the specimens and fabricated all of the special equipment.

ABSTRACT

Crack propagation experiments were conducted in polyester resin sheets containing a central crack. Uniaxial tension loading at several loading rates was applied perpendicular to the crack direction. Two types of experiments were conducted: (1) High loading rate tests at 24°C and -45°C, with a constant loading rate to study the acceleration characteristics of cracks running in a glassy material, and (2) high temperature-low loading rate tests to study slow crack propagation when appreciable viscous dissipation could occur.

During crack propagation, full frame photographs were taken of the photoviscoelastic isochromatic patterns and crack tip position at framing rates from 250 to 100,000 frames per second. The principal conclusions were as follows:

1. Even at loading rates exceeding 10^5 psi per sec, isochromatic patterns prior to crack propagation compare closely with static patterns.

2. Constant crack velocities were achieved in the high loading rate tests and it was found that the isochromatic patterns compare closely with the theoretical solution of Broberg.

3. During the crack acceleration period, the experimental data could not be represented adequately by the Berry elastic theory.

4. For the early phase of the slow (viscous) crack growth period, the crack length could be predicted using a simple theory proposed by Schapery and Williams.

Several tests were conducted on silicon-iron metal sheets; it was concluded that the same testing technique can be applied to the study of crack growth in metals.

TABLE OF CONTENTS

TABLE OF CONTENTS (Cont'd)

LIST OF TABLES

LIST OF ILLUSTRATIONS

LIST OF ILLUSTRATIONS (Continued)

LIST OF ILLUSTRATIONS (Continued)

LIST OF ILLUSTRATIONS (Continued)

LIST OF ILLUSTRATIONS (Continued)

1.0 INTRODUCTION

Experimental investigation of crack propagation had its origin with crack velocity studies in glass, using multiple spark, high speed photography (1-3).* With this equipment it was possible to obtain a limited number (usually 4 frames) of micro-second exposures per test. By altering the time spacing between frames and conducting many tests under the same conditions, crack velocity values were obtained as a function of material constituents, applied stress, temperature and composition of ambient atmosphere. For each type of glass there was a range of applied stress over which the crack length versus time data indicated high acceleration to a terminal velocity (constant limiting velocity). The crack propagation time interval from initiation to the time value at which terminal velocity was reached was much less than 1.0 second. The terminal velocity was independent of the applied stress level, but it was affected by changes in chemical composition of the glass.

Other studies, using different experimental techniques, revealed that at low applied stress levels, with a proper choice of initial crack length, slow crack propagation (low velocities) could be produced with an acceleration time up to terminal velocity ranging from 0.5 to 10^6 seconds. In each of these cases, as the crack elongated, the crack velocity increased, until a value of approximately 10 mm. per second (0.4 inches per second) was reached, at which time the acceleration increased rapidly and terminal velocity was achieved

---

* Numbers enclosed in parentheses are reference numbers.

in a fraction of a second. The details of the velocity variations at this instability condition were not accurately defined because of the nature of the experimental equipment, but the existence of the instability was established. Over the entire range of applied stress levels (a range of 6 to 1) the terminal velocity was constant. These results indicate that crack velocity is affected by the stress at the crack tip until a particular combination of local stress and crack velocity are reached, at which time the energy transfer rate to the crack tip reaches a limit. Terminal velocity values for the entire range of materials tested varied from 0.20 to 0.37 times the quantity $\sqrt{E/\rho}$. ($\sqrt{E/\rho}$ is the uniaxial wave speed.)

Crack velocity values have been obtained in plastic materials by several investigators. Polymethylmethacrylate (Plexiglas) was tested by Schardin (2) and by Williams, et al. (5). The photoelastic material CR-39 (Columbia Resin) was investigated by Wells and Post (4). Schardin, and Wells and Post used multiple spark photography, and Williams used a special high speed camera developed at GALCIT.* All of these investigators obtained some information during the acceleration phase of crack propagation in the plastic material. Wells and Post, and Williams, obtained both velocity data and photographs of photoelastic isochromatic patterns during the crack run. In all of these investigations narrow sheet specimens were used, in which, at certain crack lengths, the isochromatic patterns were affected by the boundaries. In the tests by Williams

---

* GALCIT is an acronym for the Graduate Aeronautical Laboratories of the California Institute of Technology.

small specimens were used and a shock type loading was applied. Schardin, and Wells and Post employed a low loading rate. The effect of boundary conditions and the type of loading on the results of this investigation are unknown. All of these tests on plastic materials were conducted at one temperature. Each investigator used only one loading rate.

In the tests on plastic materials, as in the studies of glass, terminal velocity values were reached which appeared to be independent of stress level. At relatively high failure stress levels, the acceleration values were somewhat lower than those obtained in glass.

Various experiments have been conducted on metal to determine fracture velocities (6-8). In each of these cases, thick plates were used, the specimen was preloaded, and crack propagation was initiated with a wedge driven into an initially machined slot. In some of these investigations the specimens were sufficiently large that, during a portion of the crack run, the stress field in the vicinity of the crack was not affected by boundaries. A terminal velocity value was reached which appeared to be constant, independent of applied stress level, similar to the results obtained for glass and plastic.

A preliminary investigation was conducted by Beebe, et al., in which thin sheet specimens of several annealed metals (aluminum, silicon iron, and plain carbon steel) with central slots, were loaded at a slow rate to fracture. Slow crack propagation was produced after extensive plastic yielding over the entire specimen surface.

The crack propagation was very discontinuous and remained slow over the full width of the specimen (approximately 6.5 inches, half crack length centrally slotted specimens).

The basic conclusions which can be reached from the previous investigations on crack propagation in metals and plastic are the following:

1. If a sufficiently large plastic or metal specimen, with an initial crack, is loaded to a high stress level prior to initiation of the crack run, the crack elongation will exhibit high acceleration to a terminal velocity which is independent of applied stress level. For all of these materials, the terminal velocity values range from 0.15 to 0.40 times $\sqrt{E/\rho}$. Silica glass approaches the value of 0.40, but there are other types of glass, plastics, and metals, which have values in the neighborhood of 0.20. In the quantity $\sqrt{E/\rho}$, $\underline{E}$ is the elastic modulus (for plastics the glassy modulus) and $\underline{\rho}$ is the density.

2. In all of these materials, slow crack propagation can be produced at low stress levels. In the studies on glass at low applied stress levels, the crack velocity is low. As the crack propagates, the velocity increases until a value is reached at which an instability condition sets in. At this condition, there is an increase in acceleration which produces a rapid velocity increase to the terminal value. The terminal value is the same as the velocity achieved at higher stress levels and is independent of applied stress.

3. Glass is the only material which has been studied over a wide temperature range and under different atmospheric conditions. At low propagating velocities, the velocity values for tests in air

are considerably lower than the values obtained in a vacuum. The terminal values, however, for tests in air and in vacuum are the same. The terminal velocity decreases very slightly as the temperature increases. A typical value for the temperature gradient is -0.15 meters per second per degree Centigrade in the temperature range of -190°C to 200°C.

Several theoretical treatments of the crack propagation problem are contained in the literature. These include reports by Mott (10), Roberts and Wells (11), Berry (12), Schapery and Williams (13), and Williams (14). The first three reports relate to elastic material and are based on an energy approach to the crack propagation problem. This energy approach is an extension of the energy method used by Griffith (15). In essence, the work done on the specimen is equated to the sum of the elastic strain energy, the kinetic energy and the surface energy. As the crack propagates, the surface energy increases, and the assumption is made that the energy required to create new surface is obtained from the strain energy and kinetic energy. Mott obtained an expression for kinetic energy using dimensional analysis. Roberts and Wells used the basic assumptions of the Mott analysis and made a further assumption that the dynamic stress field at any instant of time during the crack run was equivalent to the static stress field in a plate with a crack of the same length. Using a solution for the static stress field generated by Westergard (16), they calculated an expression for the kinetic energy and obtained a value for the undetermined constant in the Mott dimensionless analysis. They obtained an expression for crack

velocity as a function of crack length and obtained a terminal velocity of $0.38\sqrt{E/\rho}$.

Berry revised the equations used by Mott, and Roberts and Wells. He used the kinetic energy expression generated by Mott, but obtained new equations for the work done and the strain energy by using energy expressions obtained by Griffith from the original stress field analysis by Inglis (17). Berry obtained equations for acceleration and velocity as a function of crack length and for crack length as a function of time for a fixed force loading condition and a fixed displacement loading condition. An elasto-static stress field was assumed.

Schapery and Williams (13,14) studied crack propagation at low velocities in viscoelastic material. In the first paper, an analysis method similar to that used by Berry was employed. The assumption was made that the kinetic energy at low velocities is zero. A viscous dissipation energy term was included and in order to calculate this term it was assumed that the displacements of viscous elements in the viscoelastic model were the same magnitude as the elastic displacements obtained from the static field equations. A modified dimensional analysis approach was used to obtain an expression for the dissipation term, and solutions were obtained for crack velocity and crack extension as a function of time for fixed force, slowly varying force and fixed displacement boundary conditions. In all of the work by Mott, Roberts and Wells, Berry, and Schapery and Williams, a sheet specimen with a central initial crack was assumed. In the recent report by Williams (14), a

treatment is given for a spherical cavity during crack propagation. With this simplified geometry, Williams treats initiation and propagation as a continuous process.

In order to check the validity of the assumptions used in the the theoretical solutions for running crack velocities, it is important to compare measured stress values in the neighborhood of a running crack with the static solutions used in the analyses. It is also important to compare available dynamic theories with both the measured stress values and the static solutions. Static solutions are available for many different types of specimen geometry, initial crack geometry, and different loading conditions at the boundaries for elastic material. These include papers by Westergard (16), Inglis (17), Neuber (18), Sneddon (19), Williams (20), Ang and Williams (21), Paris and Sih (22). All of these papers are associated with infinite plates or sheets (22). Swedlow (23) gives a summary of the pertinent equations relating to cracks in infinite sheets. Dixon (24) has studied the stress field in a cracked plate of finite width. This information is valuable in determining the effect of side boundaries on a finite width specimen.

A number of solutions exist for the stress field around cracks running at constant velocity. These are essentially dynamic solutions at the steady state condition. Yoffe (25) determined the stress field around a constant length crack moving through elastic material at constant velocity. Craggs (26) studied the case of a semi-infinite crack extending at constant velocity. Broberg (27) determined the stresses in an infinite plate with a central crack

extending on both sides at constant velocity. At least two solutions exist for transient problems. Baker (28) studied a semi-infinite crack in an infinite sheet where the crack suddenly appears and grows at constant velocity. He gives the time dependent stress at any point in the specimen from the beginning of stress rise to the time when the stress reaches a maximum value. Ang (29) has analyzed the case of an extensional dislocation (a crack with infinitesimal length) which suddenly appears and travels at constant velocity.

At present there is no treatment in existence for the case of an accelerating crack. Also, there is no dynamic treatment of the stress field in a cracked sheet of viscoelastic material which includes kinetic energy.

The purpose of the present investigation is to obtain detailed information on the acceleration and velocity characteristics of a crack running in a homogeneous, isotropic, viscoelastic material under various temperature and loading rate conditions. By varying temperature and loading rate in the viscoelastic materials, large changes can be produced in the magnitude of internal energy dissipation in the material.

The second purpose is to determine the loci of principal stress difference values (i.e., isochromatic patterns) in the neighborhood of the running crack and study changes in the isochromatic patterns as the crack extends under different temperature and loading rate conditions. The results of these experiments will be compared with the theoretical solutions for the crack acceleration and velocity characteristics and with both static and dynamic solutions

for the stress fields. A limited number of tests was conducted using a metal to determine the applicability of the testing technique developed for the viscoelastic material to studies of crack propagation in metals.

Section 2.0 contains a general summary of the plan for the experiments. Section 3.0 is a description of the apparatus and the test procedure used in the experiment. In Section 4.0, the mechanical and optical properties of the viscoelastic material are discussed. Sections 5.0, 6.0 and 7.0 contain discussions of results in comparison with theoretical solutions. Section 8.0 is a summary of conclusions. The Appendix contains an approximate theory for crack propagation in elastic material which is a generalization of the theory by Berry (12) based strictly on dimensional analysis. A comparison is made between the Berry solution and the generalized dimensional analysis approach in Section 5.0.

The success of this experimental program is based on the use of a special high speed framing camera with associated light source and loading equipment which was developed specifically for this investigation. This equipment is thoroughly described in a previous report (9).

2.0 GENERAL PLAN OF THE EXPERIMENT

2.1 MATERIAL SELECTIONS

Two materials were selected for the experimental program; (1) A viscoelastic material called "Homalite 100", which is a polyester resin polymer manufactured by The Homalite Corporation, Wilmington, Delaware, hereafter called Homalite, and (2) Silicon-iron metal, which is a low carbon silicon steel with approximately 2.5 percent silicon. This material was obtained in the annealed condition. The Homalite material was chosen because of its simple structure. On the molecular level it consists of cross linked polymer chains with a relatively complicated structure, but on a macroscopic scale with magnification of several thousand times, the structure is essentially homogeneous and isotropic. In previous investigations reported in Reference 9, various types of annealed metal were used in preliminary crack propagation studies, but it was soon discovered that structure variables in crystalline metals (such as line, surface and volume dislocations; anisotropy due to crystal structure; the presence of grain boundaries; inclusions; and interstitial elements) cause large additions to the number of variables which must be considered in an experiment. Thus, the simple structure of the plastic material was chosen in order to reduce the number of variables. In addition, Homalite 100 is a photoviscoelastic material with a high optical coefficient. This makes it possible to observe isochromatic patterns under dynamic conditions with relatively simple equipment. A viscoelastic material was chosen so that its properties would be heavily rate dependent, and thus varying

viscous dissipation would occur as the temperature or load-rate changed. This plastic material simulates metal in that it has the same types of energy terms during crack propagation (i.e., elastic, kinetic, surface and a dissipation energy). The dissipation is of a viscous nature, but it simulates dissipation due to plastic flow in metal. Thus, the energy exchanges associated with metal fracture can be studied in principle at least. Homalite 100 is obtainable with close control on thickness and on chemical composition.

Several tests were run using the silicon-iron material to obtain a preliminary comparison between the properties of the Homalite plastic and a typical annealed metal material. These tests were conducted primarily to determine the feasibility of using the testing technique which was employed on the plastic and to indicate similarities between the rate dependent properties of the plastic and a metal. In this way a plan for future experiments using metal materials can be developed.

2.2 SELECTIONS OF SPECIMEN GEOMETRY

Large specimens were used so that initially uniform stress conditions could be established over the specimen except in the local region of the initial crack. The specimen was chosen to be sufficiently large such that the side boundaries would not affect the stress field of the running crack over a reasonable length of crack run. A short initial slot was used so that the initial total flexibility of the plate would be close to a uniform unslotted sheet (24). This allows an accurate determination of dynamic modulus of the specimen during a loading cycle leading to failure of the specimen.

Thus, in general, an attempt was made to produce a specimen which would approximate the conditions of a crack running in an infinite sheet.

2.3 LOADING CONDITIONS

It was decided to design a constant force rate machine which would hold constant force during the crack run because of difficulty in designing a rigid testing machine which would handle large sheet specimens. This required a very soft type force system so that the force would remain constant over a large deflection range. It was desired to have loading rates from 100 psi per second to 2×10^5 psi per second. These rates cover a loading rate range from the common static loading condition to a rate approaching those which can be applied by explosive loading devices. The high loading rate was desired in order to produce conditions in the Homalite material which would give the closest possible approximation to elastic material in the glassy condition.* This approach would result in the best possible comparison with the theoretical solutions for elastic materials and yet would allow the use of a specimen with the largest possible photoviscoelastic constant.

Glass would seem to be a more logical choice than Homalite for specimen material which would approach the elastic condition, but it has a low photoelastic sensitivity (approximately 1/3 of the coefficient for Homalite 100). Even glass has appreciable dissipation

---

* Viscoelastic materials have two elastic moduli: (1) a glassy modulus at short loading times and (2) a rubbery modulus at long time.

as indicated by Marsh (30) so that only an approximation to the purely elastic condition can be achieved with any known material.

The lower loading rates are required at high temperatures when the effect of high dissipation is being studied.

2.4 RECORDED DATA

The following parameters were recorded on each test.

1. Dynamic Force. This quantity is the instantaneous force on the specimen from which a force versus time curve can be plotted and the loading rate can be calculated.

Loading curves are actually plotted in terms of gross sectional stress which is the total load on the specimen divided by the cross sectional area of the specimen at the loading boundary.

2. Dynamic Total Elongation. This quantity is the total instantaneous elongation of the specimen from which a curve of elongation versus time can be plotted and strain rate can be calculated. Using the dynamic force and elongation data, the dynamic modulus can be determined and the instantaneous work done on the specimen can be calculated.

Total elongation is plotted in terms of average strain which is total specimen elongation divided by the specimen length between clamping jaws.

3. Specimen Photographs. Photographic frames were closely spaced in time and thus revealed the instantaneous crack length. Through auxiliary time measurements, a careful determination of the elapsed time from the beginning of the test run was

obtained for each photograph so that crack length versus time data could be generated. Velocity and acceleration versus time and versus crack length were calculated from faired curves through the crack length versus time data. In addition to the picture of the crack, isochromatic patterns appeared on each photograph. These patterns are representations of the loci of principal stress difference. Under test conditions where considerable dissipation occurs, a time lag between the optical patterns and the corresponding stress patterns exists. This time lag must be calculated from optical characterization data.

4. Specimen Temperature. Through the use of a temperature controlled chamber, the specimen temperature was accurately controlled and measured.

2.5 HIGH LOADING RATE TESTS

Tests at high loading rates were conducted in order to produce a near glassy condition in the material. Tests at two widely spaced low temperatures were conducted in order to determine whether small changes in the viscous dissipation at loading rates above 10^5 psi per second would affect the crack acceleration. Most of the tests were conducted at room temperature ($24^{\circ}C$) and corroborative tests were made at $-45^{\circ}C$. At both temperatures the highest possible loading rates were used. With a high loading rate and using the information previously acquired on glass, it was hoped that acceleration to terminal velocity would occur over a small increment in crack length. This would allow a crack run at

constant velocity for a distance sufficient to study stress fields under steady state constant velocity conditions and allow a direct comparison with the solution of Broberg (27). It was also hoped that the acceleration period would be sufficiently long to acquire data which would compare directly with the Berry solution for elastic material.

Both of these aims were accomplished.

2.6 HIGH TEMPERATURE-LOW LOADING RATE TESTS

In this series, the purpose was to produce slow running cracks under conditions of various amounts of viscous dissipation. A temperature of 112°C was chosen after the material properties had been determined at various temperatures and loading rates (i.e., material characterization). This temperature represents a region of high viscous dissipation. A second temperature of 120°C was chosen in order to approximate a nearly rubbery condition where the material would also be elastic. Thus, by using temperature and loading rate as variables, it is possible to look at isochromatic patterns and crack propagation characteristics over the entire range from glassy to rubbery modulus. In the viscous dissipation region, the aim was to compare experimental crack propagation data with the simplified viscoelastic theory by Schapery and Williams (13). A second aim was to obtain detailed information on the transition between low and high velocity regions of crack propagation.

2.7 TESTS WITH METAL

In this series of tests, high loading rates were used. The load was increased to a selected load value and held constant. The rise time to the constant load was made as short as possible (approximating explosive loading rates). It was hoped that well-behaved fast or slow crack propagation could be achieved by varying the magnitude of the load. This aim was accomplished.

3.0 DESCRIPTION OF EQUIPMENT AND TEST PROCEDURE

Overall views of the test equipment are shown in Figures 1 and 2. The basic components of the equipment setup include: a camera; a light source; electronic power supplies and controls for the camera and light source; a loading frame; a temperature control cabinet which surrounds the loading frame; a control unit which supplies temperature regulated air to the control cabinet; a hydraulic loading system; a load measuring system; a specimen deflection measuring system; a camera initiator system; and signal conditioning and recording equipment for load and deflection measurements and for the initiator signals. Two cameras are shown in the figures: the large high speed camera (hereafter called GALCIT Camera), which was used in the high loading rate tests, and the smaller Red Lake Co. "Hycam" camera (hereafter called Hycam Camera) which was used for the high temperature-low loading rate tests.

3.1 SPECIMEN

The basic dimension for the "Homalite 100" specimens were: $0.025 \times 13.5 \times 26.5$ inches (Figure 3). Four of the specimens used for the high temperature tests at $112^{\circ}C$ and $120^{\circ}C$ had widths which varied from 11.5 to 11.75 inches. The reduction in width on these specimens was necessary because of material shortage during the final phases of the experiment. All data are normalized to account for the dimensional variations. A series of 0.625 inch diameter holes (1.0 inch apart) was drilled along a line 1.0 inch from the top and bottom edges. Several crossed lines were

scribed on each specimen at intervals of 2.0 inches. The crosses were blackened with grease pencil. These lines appear in the photographs and establish a scale for distance measurement.

Bolts were inserted through these holes when the specimen was clamped in serrated jaws. A full thickness slot was machined in the center of the specimen with dimensions of 0.06×0.50 inches. The ends of the slots were semicircular. A sharp notch 0.05 deep with a V-angle of 25° was cut in the ends of the slot with a modified hack saw. The resulting slot was then 0.60 inches long with a notch vertex radius of less than 0.005 inches.

The silicon-iron specimen dimensions were $0.013 \times 13 \times 26.5$ inches. The central slot was milled 0.06×0.60 inches and the notches sawed in the end to make the total notch 0.70 inches long. This was necessary because the loads required to initiate crack propagation with a notch 0.60 long exceeded the capacity of the pressurization system in the hydraulic loading device. Several blackened, crossed lines were painted on these specimens at 2.0 inch intervals to establish scale on the photographs. These lines were front lighted with flood lamps, whereas the crack was illuminated with light passing through the crack.

3.2 LOADING FIXTURE

The loading fixture was the same U-shaped frame as described in the camera report (9) (Figures 4, 5 and 6). The specimen was clamped full width (13.5 inches) with serrated jaws at each end (Figure 4). One-half inch bolts spaced 1.0 inch apart

were inserted through clearance holes in one jaw piece and through the holes in the specimen, and then engaged threads in the mating jaw. For the high loading rate tests, the bolts were tightened with a torque wrench in 200 lb.-in. increments until 600 lb.-in. equilibrium torque was applied to each bolt. For higher temperature tests, the maximum bolt torque was reduced to 150 lb.-in. and spring washers were placed under the bolt heads to maintain the lower value of bolt tension. Higher torque at the test temperatures above 100°C resulted in severe deformation of the specimen around the jaws. After each torque increment was applied, stress relaxation occurred around each serration point and the clamping pressure decreased with time. The process of tightening to successively higher torque magnitudes and waiting for relaxation to occur was continued until equilibrium clamping pressures and deflections were reached.

The serrations on the jaws clamped over a distance of 1.5'' at each end of the specimen. The length of the specimen between jaws was then 26.5 - 3.0 = 23.5 inches. Accurate measurements were made during assembly and clamping of the specimen in the jaws to insure that the vertical centerline of the jaws was coincident with the specimen centerline.

As shown in Figure 4, each clamping jaw had a 0.75 inch diameter hole located on the centerline beyond the serrations. The lower jaw set was inserted between two horizontal steel bars which were attached to the upright members of the loading frame. These bars also had a 0.75 inch diameter central hole. A steel dowel pin

(0.75 inch diameter) was passed through the bars and the jaw set. Thus, the lower jaws, and in turn the specimen, had a pin joint attachment to the bottom of the loading frame which was the ground reference for deflections.

The upper jaw set was attached to a steel clevis bar with a steel dowel. Load was applied to the upper jaw set with a hydraulic cylinder which was mounted on the upper horizontal bar of the loading frame. The piston of the cylinder was hollow, so that a load cell and loading rods attached at either end of the cell could pass through the cylinder. This was a device for saving length in the fixture elements. Both loading rods were threaded. A nut was screwed onto the upper rod and the face of the nut rested on the smooth upper face of the hollow piston. The lower load rod screwed into the clevis which was pinned to the upper clamping jaw. When pressurized oil was applied to the cylinder chamber, the piston moved upward and applied force to the nut. This force was transmitted down the load rod, through the load cell, to the upper clamping jaw.

3.3 HYDRAULIC CONTROL SYSTEM

The hydraulic system is shown schematically in Figure 7.

3.3.1 High Loading Rate Tests

The operating procedure for the high loading rate tests was as follows:

1. The valve on the nitrogen cylinder No. 1 and the bleed valve were closed. Both toggle valves were opened and the needle

valve was closed.

2. The valve on nitrogen cylinder No. 2 was opened. The needle valve was then slowly opened and the pressure in the system between the needle valve and the hydraulic load cylinder was increased to a value which represented a small preload on the specimen. The preload was sufficient to take the play out of the mechanical components in the loading system, but not large enough to produce significant creep in the notched specimen.

3. The needle valve was closed and then toggle valve No. 1 was closed. Closure of toggle valve No. 1 was accomplished by tying the toggle arm to the loading frame with a wire. When the toggle arm was not restrained, a spring attached to the arm would pull the arm to the open position.

4. The needle valve was slowly opened and the nitrogen pressure in the accumulator was increased to a value corresponding to the desired maximum test load. The needle valve was then closed.

5. A test was initiated by cutting the tie wire on the arm of toggle valve No. 2. The spring would then rapidly open the valve and allow full test pressure to communicate with the hydraulic cylinder. With this system, it was possible to consistently increase the load on the Homalite specimens from the small preload to 2200 lb. in 11 to 13 milliseconds. The loading rates in the last 3 to 4 milliseconds of the loading period reach values of 400,000 to 530,000 pounds per second (120,000 to 160,000 psi per second). With the silicon-iron specimens maximum loading rates of 612,000 pounds per

second (3.6×10^6 psi per second) were achieved.

6. After the completion of the test, the pressure on the system was released by opening the bleed valve.

3.3.2 High Temperature - Low Loading Rate Tests

The operating procedure for the high temperature tests was as follows:

1. Toggle valve No. 1 was open. This valve was not used in the low loading rate tests. Toggle valve No. 2 was open. The valves on both nitrogen cylinders, the needle valve and the bleed valve were closed.

2. The valve on nitrogen cylinder No. 2 was opened and the needle valve was slowly opened to preload the system. The needle valve and the toggle valve No. 2 were then closed.

3. The valve on nitrogen cylinder No. 1 was opened and this cylinder was filled until it reached a predetermined pressure. The valve on nitrogen cylinder No. 2 was then closed.

4. The needle valve opening was set to control flow from nitrogen cylinder No. 1 at a rate which would produce the desired loading rate at a given specimen temperature. The pressure in nitrogen cylinder No. 1 and the needle valve settings were determined at each test temperature by experimenting with a dummy specimen which did not have a central notch.

5. The test was started by opening toggle valve No. 2 manually (manual operation was adequate because the loading rates were low). With this valve open, the high pressure air in cylinder

No. 2 communicated with the oil-nitrogen accumulator and pressurized the oil in the hydraulic cylinder. Loading rates from 10 to 300 pounds per second (3 to 100 psi per second) were produced with this system. These rates were obtained with the needle valve near the closed position. Thus, higher rates could be achieved, if they had been required, by opening the valve and raising the pressure in the cylinder No. 2. The highest loading rate possible with this system is approximately 2,000 pounds per second.

Load rates between 2,000 and 400,000 pounds per second could be produced in this system by adding a flow control valve in the oil line. This addition was made in some preliminary tests and was successful. Thus it was possible to produce rates from 10 to 500,000 pounds per second on Homalite 100 and 10 to 600,000 pounds per second on steel with this hydraulic loading system. With the exception of a starting transient, approximately constant strain rates were achieved in all of the tests.

6. The system was unloaded by closing toggle valve No. 2 and opening the bleed valve.

3.4 LOAD MEASURING SYSTEM

The load cell was a heat treated steel rod with two crossed flexure sections (Figure 8).

Budd Company foil type, electrical resistance strain gages were mounted at the thin sections of the flexures. Two gages were oriented in the direction of the load axis and two were mounted transverse. The gages were wired together to form a four active

element bridge. The bridge was excited with a D.C. voltage and the output was amplified with an Astrodata Corporation D.C. amplifier (Model Number 885-235). The output from the amplifier was recorded on a Minneapolis-Honeywell "Visicorder" Oscillograph (Model Number 1508) with high frequency galvanometers (Model Number M-1650) which had flat response to 1,000 cps. Two different load cells were used during the experimental program, one for the tests on Homalite 100 and one for the tests on silicon-iron. Both cells were identical except for the flexure thickness which was 0.065 inches for the Homalite cell and 0.25 inches for the silicon-iron cell.

3.5 DEFLECTION MEASURING SYSTEM

The deflection measuring system recorded the actual change in the distance between the two clamping jaws. Since load was applied directly to the upper jaw, if the change in distance between the jaws can be obtained, the total instantaneous input energy can be calculated. This quantity is the area under the load-deflection curve where each point on the curve corresponds to a particular value of time.

The deflection measuring system is shown in Figures 5 and 6. It consists of two identical devices, one for each side of the specimen, in order to detect rotation of the jaws if the deflection varies antisymmetrically across the width of the specimen. Each side had the following components: (1) two mounting brackets which were attached with locating pins and screws to the upper

and lower clamping jaws; (2) a 1.0 inch diameter steel rod, which was screwed into the lower mounting bracket; (3) an Edcliff Instrument Company linear potentiometer (Model Number 3-39-1) attached to the upper mounting bracket with a total extension range of 3.0 inches and resolution of ±0.002 inches; and (4) a flexure link which connected the steel rod to the potentiometer piston. The flexures allowed for small misalignment in the system. The 1.0 inch diameter steel rod provided a means of translating the reference position for deflection measurement from the lower jaw to the end of the potentiometer piston. Two slots (0.25 inch long) were machined in the upper mounting brackets. Two clamping screws were inserted through these slots to threaded holes in the potentiometer case. The slots allowed the potentiometer case to be moved with respect to the piston in order to establish identical zero positions on the two potentiometers. Each potentiometer had two precision slide wires. One slide wire on each unit was connected into a half bridge circuit and the output of each bridge was amplified and recorded on the Visicorder, using the same type of amplifier and galvanometer as described for the load measuring system. One of the extra slidewires was used in the camera initiator circuit.

3.6 OPTICAL SYSTEM

3.6.1 High Loading Rate Tests - Homalite 100

The optical system for the high loading rate tests is shown schematically in Figure 9. It can be seen in the figure that three polaroid wave plates are used. The two adjacent to the specimen

(No. 1 and No. 2) are crossed with axes plus and minus 45° measured from the vertical plane. The polaroid plate in the camera (No. 3) is crossed with respect to polaroid No. 2. The Kerr cell in the camera is a glass container filled with nitrobenzene liquid. Two metal capacitor plates are suspended in the nitrobenzene on electrodes which pass through the wall of the container. When a high voltage pulse is applied to the electrodes the nitrobenzene becomes strongly polarized and acts like a quarter wave plate.

During a test when voltage was applied to the Kerr cell, polaroids No. 2 and No. 3 were effectively uncrossed to allow light to reach the film plane. Polaroids No. 1 and No. 2 must still be crossed when the Kerr cell is pulsed in order to produce dark field photoelastic pictures.

In essence the high speed camera consists of the following components:

1. A camera body in which 10 feet of 35mm film (128 frames) lies stationary in a film track. At the center of the circle formed by the film track is a rotating 45° mirror driven by an air turbine. A magnetic pickup senses the position of the mirror. The optical components shown schematically in Figure 9 are mounted on the front of the camera. When a voltage pulse is applied to the Kerr cell, light passes through polaroid No. 3 to the back lens and in turn to the 45° mirror and onto the film plane. During periods when the Kerr cell is not excited, only leakage light passes through polaroid No. 3. The mirror is rotating at constant speed and when the Kerr cell is excited a frame is formed on the film. Different

time spacing can be established between frames by properly spacing the Kerr cell pulses with respect to the rotational speed of the mirror (i.e., the framing rate is changed). The framing rate is continuously adjustable in the range of 10,000 to 100,000 frames per second. Exposure time can be adjusted from 0.05 to 0.40 microseconds. An exposure time of 0.2 microseconds was used during all of the high loading rate tests.

2. A mercury arc light source which is ignited and operated at a steady state light level prior to a test with a D.C. power supply. During a test when the rotating mirror is in a position to produce one of the 128 frames, the magnetic sensor sends a signal through an electronic control unit and an electronic power supply which applies a high current pulse to the lamp for approximately 3 microseconds. Thus, an intense pulse of light is superimposed on the steady state light level during the formation of each frame. When the light pulse has reached maximum intensity, the electronic controls send a high voltage pulse to the Kerr cell and uncrosses the polaroid system to form a frame. The duration of the Kerr cell pulse is the exposure time. The light source pulses, the Kerr cell pulses, and the position of the rotating mirror are automatically synchronized so that the framing rate is changed merely by changing the speed of the air turbine which rotates the mirror. With all three polaroid axes aligned the maximum light intensity at the film plane during steady state operation was 200 foot candles. This was increased to 10,000 foot candles when pulsed.

3. Electronic power supplies: an air supply system for the

turbine; automatic controls for operating the various synchronized electronic and mechanical systems; a counter for reading framing rate; and various other meters and manual controls for adjusting and controlling the system.

Complete details of construction and operation of the camera and light source are described in the camera report (9). Alterations were made in the Kerr cell and Front Camera Lens Mounts in order to accommodate a shorter focal length lens and to improve the light transmission through the Kerr cell.

Kodak Tri-X and Royal X pan negative films were used during these tests. The quality of the negatives (i.e., contrast and grain size) was essentially the same with the two films. Since the Royal X pan is a faster film this result establishes the fact that the light level at the film plane was adequate to produce good contrast in Tri-X film.

3.6.2 High Temperature-Low Loading Rate Tests

The optical system for these tests is shown in Figure 10. This is a simple polariscope with two crossed polaroids, two quarter wave plates and a commercial high speed camera. The camera is a Red Lake Laboratory (Santa Clara, California) "Hycam" camera (Model Number K20S4E). This camera contains a 400 foot reel of 16mm film and the film is pulled past a prism type rotating shutter. Framing rates from 5 to 11,000 frames per second can be produced with the camera. Timing marks are exposed on the edge of the film. The mercury arc lamp described in Section 3.6.1

was used in this system but only as a steady state light source. Sufficient light was available from the lamp running steady state for all tests. Framing rates varied from 250 to 9,000 frames per second depending on loading rate. Up to 20,000 frames were exposed during each high temperature test so it was possible to accurately record crack length data from which velocities could be determined over a range of 0.01 to 10,000 inches per second in a single test.

Dupont 936A negative film was used for these tests.

3.6.3 High Loading Rate Tests - Silicon Iron

The optical system for the high loading rate tests was identical with the system described in Section 3.6.2 for the High Temperature Tests. The reason for this was that these tests were feasibility investigations to establish the validity of using the test procedure developed for Homalite to study crack propagation at low velocities. It was assumed that the system described in Section 3.6.1 could be used successfully at high crack velocities.

3.7 CAMERA TRIGGER SYSTEM

3.7.1 High Loading Rate Tests - GALCIT Camera

The trigger system included those components which were necessary to open the solenoid operated mechanical shutter in the camera and to initiate the photographic sequence. As described in the earlier report (6), the mercury arc lamp must be ignited and allowed to reach a steady state operation prior to pulsing operations during the photographic sequence. Even with three crossed

polaroids in the optical train enough light leaked through the crossed polaroids to the film to cause objectional fogging in 0.3 seconds. It was necessary, therefore, to have a closed mechanical shutter in the system which could be opened for a period of less than 0.3 seconds while data from a test run was being recorded. A mechanical shutter opening time of 0.2 seconds (200 ms) was selected to allow a safe margin. At the lowest framing rate used in the tests (approximately 15,000 frames/sec.) the total camera run (128 frames) required 8.5 ms. The solenoid shutter required 10 ms to open. Thus, it was required that the initiation signal for solenoid shutter operation must be created in the time interval from 183 ms to 10 ms prior to the initiation of the photographic sequence (i.e., the first Kerr cell pulse).

In order to accomplish this time sequencing, preliminary high loading rate tests to failure were conducted on several specimens. Deflection versus time, and load versus time were recorded during these runs. These trial experiments indicated that the loading rate varied by ±30 percent from a mean value and the load to failure varied by ±7 percent from a mean value. In all cases the loading rate was sufficiently high that the dynamic modulus (stress rate divided by average strain rate) at one test temperature varied by only ±2.5 percent. A variation in failure stress of 7 percent is reasonable considering tolerances in the Homalite properties, in the specimen dimensions, and in the testing conditions. These variations caused the total loading time to failure to vary from 10.5 to 14.2 milliseconds. (Only those tests which had load time to

failure in the range of 12 to 14.2 milliseconds were used for analysis purposes.) During a portion of these preliminary tests a conducting line was applied to the specimen near the notch vertex. Several materials were used for this purpose (copper wire, manganim wire, silver paint and "Aquadag", which is a colloidal suspension of graphite in water). In each case these conductors were connected into an electrical circuit which was designed to produce an electrical pulse when the crack started to propagate and cause the conducting line to fracture. All attempts to use this type of initiator system failed because the fracture of the conductor did not occur when the crack passed the line. The fracture of the conductor occurred in a range of ±30 milliseconds from the time of crack initiation. In some cases the line fractured prior to initiation because a critical strain value in the conductor had been exceeded and in other cases passage of the crack beneath the line did not produce sufficient strain to fracture the conductor. The results for any one of these conducting materials were not predictable. It was not possible to find a conducting material which would properly match the elongation and failure characteristics of Homalite 100.

In all of the final tests the initiator system consisted of the following components:

1. One slidewire of one of the extensometers (potentiometers) connected into a half bridge circuit which had a direct current (d.c.) power supply. As the specimen elongated, the output from this bridge circuit changed.

2. A high response push-pull trigger amplifier (Figure 11)

with biasing networks for adjusting the trigger point to different resistance values corresponding to different specimen deflection values. The trigger point was repeatable to ±0.003 inches of specimen deflection. The trigger signal was a ramp function with a rise time of 10 microseconds and an adjustable flat portion of a few microseconds up to 1 millisecond. The output from this amplifier was recorded on the Visicorder and was also used as an initiator signal.

3. A time delay generator (Dumont Company Model Number 326). The initiator pulse from the trigger amplifier was connected to the time delay generator. The output from this unit could be delayed by any time value up to 10 milliseconds. This interval could be increased by using more than one unit in series (Figure 12). Each generator had an undelayed and a delayed output.

4. The output of the time delay generator was connected to the Solenoid Pulse Relay Chassis which actuated the solenoid in the mechanical shutter in the GALCIT Camera. The operation of this unit is described in the camera report (9).

5. Camera photographic sequence initiator in the GALCIT camera. The operation of this system is explained in Reference 9. When different delay times were required for the mechanical shutter and the camera system, two time delay generators were used. The undelayed output from one unit was connected to the second instrument so that a different time delay could be set on this unit.

Operation of the trigger system consisted of the following steps:

1. The toggle valve was actuated by cutting the restraining wire. When the wire was severed the spring pulled the toggle arm to the open position and the specimen was loaded.

2. When the specimen deflection reached a predetermined magnitude which was determined from the preliminary tests, the trigger amplifier generated a pulse which was recorded on the Visicorder and also sent to the Time Delay Generator. Usually, the undelayed signal from the generator was sent to the Solenoid Pulse Relay Chassis and the mechanical shutter was opened within 10 milliseconds. In a few tests a delayed signal was used to open the shutter.

3. A delayed signal obtained from either the first Time Delay Generator or a second unit connected in series was used to initiate the camera cycle. Delay times were chosen from the data on time to failure in the preliminary tests and were adjusted as new data became available in subsequent test runs. At framing rates in excess of 35,000 frames per second, several tests were required to obtain a test run in which photographs of running cracks were obtained because the time to failure varied by 3.7 milliseconds (i.e., it was a trial and error process). As an example, three tests were required to obtain one successful photographic run at 100,000 frames per second.

3.7.2 Low Loading Rate Tests - "Hycam" Camera

Initiation of the camera cycle for these tests was simple because of the low loading rates. Time to failure was always

several seconds. With 400 feet of film in the camera magazine the photographic cycle was sufficiently long to allow manual operation of the toggle valve in the nitrogen line and manual actuation of the camera with an electrical switch. Time delays, when required, were achieved by using a stopwatch in conjunction with manual actuation.

3.8 TEMPERATURE CHAMBER

The temperature chamber (shown in Figures 1, 2 and 5) was a 1.0 inch thick plywood box which enclosed the U-frame portion of the loading frame. A round opening was provided at the top to allow the hydraulic cylinder to protrude through the box. Openings were provided at the bottom for the two steel upright members. Two round openings were made to couple with the inlet and outlet tubes from an air conditioning unit. Thick rubber gaskets (1/2 inch × 1/2 inch) were glued around the openings to provide air tight seals when the unit was assembled on the loading frame. A portion of the bottom of the box was removable to facilitate assembly around the loading frame, and one complete side was removable to accomplish specimen installation. Two Pyrex glass windows (0.25 × 12 × 13 inches) with an air space between layers were installed in each of two sides of the chamber to allow transmittal of light through the specimen. Temperature regulated air for the chamber was provided by a Missimer, Inc., (Burbank, California) Servo Conditioning Unit, (Model Number PTS-300X-400-LN2) which can generate regulated air from -75°C to +260°C. Below room temperature,

liquid nitrogen was used as a coolant in the Missimer unit. The air was conducted to and from the chamber in heavily insulated flexible tubes (6.0 inches inside diameter). Baffles were installed in the chamber to control circulation paths such that minimum flow velocities were achieved in the region of the specimen. Temperature was automatically controlled from a thermocouple mounted in the air exhaust passage inside the Missimer unit. Temperature in the chamber was monitored with six (6) thermocouples. The thermocouples were connected to a switch and in turn were connected with a cold junction in an ice bath. The output of each thermocouple was measured with a Leeds and Northrop Self Balancing Potentiometer.

Two of the thermocouples were attached to a piece of Homalite 100 (0.25 × 1.0 × 1.0 inches): one was cemented in the bottom of a hole which was drilled to the center of the block and one was attached to the outside surface of the block. The block was loosely attached to the specimen approximately half way between the central notch and the lower jaw. Two thermocouples were taped to the surface of the specimen, one was attached to the upper clamping jaws and one to the lower clamping jaws.

Preliminary surveys at various temperatures indicated that the air throughout the chamber was within $\pm 1.5^{\circ}C$ of a mean value when an equilibrium temperature had been reached. The surface temperature of the specimen was within $\pm 0.5^{\circ}C$ of a mean value under equilibrium conditions to within 1.0 inch of the serrated jaws. The jaw temperature was never more than $3^{\circ}C$ away from the mean surface temperature of the specimen. Equilibrium was assumed to

be established when the temperature inside the Homalite block was within 0.5°C of the surface readings.

At -45°C frosting of the windows occurred. The frost was removed with a specially designed defroster which circulated warm air over the outside window surface. In addition, low pressure heated dry nitrogen was circulated in the gap between the windows. A constricted vent was provided so that positive nitrogen pressure was maintained between the windows.

3.9 TEST CONDITIONS

High loading rate loading tests to failure were conducted at two (2) temperatures: -45°C and 24°C (room temperature). Data from these tests are designated (-45-1) and (24-1). Four (4) tests were conducted at 24°C temperature in addition to the preliminary failure tests which were used to establish the trigger deflection point. Three (3) tests were conducted at -45°C. The temperature chamber was used at -45°C, but the air conditioning system in the laboratory was sufficiently stable to allow tests at ambient temperature to be conducted without the use of the chamber. Temperature in the room was controlled within ±0.5°C over a period of one hour. Low loading rate tests were conducted at 112°C and 120°C. All tests on metal were at room temperature (24°C).

4.0 SPECIMEN MATERIAL CHARACTERIZATION

Mechanical and optical characterization of the Homalite 100 material was accomplished using the test procedures and data reduction methods outlined by Arenz, et al. (31). The data were

obtained in an Instron Testing Machine (Model TTC) with a Missimer, Inc. (Model 2-100X-250) temperature cabinet enclosing the specimens. The specimen had a "dog bone" shape with a central cross section of 0.25×0.50 inches which was constant over a 3 inch length. Tests were conducted over a temperature range of $-95^{\circ}C$ to $+120^{\circ}C$. A special extensometer based on the use of the Moire grid principle was designed and constructed for use in obtaining the effective gage length of the specimen at various temperatures.

The mechanical data are shown in Figures 13 and 14. Figure 13 shows the master relaxation modulus, (E_{rel}), curve which has been constructed by applying a time-temperature shift factor (32) to segments of curves obtained at other temperatures. Also shown in this figure are segments of curves for the temperatures used in the crack propagation tests. The segments extend over the range of interest represented by the total test times at these temperatures.

The time-temperature shift curve is shown in Figure 14. A best fit WLF curve is also included in the figure. The WLF curve (32) is close to the experimental data over the temperature region of $30^{\circ}C$ to $100^{\circ}C$. The rapid decrease in the slope of the curve below $30^{\circ}C$ is somewhat unusual in comparison with viscoelastic materials which are rubbery at room temperature. Some of the hard plastics such as epoxy resins do

show this type of sharp drop off in the shift curve (33).* As indicated by Figure 13 this phenomenon is due to the fact that there is a relatively rapid increase in relaxation modulus as the temperature decreases in the range of low temperatures. At 20°C, the lowest temperature included in the figure, the maximum value of relaxation modulus is 660,000 psi ($(T_o/T)E_{rel}$ = 795,000 for T_o = 352°K). At -95°C, E_{rel} = 848,000 psi ($(T_o/T)E_{rel}$ = 1,675,000 psi, Log (T_o/T) E_{rel} = 6.24). At -95°C, it appears that E_{rel} has approached an asymptote which should be a true glassy modulus. Thus as -95°C is approached the shift factor a_T curve will turn upward and rapidly approach a vertical asymptote.

As can be seen in Figure 14 the experimental shift factors are larger negative values as compared with the WLF curve at temperatures higher than 110°C. This condition is probably due to post curing of the material which is occurring at these temperatures. This conclusion is substantiated by the fact that when the material was held at 120°C for more than 15 minutes, a color change started to occur from clear to a yellowish tint.

Photoviscoelastic data is shown in Figure 15. The quantity $C_{\epsilon_{rel}}$ is the birefringence-strain coefficient and is defined as follows:

$$n(t)_{rel} = C_{\epsilon_{rel}}(t)\,(\epsilon_1 - \epsilon_2)_o$$

---

* All viscoelastic materials have shift factors which are less than the WLF curve values in the temperature range below the glass transition temperature. The glass transition temperature is usually 50°C below the reference temperature. As seen in Figure 14 the experimental curve starts to drop away from the WLF curve at 30°C which is 50°C below the reference temperature of 80°C.

where

$n(t)_{rel}$ = fringe order response to an applied step input of constant principal strain $(\epsilon_1 - \epsilon_2)_0$

$C_{\epsilon_{rel}}(t)$ = relaxation birefringence-strain coefficient

ϵ_1, ϵ_2 = principal strain values

The value of $C_{\epsilon_{rel}}(t)$ plotted in Figure 15 applies to a specimen which is 0.250 inches thick and a monochromatic light source with a wavelength of 5460 Angstroms.

Interpretation of data from other loading inputs is carried out using the general definition of the birefringence-strain relations in their Laplace transform form, e.g., $\overline{n}(p) = C_{\epsilon}(p)[\overline{\epsilon}_1(p) - \overline{\epsilon}_2(p)]$, where one has $C_{\epsilon}(p) = p\overline{C}_{\epsilon_{rel}}(p)$ in which $\overline{y}(p)$ is defined as the Laplace transform of $\overline{y}(t)$. Further analysis details are given in Reference 31. The complete curve could not be obtained because at the lowest test temperature of -95°C the curve showed the first evidence of decrease in slope. The shift factors for the photoviscoelastic data are the same as for E_{rel}.

In addition to the relaxation and photoviscoelastic tests conducted with small tensile specimens, similar data were obtained by conducting load-deflection tests at several loading rates at four different temperatures using a full size specimen (.025 × 13.0 × 26.5 inches) without a central notch. The results from these tests plot on the E_{rel} and C_{ϵ} master curves within the scatter band of the data from the Instron tests. Also, the dynamic modulus obtained by Clark and Sanford (34) for Homalite is within 5 percent of the E_{rel}

data for a corresponding loading time at 24°C. Clark and Sanford also obtained photoelastic constants. The data obtained from the full size specimen tests correlate with their dynamic stress fringe constant within 7 percent for comparable loading rate conditions.

Wave speeds in the Homalite 100 were calculated using the dynamic modulus data at high loading rates and assuming a Poisson's ratio of 0.3. The calculated dilatation wave speed is 87,700 inches per second and the shear wave speed is 48,400 inches per second. In two of the high loading rate tests a shear wave was seen travelling across the width of the specimen after reflection on a side boundary. The measured shear wave velocity was 47,700 inches per second.

5.0 RESULTS OF HIGH LOADING RATE TESTS AND COMPARISON WITH THEORY

5.1 TEST RESULTS

Figures 16 and 17 show the applied stress versus time (i.e., applied load divided by the cross sectional area in a region which does not contain the crack, hereafter called gross sectional stress) and average strain versus time (i.e., total specimen deflection divided by the specimen deflection divided by the specimen length between clamping jaws). There was no evidence of specimen deflection in the jaws so the length between jaws should be an accurate effective length. Data are shown for the two test temperatures of 24°C and 40°C. The difference in fracture stress at the two temperatures does not represent a decrease in strength at the lower temperature because fracture stress at the two temperatures varied by approximately ±7 percent. Each high rate loading curve had a hump just prior to the last straight line segment. This discontinuity in the curve may be due to high frequency electrical noise in the measuring circuitry or it may be associated with a crack initiation phenomena in which the crack elongates by a short, brittle jump, and then holds at this new length for a brief period before further propagation. When the stress wave (dilatation wave) produced by this jump reached the load cell (175 microseconds later), a small decrease in load would occur. This is speculative, but is suggested by the nature of the fracture surfaces at the beginning of propagation.

Figure 18 shows a few typical crack propagation photographs

from a run at 24°C. The circle of light on the photographs represents a distance of 6.5 inches on the specimen. The edge of the specimen is 1.5 inches beyond the circle of light on the right side of the photographs. (The black crosses are exactly 2.0 inches apart.) In frame number 4 of this sequence, the crack is at approximately 0.5 × specimen width. Up to this point the results should not be significantly affected by the side boundary according to Dixon (24). Also, the isochromatic patterns shown in frames 3 and 4 should not be affected by the proximity of the opposite crack tip. Thus, the patterns in these frames should compare directly with the patterns computed by Broberg for an infinite sheet. Branching of the crack is clearly seen in the photographs. Figure 19 shows an overall view of three specimens from the high loading rate tests. Branching has occurred in each specimen, but the branches start at different crack lengths. In all three cases the crack velocity had reached the same constant value of 15,000 microseconds within the first 0.3 to 0.4 inches of the crack run. The gross sectional stress at fracture, however, was different in the three cases as indicated in the figure. Thus, it can be concluded that once the crack has reached terminal velocity, branching is enhanced by increasing the stress level at the crack tip. This is accomplished by producing a higher stress at fracture initiation.

Details of the fracture surface contours are shown in Figure 20. These photographs reveal a continuous change in the nature of the crack as the crack extends. At the notch (frames 1 and 2) curved lines radiate from the notch vertex. The surfaces between the

curved lines are very smooth cleavage faces. In the next two frames, the crack velocity is increasing to the terminal value. In this region, the smooth cleavage faces are interrupted by a few widely spaced lines (cleavage steps), which are roughly in the direction of propagation. These lines appear to be narrow grooves. By the time the crack has reached the region shown in frame number 5, the crack velocity has reached the terminal value. In this picture the narrow lines are closer together and several lines intersect to form "V's". In frames 6, 7, and 8 the grooves multiply and form many more V-shaped irregularities. The surface between the lines becomes progressively more rough. At frame 9 the surface has started to hackle. The hackles are shallow pits with the shape of the V's on the main fracture surface. In frames 10 and 11, large hackles appear and the main crack starts to branch. The surface is very rough and appears feathery.

As can be seen in Figure 18, branching starts with short terminated branches. These appear at random across the thickness of the specimen. None of the starting branches propagates across the full thickness of the specimen. The branches make angles of 20 to 30 degrees with the main path of the crack. Within approximately one inch from the first appearance of branching, the main crack separates into two branches which propagate to the side boundaries of the specimen.

The appearance of the fracture surfaces is characteristic of thermosetting polymers as indicated by tests on epoxy resins by Feltner (35) and on cellulose acetate by Kies, et al. (36). The "V"

pattern in the early stages of the crack run is essentially identical to those seen in cellulose acetate. These patterns appear to be basically different from those which are seen on fracture surfaces of thermoplastic polymers. In the case of the thermoplastic materials, a series of parabolic figures is seen in the crack acceleration region (35, 36). The trailing edges of these parabolas point in the direction of propagation, which is opposite to the direction of the legs of the "V's" in Figure 20. In certain of the thermosetting materials, parabolic figures are seen but the pattern is not regular as it is for thermoplastic materials.

An explanation of these patterns has been suggested by several investigators: (Wolock and Newman (37) present an excellent review of the entire subject of fracture topography.) Kies, et al. (36) proposed the theory that as the primary crack increases in length the stress concentration near the crack tip causes secondary cracks to form at points ahead of the primary crack where imperfections in the material are located. The primary crack has a straight line or slightly curved line front whereas the crack from an imperfection expands with a circular front. The points at which these two crack fronts meet are the loci of conic sections. If the velocities of the two cracks are the same, the intersection is an ellipse. If the circularly expanding crack from the flaw has a lower velocity than the main crack, a closed elliptical figure will be formed. These types of figures can be seen clearly in photographs of fracture surfaces on cellulose acetate (36). A few small elongated elliptical type patterns can be seen in Figure 20b, frame 10. It is suggested by Kies

that the "V" patterns seen on the fracture faces of thermosetting polymers are actually modifications of the elliptical shape where the secondary crack origins are near the intersections of the legs of the "V's". The vertices of the "V's" represent points of extinction of branches of the main crack as it passes by a flaw and reconnects. Kies further states that the lines appear in the photographs because the contours of the primary and secondary cracks are different, so that a slight peak or valley occurs at the lines of intersection of these cracks. The origin of the flaws is not seen in the "V" patterns because the fracture surfaces of the primary and secondary cracks are nearly coincident in this region.

This theory seems to be a reasonable explanation of the experimental facts. In materials where the parabolic patterns occur, the flaw origins can be identified at high magnification.

A concise statement of the prevailing theory which explains the occurrence of hackles and branching phenomena is presented by Andrews (38):

> "The energy available in a large test piece with a small growing crack, per unit increase of its length, is proportional to its length. Thus, as the fracture spreads outwards from its origin it will tend to accelerate in order to utilize the increasing energy supply. There probably exists a limiting velocity for the fracture, low compared with the velocity of sound, and when this velocity is reached by the growing fracture it will become unstable and adopt one method or another of dissipating the excess energy. Deviation of the fracture, branching or oscillation could arise in this way. Possibly all of these occur, but to differing degrees governed by unknown factors."

The energy referred to by Andrews is the strain energy which is a function of $(\sigma c)^2$ where c is the half crack length and σ is the

applied load at the boundary. Thus, if a critical energy value for hackle formation and for branching does exist for each material, an increase in stress level will definitely reduce the crack length at branching. It is obvious that the larger fracture surface area in the hackled region and at the branches does require greater surface energy in their formation. Results shown in Figure 19 generally corroborate this theory. Many additional tests would be required, however, to generate sufficient statistical data to fully substantiate the theory. The test equipment and specimen configuration used in this investigation would be ideal for conducting such an experimental program.

Figure 21 gives crack length versus time data for two high loading rate runs. The inset in the figure gives the details of the acceleration phase of the run. At the high framing rate of 100,000 frames per second achieved by the GALCIT camera, sufficient detail is obtained for this high speed crack propagation to define the acceleration phase. (It should be realized that crack initiation started somewhere in the time interval represented by the frame spacing between the first frame from which data are shown in the figure and the previous frame. The crack could have attained a finite velocity in this interval.) During the constant velocity portion of the run, the data seem to have a periodic wander about the constant velocity line. This may be natural scatter in the data or it may be due to the influence of dilatation and shear waves generated during the early stages of crack propagation and returning to the crack tip after reflecting off the side boundary or thickness faces. The first downward deviation from the constant

velocity line (i.e., at 120 microseconds) compares with the time for a dilatation wave with a speed of 88,700 inches per second to travel approximately 10.5 inches. This is the distance from initial crack tip to the boundary and back to the crack tip, which, after 120 microseconds, has moved to a point two inches from the center of the specimen (or 4.5 inches from the boundary). The second downward deviation is at approximately the correct location for the shear wave (48,000 inches per second) to reflect from the boundary and intercept the crack.

5.2 COMPARISON WITH THEORY

Figure 22 is a comparison between the crack length versus time data and curves predicted by Berry (12). Berry computed acceleration, velocity and crack length expressions for two loading conditions during the crack run: fixed force and fixed displacement. In each case, the load-deflection curve up to the fracture point was linear. The high loading rate experiments described in this report do not correspond exactly with either of these load conditions. In the fixed force condition prescribed by Berry, the specimen elongates during the crack run and energy is added to the specimen. This energy appears as additional strain energy which becomes available for conversion to kinetic or surface energy. In the fixed displacement case, no energy is added during the crack run, so a portion of the strain energy in the plate is converted to kinetic and surface energy. In the present test as shown in Figure 21, the entire crack run up to the time of branching is 300 microseconds (0.3 milliseconds).

A dilatation wave with a velocity 88,700 inches per second takes 265 microseconds to travel from the center of the specimen to the upper boundary and return to the crack line. Thus, the crack acceleration phase and nearly all of the constant velocity phase of the crack run are unaffected by force or deflection changes at the boundaries. This fact gives further credence to the initial assumption that the crack is propagating under conditions which exist in an infinite plate with the load at boundaries which are an infinite distance away from the crack. Therefore, the energy exchange is occurring in the neighborhood of the crack with no influence from the boundaries.

In the fixed displacement loading case, the kinetic and surface energy are obtained from the elastic energy existing in the plate at the time of fracture. The test conditions are closer, therefore, to the fixed displacement case than the fixed force case. For the fixed displacement case, the Berry equation for crack velocity is

$$v_c^2 = \frac{2\pi}{k'} \frac{E}{\rho} \frac{(m+2\alpha^2)}{\alpha^2(m+2)} \left[\frac{(m+2)(\alpha^2-1)}{(m+2\alpha^2)} - n(\alpha-1) \right] \quad (5.2\text{-}1)$$

where:

$$m = \frac{A}{\pi c_o^2}$$

A = plate area

$2c_o$ = initial crack length

$$\alpha = \frac{c}{c_o}$$

$$n = \frac{4E\gamma}{\pi c_o \sigma_c^2}$$

γ = specific surface energy

$\sigma_c = \bar{\sigma}_y$ at the initiation of the crack run

For run number 24-1, m = 1119.

When $\alpha = 1$, $\left(\frac{m+2}{m+2\alpha^2}\right) = 1$ and when $\alpha = 3$ (corresponding to the crack length at which the crack has reached terminal velocity (Figure 21), $\left(\frac{m+2}{m+2\alpha^2}\right) = 0.995$. Consequently, equation (5.2-1) reduces to

$$v_c^2 = \frac{2\pi}{k'} \frac{E}{\rho} \left(1 - \frac{c_o}{c}\right) \left[1 - (n-1) \frac{c_o}{c}\right]$$

or

$$\frac{v_c^2}{v_m^2} = \left(1 - \frac{c_o}{c}\right) \left[1 - (n-1) \frac{c_o}{c}\right] \qquad (5.2\text{-}2)$$

where:

v_m = terminal velocity

This is identical to the Berry equation obtained for the fixed force case. Thus, for the large specimen used in this investigation the same equation represents both the fixed force and fixed displacement conditions to a very close approximation. Figure 22 shows that the data points fall below the curve for n = 1 during the acceleration phase, but match the n = 0.25 curve during the constant velocity phase.

n = 1 corresponds to

$$\gamma = \left(\frac{\pi}{4n}\right) \frac{c_o \sigma_c^2}{E} = 7430 \frac{\text{ergs}}{\text{cm}^2} \left(0.042 \frac{\text{lb-in}}{\text{in}^2}\right)$$

and

$$n = 0.25 \text{ to}$$

$$\gamma = 1857 \text{ ergs/cm}^2 \; (0.011 \; \frac{\text{lb-in}}{\text{in}^2})$$

Under similar conditions, according to Shand (3), glass at terminal velocity has values of γ = 3,000 to 10,000 ergs/cm^2 (0.017 to 0.057 lb-in/in^2) computed on a basis of the Griffith equation (i.e., $\gamma = \pi c_o \sigma_c^2 / 2E$). The value of n in the Griffith equation is 0.5. Independent measurements of surface energy in glass give values of 250 to 300 ergs/cm^2.

The crack length versus time curve in Figure 22 suggests that the acceleration characteristics may be approximated by using a value of n = 1 and the constant velocity phase by n = 0.25. A more detailed study of the crack velocity, however, shows that neither of these values gives a satisfactory approximation to the velocity.

Figure 23 compares the experimental velocity values in run 24-1 with predicted curves, using n = 0.25 and n = 1.0. The n = 1.0 curve is closest to the experimental data in the early stage of propagation and n = 0.25 in the later stage. The match is poor, however, with either curve. The fact that the n = 0.25 curve for crack length versus time closely approximates the experimental data is due to the fact that the initial acceleration in n = 0.25 case is higher than the experimental data (i.e., the theoretical curve rises faster than the experimental curve). Therefore, even though the n = 0.25 velocity curve is lower than the experimental curve for low c/c_o values the velocity curves and the intercept is at c/c_o = 3, the

higher initial velocity causes the crack length versus time curve for $n = 0.25$ to intercept the experimental curve at c/c_o slightly above 2. It should be remembered that all of the theoretical curves for c/c_o versus time have the same final slope (i.e., the same velocity). Equation (5.2-2) indicates that the Berry equation for

$$\frac{v_c^2}{v_m^2(1 - \frac{c_o}{c})} \quad \text{which is equal to } [1-(n-1)\frac{c_o}{c}]$$

should be a series of straight lines for various values of n. Figure 24 is a comparison of the experimental data with the theory over the entire range of crack length values. $c_o/c = 1$ is the beginning of crack propagation and $c_o/c = 0$ is for an infinite crack length. For $c_o/c = 0.45$, the experimental velocity is constant. It can be seen that the experimental data intercepts the theoretical curves for all values of n from $n = 2.0$ to $n = -1.0$ (negative values of n are not acceptable, because they would indicate negative surface energy).

In Appendix I, the Berry theory is generalized on the basis of dimensional analysis. This revised theory does not depend on the assumption of a static stress field, but since it is strictly a dimensional approach to the problem, it includes an unknown function which depends on the nature of the dynamic stress field. Using a series expansion for this unknown function, it is interesting to note that the equation for velocity can be arranged in the same form as the Berry equation:

$$(\frac{v_c}{v_m})^2 = (1 - \frac{c_o}{c}) [a_o + (a_1 - n)\frac{c_o}{c} + a_2 (\frac{c_o}{c})^2 + \ldots] \qquad (5.2\text{-}3)$$

In the Berry equation (5.2-2)

$$a_o = 1,\ a_1 = 1 \text{ and } a_n = 0 \text{ for } n > 1$$

Using the generalized theory, a close match with the experimental data can be obtained during the acceleration phase if

$$a_o = 0.633$$
$$(a_1 - n) = -0.916$$
$$a_2 = 10.833$$

Points on this theoretical curve are plotted in Figure 24, and as shown in the figure, the approximation is valid only from

$$\frac{c_o}{c} = 0.6 \text{ to } 1.0 .$$

To match the velocity curve over the entire range of crack length values requires a minimum of four higher order terms, all with large coefficients. In summary, the Berry theory does not appear to represent the basic nature of the experimental data and, therefore, cannot be used as a prediction method for crack propagation kinetics.

A comparison of experimental and theoretical isochromatic patterns is contained in Figures 25 and 26. Figure 25 illustrates the relationship between the largest fringe shown in Figure 18a frame 1 (left side) and a theoretical isochromatic based on a statically loaded stationary crack (23). This fringe represents the locus of a particular value of principal stress difference, $\sigma_1 - \sigma_2$, at the instant of crack initiation. The match between the experimental and

the theoretical patterns is remarkably close even though the theoretical pattern is based on a fixed (static) load while the loading rate in the test run is greater than 10^5 psi/sec. This result suggests that, during loading prior to crack propagation, the static solution for the stress field is an adequate approximation to the dynamic stress field, even at extremely high loading rates, if the load at the boundary is a smooth function of time.

The magnitude of $(\sigma_1 - \sigma_2)/\bar{\sigma}_y$ on this fringe was determined from an optical material calibration test on a full size, solid specimen (no central slot) in which the same loading rate was used as in the test from which the photographs in Figure 18 were obtained. Values of $dn/d\bar{\sigma}_y$ versus $\bar{\sigma}_y$ were determined from the calibration test (n = fringe order). When the magnitude of $\bar{\sigma}_y$ at crack initiation was multiplied by $dn/d\bar{\sigma}_y$ a value of slightly less than 1 was obtained. This calculation, coupled with a study of changes in the shape of the fringe as revealed by the photographic frames prior to frame 1 shown in Figure 18a, confirmed that the fringe under consideration was the first order dark fringe (the field of the polariscope was dark at zero load, i.e., the zero order dark fringe covered the entire specimen). Returning to the calibration data it was established that the first order dark fringe represented a value of $(\sigma_1 - \sigma_2)/\bar{\sigma}_y = 1.075$. The smaller second order dark fringe in the photographic sequence was therefore a locus of $(\sigma_1 - \sigma_2)/\bar{\sigma}_y = 2.15$.

Figure 26a shows a comparison between the first order dark fringe and the corresponding pattern for a stationary crack in a region where the crack is running at constant velocity. The

experimental data points were taken from Figure 18b, frame 5, where the half crack is running at constant velocity when $c \geq 0.06$. The dotted region on the experimental curve for $(\sigma_1-\sigma_2)/\overline{\sigma}_y = 1.075$ is uncertain because the fringe is outside the field of view of the camera in this region. A study of neighboring frames in Figure 18a indicates, however, that the dotted portion is a close approximation to the actual pattern.

As shown in Figure 26a there is a large difference between the size of the static and the dynamic isochromatics in the specimen area where the stress is close to the applied stress. The size difference is less startling when it is realized that an increase of $(\sigma_1-\sigma_2)/\overline{\sigma}_y$ to 1.2 would reduce the maximum length of the theoretical pattern to one half the length shown for 1.075.

Results close to the crack tip are presented in Figure 26b. Two theoretical curves are shown in this figure: (1) a pattern for a stationary crack with a static load and (2) a pattern for a steady state dynamic stress field obtained from Broberg's solution (27). Broberg solved the problem of a centrally cracked plate in which the crack length is increasing at constant velocity. All transient effects are neglected, so that the solution represents the case in which waves generated during crack initiation and acceleration to constant velocity have passed outside of the area of interest.

For the region near the crack tip the Broberg equations are as follows:

$$\frac{\sigma_1-\sigma_2}{\bar{\sigma}_y} = 2\left[\left[\left\{\frac{MK^2}{2\beta_o^2}\left(\frac{c}{r}\right)^{\frac{1}{2}}\left[\frac{(2k^2-\beta_o^2)(2-\beta_o^2)}{\sqrt{1-\beta_o^2}}F_1(\beta_o,\nu)\right.\right.\right.\right.$$
$$\left.\left.\left.\left. -4k\sqrt{k^2-\beta_o^2}\,F_1\left(\frac{\beta_o}{K},\nu\right) - 0.5\right\}^2\right.\right.$$
$$\left.\left.+\left\{\frac{Mk^2}{2\beta_o}\left(\frac{c}{r}\right)^{\frac{1}{2}}(2k^2-\beta_o^2)\left[F_2(\beta_o,\nu) - F_2\left(\frac{\beta_o}{k},\nu\right)\right]\right\}^2\right]\right] \qquad (5.2\text{-}4)$$

where:

$$F_1(\xi,\nu) = \left[\frac{\sqrt{1-\xi^2\sin^2\nu}+\cos\nu}{1-\xi^2\sin^2\nu}\right]^{\frac{1}{2}}$$

$$F_2(\xi,\nu) = \left[\frac{\sqrt{1-\xi^2\sin^2\nu}-\cos\nu}{1-\xi^2\sin^2\nu}\right]^{\frac{1}{2}}$$

$$\beta_o = \frac{v}{c_d}$$

$$k = \frac{c_r}{c_d}$$

v = crack velocity

c_r = shear wave speed

c_d = dilatational wave speed

$$M = \frac{(1-\beta_o^2)}{g(\beta_o)}$$

$$g(\beta_o) = \{[(1-4k^2)\beta_o^2 + 4k^4]\,K(\sqrt{1-\beta_o^2})$$
$$-\frac{1}{\beta_o^2}\,[\beta_o^4-4k^2(1+k^2)\,\beta_o^2 + 8k^4]\,E\,(\sqrt{1-\beta_o^2})$$
$$-4k^2(1-\beta_o^2)K\left(\sqrt{1-\left(\frac{\beta_o}{k}\right)^2}\right.$$
$$+\frac{8k^4}{\beta_o^2}(1-\beta_o^2)\,E\,\left(\sqrt{1-\left(\frac{\beta_o}{k}\right)^2}\right.$$

where K and E are complete elliptic integrals of the first and second kind.

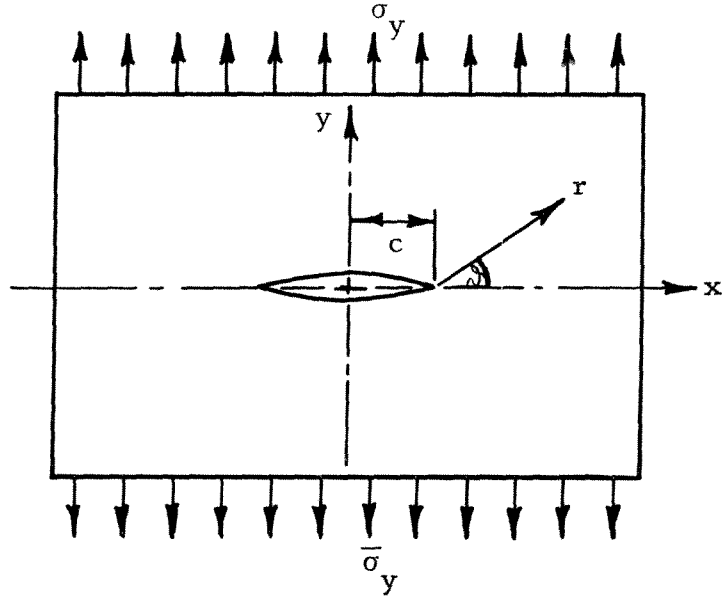

In the case under consideration

v = 15,100 inches/second

c_r = 87,700 inches/second

c_d = 48,000 inches/second

β_o = 0.170

K = 0.534

Before the Broberg equation was used to calculate the shape of an isochromatic, the size of the region around the crack tip for which the equations were applicable was established. This was done by comparing values of $(\sigma_1-\sigma_2)/\bar{\sigma}_y$ at various distances from the crack tip in the limiting case where $\beta_o = 0$ (i.e., v = 0) with the static solution for a stationary crack. The Broberg approximation matched the static solution within ± 0.02 for $c/r > 4.0$. In the case illustrated in Figure 26b, $(c/r) > 4.6$.

Figure 26b shows excellent agreement between the Broberg solution and the experimental data for $(\sigma_1-\sigma_2)/\bar{\sigma}_y = 2.15$. This result indicates that for the case of a constant crack velocity in the region

near the crack tip ($c/r > 4$), the Broberg equations accurately represent the dynamic stress field. The fact that the experimental stresses are close to the static values prior to initiation and that they match the Broberg solution at the terminal velocity condition, suggests that the Broberg solution would give a relatively accurate representation of the stresses during the acceleration period. Data for the acceleration region are available from run 24-1. The second order fringe in this region is small but with special attention to contrast in an enlarging and printing process, adequate information on the shape of the isochromatics probably can be obtained. Also a series expansion of the Broberg equations for small β_o values and further study of the effects of the approximations in the equations is required. This study is necessary because of small differences in the equation for $(\sigma_1-\sigma_2)/\overline{\sigma}_y$ which, even at $\beta_o = 0.17$, cause accuracy problems in the computation. A minimum of seven place accuracy was required in the computations for $\beta_o = 0.17$ in order to obtain 2 percent accuracy in the values of (c/r). The additional analysis for the acceleration region is beyond the scope of this investigation.

6.0 RESULTS OF HIGH TEMPERATURE - LOW LOADING RATE TEST AND COMPARISON WITH THEORY

6.1 TEST RESULTS

Applied loading curves for tests at 112°C (designated 112-1, 112-2, 112-3, 112-4, 112-5, 112-6, and 112-7), and for tests at 120°C (designated 120-1 and 120-2) are contained in Figures 27, 28, and 29. Corresponding average strain curves are contained in Figures 30, 31, and 32. As can be seen in these figures, non-linearities occur in the early part of the loading cycle, but, near the segment where crack propagation occurs, the loading rate is approximately constant. The average strain curves have less irregularity so that it can be stated with good approximation that these tests are constant strain rate tests to fracture. When the crack starts to run, especially at the lower loading rates, there is some upward curvature in the strain curves. This is due to the fact that as the crack elongates the total flexibility of the specimen increases. Solid triangles are located at points on the loading and strain curves where crack propagation is initiated. It will be noticed that these triangles are missing from three of the curves, namely, 112-1, 112-3, and 112-5. In these cases the photographic cycle was started after the crack had propagated for a short distance. A circle is located on these curves at the point where the first photographs were taken. In all of the specimens the initial half crack length was 0.3 inches. In the case of test 112-1 the first pictures were taken at a half crack length of 0.375 inches, for run 112-3 at 0.425 inches, and for run 112-5 at 0.475 inches. Loading rates during

the final portion of the loading curves and the strain curves are shown in insets on each figure. Tests 112-1 through 112-5 represent a strain rate variation of approximately 1.75 to 1. In runs 112-6 and 112-7 an attempt was made to run a constant load test during the time the crack propagated. As can be seen in Figure 28, the curves show approximately constant loading rate during the crack run. The load decreases in each case approximately 5 percent from the value at the initiation point. During this time the strain is increasing because of the elongation of the crack so there is energy addition to the plate during these constant loading rate runs.

Unlike the high loading rate experiments, in these low loading rate tests dilatation or shear waves can travel to the loading boundaries and return to the crack during a time in which the crack has elongated only a very small increment. Thus, work done at the boundaries is communicated to the crack region and these tests are, therefore, representative of constant loading rate and constant force tests.

At 120°C the material approaches a rubbery condition. At this temperature an attempt was made to produce a stable constant velocity running crack at the rubbery (or elastic) condition. This aim was not achieved but extremely low crack velocities were produced so that it can be considered that the condition was approximated.

Crack propagation photographs are shown in Figures 33, 34, 35, 36, and 37. As can be seen, there is some variation in contrast and, therefore, clarity of the isochromatic patterns in these

tests. All of the runs were made using the Hycam camera but different framing rates were used in the various tests and because of the nature of the shutter system in the Hycam camera this resulted in different exposure times from one run to the next. A grainy texture is noted in the spaces between the isochromatic patterns. This is not a representation of surface roughness on the specimen and does not appear to be associated with fine scale strain effects in the Homalite material. Rather it seems to be associated with the optical system in the camera and possibly the film used in these tests. The presence of the graininess does not affect the results because the isochromatic patterns stand out sharply against this background.

In all cases it is not possible in any of these photographs to see the crack tip because of a dark spot at the tip. A study of photographs prior to crack initiation (which are shown only in Figure 37) indicate that the crack tip is located at the center of the dark spot. In measurements of crack length the film was projected using a special slide projector and magnified approximately 20 times. A reference point was established at the center of the smallest isochromatic ring. This point correlated well with the center of the crack at crack initiation. It is estimated that crack length determinations were made to within ± 0.02 inches.

Some asymmetry is shown in the two largest isochromatic patterns at the crack tip. In most of the cases of pronounced asymmetry the largest of the two elongated rings is connected with a dark patch which runs to the boundary of the photograph. This, of

course, means that the stress level in the entire dark region is approximately the same. The asymmetry appears, therefore, when the largest rings reach a position in which they are at approximately the same stress level as the entire surrounding plate. The condition is influenced by the large stress or strain increments between the isochromatic patterns and is a common problem in dynamic photoelastic measurements. This phenomena does not affect the validity of the results as they pertain to the type of analysis being made using these patterns.

In all cases shown in the photographs, the last frame indicates that the crack has propagated completely across the specimen. The next frame previous shows the crack length at a point just prior to the fast crack propagation. The interval of time between these two frames is the reciprocal of the framing rate. In each of these figures the time, t, from the start of crack propagation (or the time from the first frame taken in the sequence) is shown and also the time, t', measured backwards from the instant at which the crack has propagated completely across the plate. These time numbers give a first introduction to an instability phenomena which will be discussed later in this section. In each test there is a period of slow crack propagation where the total crack elongation at low velocity is affected by strain rate and failure load at each temperature, and a period of fast crack propagation with a very sharp discontinuity between these two regions. Figures 34 and 35 show portions of both slow crack propagation and fast propagation. These figures give a strong indication of the viscoelastic nature of the material

at these high temperatures. In frame numbers 8 and 9 in Figure 34 and frame numbers 7, 8 and 9 in Figure 35 the crack is in the region of fast propagation and is shown at various positions across the width of the specimen. A portion of one isochromatic ring is shown on each side of the crack tip. These are faint and somewhat smeared because of the relatively long exposure time of the Hycam camera. The isochromatic patterns in the slow crack propagation region are still clearly visible and appear to interfere somewhat with the pattern in the fast propagation regions. This is due to the fact that these patterns occur in a region where the material is highly viscoelastic and a certain relaxation time is required for the patterns to disappear. This time is much longer than the time necessary for the crack to propagate across the remaining width of the specimen. It was not possible with a single camera to obtain a large amount of detail in the fast crack propagation region and at the same time obtain detail in the low velocity region. Sufficient information is available, however, to define the transition between these regions. In three of the tests several points were obtained in the high velocity region to show the acceleration to the high terminal velocity. The definition of the crack tip location in the high velocity region is less certain than in the low velocity region. It is estimated that in this region the crack tip can be determined within ± 0.15 inches.

Figure 38 is a photograph of the fracture surfaces on two specimens: 112-2 and 112-7. As can be seen from the loading curves, 112-2 has a higher loading rate than 112-7. Run 112-7 is a

constant load test. Also included in the figure is a tabulation of the strain rate and the distance to the discontinuity line. Every specimen tested at 112°C and 120°C with low loading rates had a fracture surface similar to those shown in Figure 38. The shiny area is the region of slow crack propagation and the darker area is the high velocity region. Between the two areas is a sharp discontinuity line.

Details of the fracture surface texture can be seen in the photomicrographs in Figures 38 and 39. At the vertex notch long deep rivulets appear at these high temperatures and low loading rates. The height and the width of the peaks and valleys in these contours are larger at 120°C than at 112°C. (This is not as apparent in the photographs as it is in direct observation through the microscope.) Fine lines, some of which appear to have their origin at the notch vertex, appear on the surface. These lines are similar to the lines which could be seen in the specimen in the high loading rate test; however, in that case the lines did not originate at the notch vertex. These lines are seen in frames 3 and 4 in Figure 39 and frame 4 in Figure 40. The lines are always at an angle with respect to the specimen edge and form a pattern of long slender "V's". As the crack length increases, as indicated in frames 5 and 6 in Figure 39 and frames 5, 6, and 7 in Figure 40, the number of lines multiply and a system of V-shape patterns develops on the surface similar to those which appeared in the high loading rate tests. In this case, however, the surface is considerably smoother, even when a very closely spaced pattern of V's had developed. At the edges of the specimen, the noses of the V-shaped pattern are

turned toward the edges, and near the center of the fracture face, they are approximately parallel to the edges. Along a portion of the edge a faint line parallel to the edge can be seen. Along this line the fracture surface changes slope very slightly. This contour seems to be a faint hint of a shear lip.

In both Figures 39 and 40, a sharp discontinuity line is seen at which the closely spaced V-pattern terminates sharply. On the other side of the discontinuity line, the specimen is smooth. In Figure 39, frame 9, it can be seen that this smooth texture is unchanged as the crack extends beyond the discontinuity line. The texture shown in frame 9 is representative of the specimen surface throughout the remaining length of the crack path. In Figure 40, frame 9, the specimen surface appears to be somewhat rougher on the high velocity side of the transition line. At low magnification on this specimen the discontinuity line appears to be as sharp as in the test at 112^{o}C, but at high magnification it can be seen that the discontinuity is not as sharp as at the lower temperature. It should be realized, however, that one of these frames covers a total distance of 0.13 inches, so the transition is a sharp discontinuity on the macroscale.

Crack length versus propagation time for the high temperature tests is contained in Figures 41, 42, 44, and 45. Figure 42 shows the transition region between low velocity and high velocity fracture for runs 112-3, 112-4, and 112-5. In this case, time is represented as the interval between the time at a given crack length and the time of the last test point. The reason for presenting the

data in this manner is that the transition occurs in approximately one millisecond. The three curves shown in Figure 42 all indicate velocities in the high velocity region less than the terminal value measured in the high loading rate test. Even though the curves in the high velocity region appear to be straight and the velocity, therefore, constant, this portion of each curve is in the region of acceleration to terminal velocity. The curves appear straight merely because they are defined by only a few points and the uncertainty in the location of these points is relatively large. It is to be expected, however, that as the applied load at the time of transition from low velocity to high velocity propagation decreases, the acceleration will be slower. This phenomena is indicated in the figure because each curve shows a different maximum velocity. Crack length at the juncture between the steep rising portion of the curve and the low velocity region corresponds exactly with the sharp discontinuity line seen on the fracture surface of each specimen. Reference to the strain rate for the various tests also indicates that the crack propagation is slower and the distance to the transition point is longer as the loading rate decreases.

Figures 46, 47, 48, and 49 are crack velocity curves for the high temperature tests. A log-log scale is used in this case, because the velocity values range from 0.01 to 10,000 inches per second (six decades). The time could be plotted using a linear scale, but the transition region would be compressed into a narrow vertical band and the characteristics of this region could not be seen. The high velocity region can be seen only on three of the

tests, however, but for uniformity the log scale is used. For convenience, a tabulation of crack length and velocity data for all of these runs can be found in Tables I through IX.

6.2 COMPARISON WITH THEORY

As explained in the introduction, Schapery and Williams (14) developed a modification of the Berry theory which would apply to viscoelastic materials. This is an energy analysis which pertains to low velocity crack propagation. The basic assumption is that the kinetic energy can be neglected at low velocity and a dissipation term added. The dissipation term was obtained using modified dimensional analysis. The equations for crack length versus time and for crack velocity versus time are as follows:

$$\dot{c} - \frac{2\pi E}{\eta} c + \frac{4\gamma E^2}{\eta \sigma(t)^2} = 0 \qquad (6.2\text{-}1)$$

For the constant load case $\sigma(t) = \sigma_o$ and

$$\frac{c}{c_o} = \left[1 - \left(\frac{\sigma_g}{\sigma_o}\right)^2\right] \exp\left[\frac{2\pi E t}{\eta}\right] + \left(\frac{\sigma_g}{\sigma_o}\right)^2 \qquad (6.2\text{-}2)$$

$$\frac{\dot{c}}{c_o} = \frac{2\pi E}{\eta} \left[1 - \left(\frac{\sigma_g}{\sigma_o}\right)^2\right] \exp\left[\frac{2\pi E t}{\eta}\right]$$

For the case of a constant load rate during fracture $\sigma(t) = \sigma_f + Bt$ where σ_f is the gross sectional stress at the initiation of the crack run and B is the slope of the stress versus time curve during the crack run. In this case when $B/\sigma_f < 0.1$ sec^{-1}:

$$\frac{c}{c_o} = \left[1 - \left(\frac{\sigma_g}{\sigma_f}\right)^2 \left(1 - \frac{2B\eta}{\pi E\sigma_f}\right)\right] \exp\left[\frac{2\pi Et}{\eta}\right]$$

$$+ \left(\frac{\sigma_g}{\sigma_f}\right)^2 \left[1 - \frac{2B\eta}{\pi E\sigma_f}\left(1 + \frac{2\pi Et}{\eta}\right)\right] \qquad (6.2\text{-}3)$$

$$\frac{\dot{c}}{c_o} = \left(\frac{2\pi E}{\eta}\right)\left[1 - \left(\frac{\sigma_g}{\sigma_f}\right)^2 \left[1 - \frac{2B\eta}{\pi E\sigma_f}\right] \exp\left[\frac{2\pi Et}{\eta}\right]\right. \qquad (6.2\text{-}4)$$

where

c = crack length

c_o = initial crack length

$\dot{c}$ = crack velocity

E = rubbery modulus of the material

$\sigma_g = \frac{2\gamma E}{\pi c_o}$

η = constant associated with the viscous dissipation. All other notation has been changed to conform with that used in Section 5.0.

t is measured from the instant at which the crack starts to grow.

These equations contain two undetermined constants which are a function of the specific surface energy, the elastic modulus of the material, a viscosity coefficient and the applied stress.

Figures 50 and 51 show comparisons between the Schapery and Williams theory and experimental data for Runs 112-2 and 112-7. In both cases equation (6.2-3) was used because the stress is varying during crack propagation for both runs. Run 112-7 is an approximation to a constant force test but the loading actually decreased

slightly during crack propagation. This was accounted for by using a negative value for $\underline{B}$ in equation (6.2-3). As can be seen in the figures, the theoretical curves match the experimental data for at least 75 percent of the total time interval for crack propagation. The entire low speed portion can be approximated by extending the theoretical curve to the time value at which the transition to high velocity fracture occurs and drawing a vertical line at this point. For run 112-2 the transition occurred at a theoretical velocity value of $\dot{c}/c_o = 0.82$ sec^{-1} and for run 112-7 at $\dot{c}/c_o = 1.5$ sec^{-1}. If a value of $\dot{c}/c_o = 1.0$ is chosen for these runs, then the transition point would be predicted within 0.25 seconds in both cases. This is a reasonable approximation. A study of the data from the other runs will reveal that a value of $\dot{c}/c_o = 1.0$ will predict the transition within the same time interval of ± 0.25 seconds.

This method, of course, does not allow a prediction of acceleration characteristics during the velocity increase from approximately 100 inches per second to the limiting velocity. As a crude approximation the Berry theory could be used in the high velocity, but the value of the parameter $\underline{n}$ which is associated with specific surface energy would have to be determined on the basis of a considerable number of experiments.

Figures 52 and 53 show comparisons between experimental isochromatic patterns and theoretical patterns for the case of static loading on a plate with a stationary crack. The letter $\underline{n}$ in the figures refers to the fringe order of dark fringes, e.g., n = 4 is the fourth dark fringe counting from the zero order fringe. The zero order

fringe is dark because the polaroids were crossed at the zero load condition. The magnitudes of $\bar{\tau} = (\epsilon_1 - \epsilon_2)/\bar{\epsilon}_y$ which correspond to the values of $\underline{n}$ for the experimental curves shown in the figures are not included because the calculation of $\bar{\tau}$ involves quantities which are unknown. In order to compute $\bar{\tau}$, the shape of the strain versus time curve must be known for each point on the isochromatic line. As the crack extends this strain history becomes very complex particularly in the neighborhood of the crack where it is apparent from the photographs that large displacements are occurring. For the case shown in Figure 52 an approximation for $\bar{\tau}$ was computed based on the assumption that a constant strain rate was applied at every point in the field. With this assumption:

$$n(t) = \frac{1}{t}\left[\int_0^t C_{\epsilon_{rel}}(t)\, dt\right]\left[\epsilon_1(t) - \epsilon_2(t)\right]$$

Using the values of $C_{\epsilon_{rel}}(t)$ from Figure 15, $(\epsilon_1 - \epsilon_2)/\bar{\epsilon}_y = 1.2$ for $n = 4$. As can be seen in Figure 52, the experimental pattern is closer to 1.15. On the basis of this analysis $n = 5$ should correspond to $\tau = 1.5$. The $n = 5$ contour is slightly larger than the theoretical $\tau = 1.5$ contour. The shapes of the patterns are generally the same as the theoretical patterns but the quantitative comparison is poor.

As the crack grows longer the experimental patterns show a marked deviation from the theoretical curves. In Figure 53, the $n = 5$ isochromatic is smaller than the $\bar{\tau} = 1.5$ pattern and has rotated backwards by at least 20°. The portion of the $n = 4$ contour

closest to the specimen centerline has considerable distortion toward the crack line. This is probably due to large deformations near the crack line.

7.0 RESULTS OF TESTS ON METAL SPECIMENS

Loading curves and average strain curves for three tests on metal specimens are contained in Figures 54 and 55. (These tests are designated M-1, M-2, and M-3.) In each case a high loading rate was applied and the load was brought to a constant value at which it remained during crack propagation. Thus, these are all constant load tests. As can be seen, the maximum load variation between the tests was relatively small. With this small load variation, however, it was possible to produce crack propagation at widely varying velocities. In each case as in the plastic specimens there was a region of slow crack propagation and a region of fast crack propagation.

Sample crack propagation photographs are contained in Figure 56 for run number M-1. A side view of the fracture surfaces for two of the specimens is shown in Figure 57 and photomicrographs of an edge view of the fracture surfaces are shown in Figure 58. The side view photographs indicate a somewhat discontinuous nature of the fracture. The photomicrographs show that in the region of slow crack propagation necking of the material occurred in the region adjacent to the fracture surface. The thickness of the fracture surface in the necked region is approximately 20 percent of the original specimen thickness. In the region of fast crack propagation the fracture surface was indicative of brittle cleavage within the grains across the full width of the specimen. The fracture surfaces (cleavage surfaces) are stepped at the grain boundaries.

Figure 59 contains curves of crack length versus time for these tests, and Figure 60 velocity versus time. It can be seen that the basic nature of these curves is the same as for the Homalite material. The data can be represented with the Schapery and Williams theory, where the constant which is attributed to viscous dissipation would in this case be a constant which is related to plastic dissipation.

It is apparent from these tests that it is possible by varying loading rate in the high loading rate region and varying the maximum constant load that low crack velocities can be generated for different crack lengths in exactly the same way as occurred in the tests on Homalite. In the case of the silicon-iron material, a loading rate higher than the maximum rate possible with the existing loading equipment would be necessary in order to produce an essentially brittle fracture over the full specimen width from the point of initiation. In these tests the minimum crack length increment from the initiation point to the transition to high velocity propagation was approximately 0.5 inches.

The original purpose for testing the metal specimens was to determine if the testing technique used for the Homalite material could be successfully used to investigate the fracture properties of annealed metal materials with simple structure. It is abundantly evident that the testing technique and the equipment developed for the Homalite program are fully applicable to crack propagation tests on metals. The main reason for the success of this technique on metals is the fact that metals are rate sensitive. It is seen from

these tests on metals that the crack velocity characteristics can be changed over a wide range by small changes in failure load. Also, on most of these materials high loading rates must be achieved in order to produce crack propagation prior to general yielding of the specimen. This was noted in preliminary investigations reported in the camera report (9). Thus in order to accomplish crack propagation studies in annealed metal materials, high strain rates must be used. It is expected that as the strain range to failure in the metal material decreases (with cold working or heat treatment) the loading rates can be decreased. Also, as the specimen thickness increases to the point where the specimen approaches a plane strain condition, the fracture takes on a progressively more brittle character. Lower loading rates should be possible, therefore, as the specimen thickness increases.

Data on the dynamic stress patterns during crack propagation probably can be obtained on metal using a modification of the light source and optical system developed for this investigation in conjunction with polished specimens and a photo-elastic coating (photo stress or using a Moire grid technique). If a Moire grid with both horizontal and vertical lines were used, it may be possible to obtain information on the complete surface stress pattern (including separation of the two principal stresses) under dynamic conditions.

The use of a large sheet specimen is particularly advantageous for tests in metal because the crack velocities during the high velocity phase are approximately three times the values

obtained for the Homalite specimens. It is doubtful that the acceleration time period in annealed metal specimens would be shorter than in the case of Homalite because of plastic dissipation, thus a framing rate on the GALCIT Camera of 100,000 frames per second should be adequate. If it is not, the framing rates on this camera can be increased to well above 150,000 frames per second with slight modifications in the turbine drive systems and in the electronic controls. It is apparent from the investigations on Homalite 100 that two cameras are required in order to do successful crack propagation studies in either plastics or metal materials where high velocities are achieved. The lower speed camera (such as the Hycam Camera) is not only necessary in order to obtain the low speed data, but this type of camera is necessary as a probing camera for all work which is done with the higher speed camera system. All preliminary work would be done with the lower speed camera to establish necessary framing rates, the approximate magnitudes of maximum crack velocities and the crack length values at which transition occurs to high speed fracture. The high speed GALCIT type camera would be used for the high speed photographs in conjunction with an initiator system which would be installed along the crack path. This device should be a small light source mounted adjacent to the specimen with a small photocell on the opposite side. When the crack passes this tiny light source, the output from the photocell would be the initiator signal. This type of device (or something similar) which does not directly contact

the specimen appears to be the only type of initiation device which is suitable for materials which have large plastic strain values prior to failure.

8.0 CONCLUSIONS

The conclusions from this investigation can be summarized as follows:

1. The testing equipment and the specimens used in this investigation appear to be suitable for crack propagation studies on many different types of plastic metal materials.

2. A viscoelastic polymer is an excellent model material for making general studies of crack propagation phenomena. The large rate sensitivity of the material accentuates the rate phenomena to be found in metal. The homogeneous, isotropic structure results in the elimination of complications which are found in metals due to the many structure variables.

Comparison between the results for Homalite 100 and silicon-iron suggest direct analogues between polymers and metals.

3. A sufficiently high loading rate can be produced with a simple hydraulic loading system to produce near brittle fracture in polymers or metals. The loading rates available with the equipment described in this report should be large enough to produce high acceleration crack propagation in polymers which are rubbery at room temperature. The use of a rubbery polymer (i.e., lower rubbery temperature and lower glass transition temperature) would allow a more careful investigation of propagation in the rubbery condition. Consequently, a better comparison of properties in the entire range from the rubbery to the glassy region could be made on the same material.

4. The large specimen size chosen for this investigation in conjunction with the clamping and loading systems resulted in a close approximation to crack propagation in an infinite sheet for at least one half of the specimen width.

5. Even at the loading rates above 10^5 psi per second the isochromatic patterns prior to crack initiation are represented adequately by the theoretical patterns for static loading on a plate with a stationary crack. In the high loading rate tests after the crack had reached terminal velocity the isochromatic patterns near the crack tip are closely matched by the theoretical solution of Broberg for the stress field around a crack expanding at constant velocity. These results indicate that in the high loading rate tests a close approximation to an elastic (glassy) condition was achieved.

6. In the high loading rate tests, branching of the main crack occurred in all test runs. The crack length at the point of branching was affected by changes in the applied stress at the initiation of crack propagation. As the applied stress at failure increased, the crack length at the branching point decreased.

The influence on the branching process by waves reflecting off the side boundaries and returning to the crack tip probably was negligible. The reason for this conclusion is that the waves generated during the initiation process had reflected and passed by the crack tip at least 100 microseconds before branching occurred. The continuous train of waves generated during the remainder of the crack run up to branching was of constant intensity and, therefore, would not result in a branching at any particular time.

7. The theoretical solution by Berry (13) for crack acceleration characteristics in an elastic material does not appear to be an adequate representation of experimental data. It gives a crude approximation to the crack length versus time curve but there is a large difference between calculated and measured velocity values during acceleration.

8. With a proper choice of loading rates in a constant loading rate test, slow crack propagation can be produced in plastic or metal with the equipment described in this report. In the case of a constant force test, both the loading rate and the constant final load must be determined by experimenting with each material.

9. In all of the slow crack propagation tests in both plastic and metal, the crack velocity slowly increased until the velocity reached a value at which an instability condition occurred. At this point, the crack acceleration increased rapidly and within a few milliseconds the velocity increased by at least 1000 : 1 and reached a terminal velocity value. For Homalite, the terminal velocity was $0.19\sqrt{E/\rho}$.

10. On the fracture surface in the region where the instability occurs a sharp line can be seen. At high magnification it is evident that the fracture has changed from a ductile to a brittle type fracture in a short distance (of the order of 0.01 inches). The ductile fracture region is characterized by a system of V-shaped irregularities similar to those found in the ductile fracture of metal. In the high velocity region adjacent to the discontinuity, the surface is smooth over the full specimen thickness.

11. Low speed fracture can be characterized by a simple viscoelastic theory of fracture developed by Schapery and Williams. This theory closely matches the experimental data over at least 75 percent of the low velocity region. For crack length versus time, it is a good approximation over the entire region. A simple theory is proposed in which the curve generated by this theory is terminated with a vertical line (or ramp function) which represents a discontinuous rise to the limiting velocity.

12. For small crack lengths the isochromatic patterns during the slow velocity phase of propagation are approximately the same size and shape as the theoretical patterns for static loading of a plate with a stationary crack. The quantitative comparison of principal strain difference values based on the assumption of constant strain rate deformation during loading is reasonably close. For crack length divided by initial crack length (c/c_o) values greater than 2, the shapes of the experimental patterns deviate appreciably from the theoretical contours.

REFERENCES

1. Schardin, H: "Velocity Effects in Fracture," Fracture, Proceedings of an International Conference on Mechanisms of Fracture, Swampscott, Mass., Technology Press (1959), pp. 297-330.

2. Schardin, H.: "Fracture Processes in Glass," Proceedings of the International Commission on Glass, Vol. I (1954), pp. 81-95.

3. Shand, E. B.: "Fracture Velocity and Fracture Energy of Glass in the Fatigue Range," Journal of the American Ceramic Society, Vol. 44, No. 1 (January 1961), pp. 21-26.

4. Wells, A. A. and Post, D.: "The Stress Distribution Surrounding a Running Crack - A Photoelastic Analysis," U. S. Naval Research Laboratory (NRL) Report 4935 (April 23, 1957).

5. Williams, M. L., Jessey, M. E., and Parmerter, R. R.: "Some Exploratory Photoelastic Studies in Stress Wave Propagation," Society of Experimental Stress Analysis, Proceedings, Vol. XVII, No. 2, p. 121.

6. Hall, W. J. and Barton, F. W.: "Summary of Some Studies of Brittle-Fracture Propagation," U. S. Navy Bureau of Ships Report SSC-149 (September 1963).

7. Barton, F. W. and Hall, W. J.: "Brittle Fracture Tests of Six-Foot Wide Prestressed Steel Plates," The Welding Journal, Vol. 39, Research Supplement (September 1960), pp. 379-S to 384-S.

8. Hudson, G. and Greenfield, M.: "The Speed of Propagation of Brittle Cracks in Steel," Journal of Applied Physics, Vol. 18 (1947), pp. 405-407.

9. Beebe, W. M., Jessey, M. E., Liu, H. W., Valluri, S. R., and Williams, M. L.: "Development and Application of a High Speed Camera for Metallographic and Crack Propagation Studies," U. S. Air Force, Office of Aerospace Research, ARL 64-69 (April 1964).

10. Mott, N. F.: "Brittle Fracture in Mild Steel Plates," Engineering, Vol. 165 (January 2, 1948), pp. 16-18.

11. Roberts, D. K. and Wells, A. A.: "The Velocity of Brittle Fracture," Engineering, Vol. 178 (December 24, 1954), pp. 820-821.

12. Berry, J.P.: "Some Kinetic Considerations of the Griffith Criterion for Fracture - I. Equations of Motion for Constant Force. II. Equations of Motion at Constant Deformation," Journal of the Mechanics and Physics of Solids, Vol. 8 (1960), pp. 194-216.

13. Schapery, R.A. and Williams, M. L.: "On the Acceleration of Cracks in Viscoelastic Media," GALCIT SM 62-39, California Institute of Technology (September 1962).

14. Williams, M. L.: "Initiation and Growth of Viscoelastic Fracture," Proceedings of the International Conference on Fracture, Sendai, Japan (September 1965).

15. Griffith, A.A.: "The Phenomena of Rupture and Flow in Solids," Philosophical Transactions of the Royal Society, Vol. A 221 (1921), pp. 163-198. "The Theory of Rupture," Proceedings of the International Congress of Applied Mechanics, Delft (1924), pp. 55-63.

16. Westergaard, H. M.: "Bearing Pressures and Cracks" Journal of Applied Mechanics, Vol. 61 (1939), pp. A 49-53.

17. Inglis, C. E.: "Stresses in a Plate Due to the Presence of Cracks and Sharp Corners," Transactions of the Institute of Naval Architects, London, Vol. 60 (1913), pp. 219-230.

18. Neuber, H.: Theory of Notch Stresses, J. W. Edwards Co. (1946).

19. Sneddon, I. N.: Fourier Transforms, Mc-Graw Hill Book Co. (1950).

20. Williams, M. L.: "On the Stress Distribution at the Base of a Stationary Crack," Journal of Applied Mechanics, Vol. 24 (March 1957).

21. Ang, D. D. and Williams, M. L.: "Combined Stresses in an Orthotropic Plate Having a Finite Crack," ARL 22 (July 1961).

22. Paris, P. C. and Sih, G. C.: "Stress Analysis of Cracks," Fracture Toughness Testing and Its Applications, American Society for Testing and Materials (1964), pp. 30-82.

23. Swedlow, J. L.: "On the Elastostatic Stresses in Cracked Plates," GALCIT SM 62-9, California Institute of Technology (August 1962).

24. Dixon, J. R.: "Stress Distribution Around a Central Crack in a Plate Loaded in Tension; Effect of Finite Width of Plate," Journal of the Royal Aeronautical Society, Vol. 64 (1960), pp. 141-145.

25. Yoffe, E. H.: "The Moving Griffith Crack," Philosophical Magazine, Vol. 42, series 7 (1951), pp. 739-750.

26. Craggs, J. W.: "On the Propagation of a Crack in an Elastic-Brittle Material," Journal of the Mechanics and Physics of Solids, Vol. 8 (1960), pp. 66-75.

27. Broberg, K. B.: "The Propagation of a Brittle Crack," Arkiv für Fysik, Vol. 18, no. 10 (1960), pp. 159-192.

28. Baker, B. R.: "Dynamic Stresses Created by a Moving Crack," Journal of Applied Mechanics, Vol. 29 (September 1962), pp. 449-458.

29. Ang, D. D.: "The Dynamic Stress Field Due to an Extensional Dislocation," Proceedings of the Fourth Annual Conference on Solid Mechanics, University of Texas, Austin, Texas (September 1959), pp. 36-52.

30. Marsh, D. M.: "Flow and Fracture in Glass," Fracture of Solids - Proceedings of an International Conference, Maple Valley, Washington, August 21, 1962, Interscience Publishers (1963), pp. 143-155.

31. Arenz, R. J., Ferguson, C. W., Kunio, T., and Williams, M. L.: "The Mechanical and Optical Characterization of Hysol 8705 with Application to Photoviscoelastic Analysis," U. S. Air Force Technical Documentary Report No. WL TDR-64-4 (June 1964); also, Williams, M. L. and Arenz, R. J.: "The Engineering Analysis of Linear Photoviscoelastic Materials," Experimental Mechanics (September 1964).

32. Williams, M. L., Landel, R. F., and Ferry, J. D.: "The Temperature Dependence of Relaxation Mechanisms in Amorphous Polymers and Other Glass-Forming Liquids," Journal of the American Chemical Society, Vol. 77 (1955), pp. 3701-3707.

33. Theocaris, P. S. and Mylonas, D.: "Viscoelastic Effects in Birefringent Coatings," Journal of Applied Mechanics, Vol. 28 (1961), pp. 601-607; also, Discussion in Journal of Applied Mechanics, Vol. 29 (1962), pp. 598-603.

34. Clark, A. B. J. and Sanford, R. J.: "A Comparison of Static and Dynamic Properties of Photoviscoelastic Materials,"

Society of Experimental Stress Analysis - Proceedings, Vol. 20, no. 1 (1963), pp. 148-151.

35. Feltner, C. E.: "On the Mechanical Behavior and Fracture Morphology of Epoxy Resin," University of Illinois, T. and A. M. Report No. 224 (1962).

36. Kies, J. A., Sullivan, A. M., and Irwin, G. R.: "Interpretation of Fracture Markings," Journal of Applied Mechanics, Vol. 21 (1950), pp. 716-720.

37. Wolock, J., Newman, S. B.: "Fracture Topography," Fracture Processes in Polymeric Solids, Interscience Publishers (1964), pp. 235-289.

38. Andrews, E. H.: "Stress Waves and Fracture Surfaces," Journal of Applied Physics, Vol. 39 (1959), pp. 740-743.

APPENDIX

DIMENSIONAL ANALYSIS OF CRACK PROPAGATION KINETICS IN AN ELASTIC MATERIAL

The basic assumptions for this analysis are as follows:

1. The material is homogeneous, isotropic and linearly elastic.

2. A sheet or plate specimen is assumed in which stresses and displacements are a function only of coordinates in the plane of the sheet, i.e., a two-dimensional problem.

3. The sheet is infinite in size or has a large enough finite size such that the stress distribution is the same as for an infinite sheet.

4. The sheet has a centrally located crack of finite length, 2c, and an infinitesimal crack opening. The surfaces of the crack are stress free.

5. A uniaxial surface traction is applied at the specimen boundary in a direction perpendicular to the length direction of the crack. The load is applied as a linear function of time until fracture occurs and the initial crack starts to run, then the load is held constant.

6. Displacements in the plate are a function of x, y, c_o, c, E, ν, γ, ρ, and σ

where

x, y = coordinates in the plane of the plate. This is a fixed coordinate system

c = one half crack length (inches)

c_o = initial half crack length (inches)

E = elastic modulus (psi)

ν = Poisson's ratio (dimensionless)

γ = specific surface energy

σ = surface traction at the boundary (psi)

7. During loading and during the crack run

$$W + S_1 = U + S + K \qquad (A-1)$$

where

W = work done on the plate by the surface tractions

U = internal strain energy in the plate

S = total surface energy of the plate

S_1 = surface energy during loading of the plate

K = kinetic energy in the plate

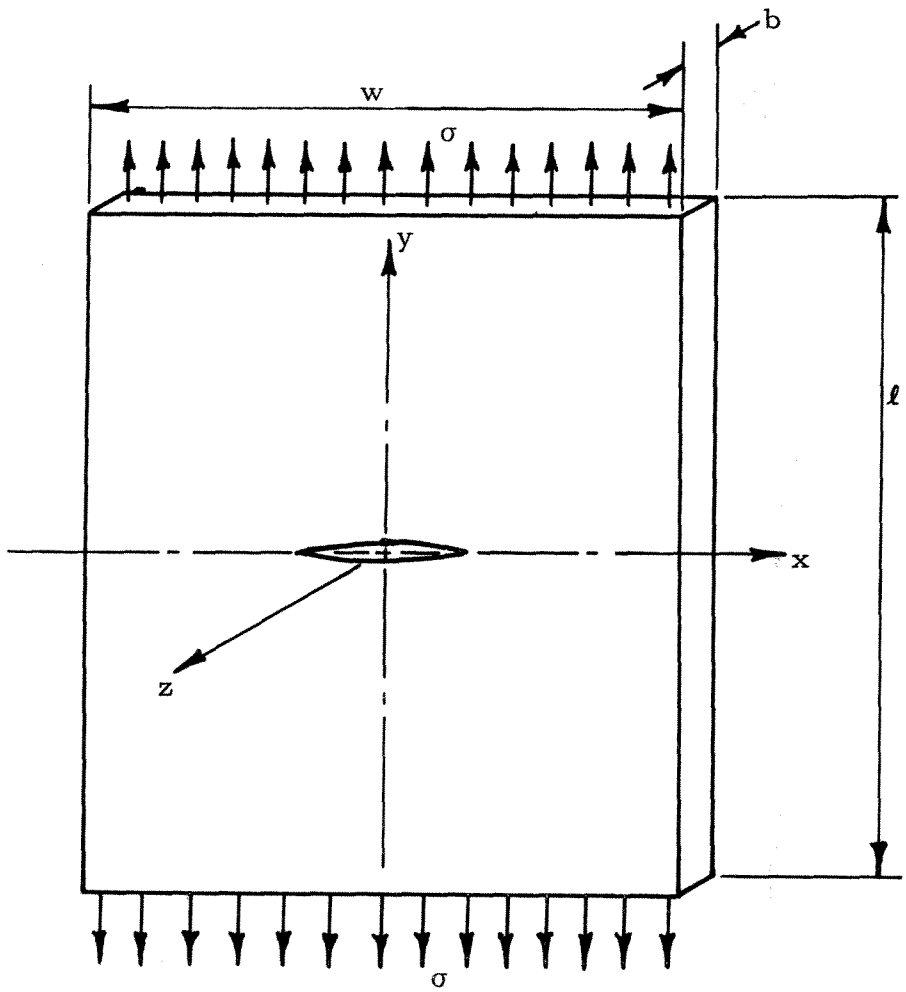

$$W = W_1 + 2b\sigma \int_{-\frac{w}{2}}^{\frac{w}{2}} dx \int^{v_\sigma(x)} dv_\sigma \qquad \text{(A-2)}$$

where

W_1 = work done during loading up to the fracture point. This quantity is equal to the strain energy, U_1, in the plate at the time of the initiation of the crack run.

$W_1 = U_1$

v_σ = displacement at the upper and lower boundaries due to the action of the constant stress and the increase in flexibility of the plate as the crack length increases.

In the following discussion square brackets around a quantity represent the dimensions of the quantity. Force [F], length [L], and time [T], are assumed to be the basic dimensions.

$$[\rho] = [FL^{-4}T^2]$$

ρ is the only quantity among the variables above which contains time as a dimension; therefore it must be eliminated from the list. Crack length is a function of time but does not contain time as a dimension. The material properties are not functions of time because elastic material was assumed. Consequently:

$$v_\sigma = f_1 (x, y, c_o, c(t), E, \nu, \gamma, \sigma) \qquad \text{(A-3)}$$

Dimensionless quantities are now formed in which $\underline{c}$ is chosen to eliminate the dimension [L] and E to eliminate [F]

$$\frac{v_\sigma}{c} = f_2 \left(\frac{x}{c}, \frac{y}{c}, \frac{c_o}{c}, \frac{\sigma}{E}, \nu, \frac{\gamma}{Ec}\right) \qquad \text{(A-4)}$$

It is interesting to recall (12) that

$$\frac{\gamma}{Ec} = \frac{\pi}{2} \left(\frac{\sigma_g}{E}\right)^2 \left(\frac{c_o}{c}\right) \qquad \text{(A-5)}$$

where

$$\sigma_g^2 = \frac{2\gamma E}{\pi c_o} = \text{Griffith fracture stress}$$

In all known static and dynamic solutions for the displacements in a plate with a stationary or a running crack, the displacement is a linear function of the ratio σ/E. Thus, it is assumed that this term can be factored from equation A-4. With this assumption

$$\frac{v_\sigma}{c} = \frac{\sigma}{E} f_3 \left(\frac{x}{c}, \frac{y}{c}, \frac{c_o}{c}, \nu, \frac{\gamma}{Ec}\right) \tag{A-6}$$

and

$$W = U_1 + \frac{2bc^2\sigma^2}{E} \int_{-\frac{w}{2c}}^{\frac{w}{2c}} d\left(\frac{x}{c}\right) \int_0^{\frac{v_\sigma(x)}{c}} d\left(\frac{v_\sigma(x)}{c}\right) \tag{A-7}$$

$$W = U_1 + \frac{bc^2\sigma^2}{E} f_4 \left(\frac{c_o}{c}, \nu, \frac{\gamma}{Ec}\right) \tag{A-8}$$

Assuming that W is continuous and has continuous derivatives of all orders the function f_4 can be expanded in power series:

$$W = U_1 + \frac{bc^2\sigma^2}{E} \left[a_o + a_1 \left(\frac{c_o}{c}\right) + a_2 \left(\frac{c_o}{c}\right)^2 + \ldots\right] \tag{A-9}$$

$$W = U_1 + \frac{bc^2\sigma^2}{E} \left[b_o + b_1 \left(1 - \frac{c_o}{c}\right) + b_2 \left(1 - \frac{c_o}{c}\right)^2 + \ldots\right] \tag{A-10}$$

but when $c = c_o$, $W = U_1$ so $b_o = 0$, therefore:

$$W = U_1 + \frac{bc^2\sigma^2}{E} \left(1 - \frac{c_o}{c}\right) \left[b_1 + b_2 \left(1 - \frac{c_o}{c}\right) + b_3 \left(1 - \frac{c_o}{c}\right)^2 + \ldots\right] \tag{A-11}$$

In a similar manner

$$U = b \int_A dA \int^{\epsilon_{ij}} \sigma_{ij}\, d\epsilon_{ij} \tag{A-12}$$

where

σ_{ij} = general stress component

ϵ_{ij} = general strain component

but

$$\sigma_{ij} = \frac{E}{(1+\nu)}\left[\epsilon_{ij} + \frac{\nu\,\delta_{ij}\epsilon_{kk}}{(1-2\nu)}\right] \tag{A-13}$$

where

δ_{ij} = Kronecker delta

and

$$\epsilon_{ij} = \frac{1}{2}\left(\frac{\partial u_i}{\partial x_j} + \frac{\partial u_j}{\partial x_i}\right) \tag{A-14}$$

where

u_i = general displacement component ($u_1 = u$; $u_2 = v$; $u_3 = w$) where u, v and w are the displacements in the x, y, and z directions respectively.

Following the same dimensional procedure as previously:

$$\frac{\partial u_i}{\partial x_j} = \frac{\sigma}{E}\, g_\ell\left(\frac{x}{c}, \frac{y}{c}, \frac{c_o}{c}, \frac{\gamma}{Ec}, \nu\right) \tag{A-15}$$

Combining (A-12) through (A-15)

$$U = \frac{bc^2\sigma^2}{E}\int_A g_1\left(\frac{x}{c}, \frac{y}{c}, \frac{c_o}{c}, \frac{\gamma}{Ec}, \nu\right)\, d\left(\frac{x}{c}\right)\, d\left(\frac{y}{c}\right) \tag{A-16}$$

$$U = \frac{bc^2\sigma^2}{2E}\, g_2\left(\frac{c_o}{c}, \frac{\gamma}{Ec}, \nu\right) \tag{A-17}$$

$$U = \frac{bc^2\sigma^2}{2E} \left[d_o + d_1 \left(1 - \frac{c_o}{c}\right) + d_2 \left(1 - \frac{c_o}{c}\right)^2 + \ldots \right] \tag{A-18}$$

when

$$c = c_o,\ U = U_1 = \frac{\sigma^2 b}{2E} \left(A + 2\pi c_o^2\right) \tag{A-19}$$

according to Berry (12).

Thus:

$$d_o = \frac{A}{c_o^2} + 2\pi \tag{A-20}$$

and

$$U = U_1 + \frac{bc^2\sigma^2}{2E} \left[d_o \left[1 - \left(\frac{c_o}{c}\right)^2 \right] + d_1 \left(1 - \frac{c_o}{c}\right) + d_2 \left(1 - \frac{c_o}{c}\right)^2 + \ldots \right] \tag{A-21}$$

$$U = U_1 + \frac{bc^2\sigma^2}{2E} \left(1 - \frac{c_o}{c} \left[d_o \left(1 + \frac{c_o}{c}\right) + d_1 + d_2 \left(1 - \frac{c_o}{c}\right) + d_3 \left(1 - \frac{c_o}{c}\right)^2 + \ldots \right] \right) \tag{A-22}$$

In a similar manner

$$K = \frac{1}{2} \rho b \int_A \left(\frac{d\bar{u}(x,y)}{dt} \right)^2 dA \tag{A-23}$$

where

$$\bar{u}(x,y) = \bar{i}\, u(x,y) + \bar{j} v(x,y) \tag{A-24}$$

$$\frac{du}{dt} = \frac{\partial u}{\partial c} \frac{dc}{dt} = \dot{c} \frac{\partial u}{\partial c} \tag{A-25}$$

because $\underline{c}$ is the only function of time among the basic variables

$$\frac{\partial u}{\partial c} = \frac{\sigma}{E} h_1 \left(\frac{x}{c}, \frac{y}{c}, \frac{c_o}{c}, \frac{\gamma}{Ec}, \nu \right) \tag{A-26}$$

$$K = \frac{\frac{1}{2} \rho b c^2 \dot{c}^2 \sigma^2}{E^2} \int_A h_2 \left(\frac{x}{c}, \frac{y}{c}, \frac{c_o}{c}, \frac{\gamma}{Ec}, \nu \right) d\left(\frac{x}{c}\right) d\left(\frac{y}{c}\right) \tag{A-27}$$

$$K = \frac{\frac{1}{2} \rho b c^2 \dot{c}^2 \sigma^2}{E^2} h_3 \left(\frac{c_o}{c}, \frac{\gamma}{Ec}, \nu \right) \tag{A-28}$$

$$K = \frac{\frac{1}{2} \rho b c^2 \dot{c}^2 \sigma^2}{E^2} \left[m_0 + m_1 \left(\frac{c_o}{c}\right) + m_2 \left(\frac{c_o}{c}\right)^2 + \ldots \right] \tag{A-29}$$

The surface energy term is as follows:

$$S = S_o + 4b\gamma c \tag{A-30}$$

where S_o = surface energy of a plate which does not contain the central crack

Combining equations (A-1). A-11), A-22), (A-29) and (A-30)

$$S_o + 4b\gamma c_o + W = S_o + 4b\gamma c + U + K \tag{A-31}$$

$$U_1 + \frac{b c^2 \sigma^2}{E} \left(1 - \frac{c_o}{c}\right) \left[b_1 + b_2 \left(1 - \frac{c_o}{c}\right) + b_3 \left(1 - \frac{c_o}{c}\right)^2 + \ldots \right]$$

$$= 4b\gamma(c - c_o) + U_1 + \frac{b c^2 \sigma^2}{2E} \left(1 - \frac{c_o}{c}\right) \left[d_o \left(1 + \frac{c_o}{c}\right) + d_1 \right.$$

$$\left. + d_2 \left(1 - \frac{c_o}{c}\right) + d_3 \left(1 - \frac{c_o}{c}\right)^2 + \ldots \right] +$$

$$\frac{\frac{1}{2} \rho b c^2 \dot{c}^2 \sigma^2}{E^2} \left[m_0 + m_1 \left(\frac{c_o}{c}\right) + m_2 \left(\frac{c_o}{c}\right)^2 + \ldots \right] \tag{A-32}$$

$$\dot{c}^2 = 2\left(\frac{E}{\rho}\right)\left(1 - \frac{c_o}{c}\right)\left\{\left[b_1 + b_2\left(1 - \frac{c_o}{c}\right) + \ldots\right] - \frac{1}{2}\left[d_o\left(1 + \frac{c_o}{c}\right) + d_1 + d_2\left(1 - \frac{c_o}{c}\right) + \ldots\right] - \frac{4\gamma E}{\sigma^2 c_o}\left(\frac{c_o}{c}\right)\right\}$$

$$\frac{}{\left[m_0 + m_1\left(\frac{c_o}{c}\right) + m_2\left(\frac{c_o}{c}\right)^2 + \ldots\right]} \qquad \text{(A-33)}$$

Assuming $m_0 \neq 0$ and $\sum_{n=0}^{\infty} m_n \neq 0$ when $c_o/c = 1$ a new series can be formed.

Using the same general form as proposed by Berry (12)

$$\dot{c}^2 = \left(\frac{2\pi}{k}\right)\left(\frac{E}{\rho}\right)\left(1 - \frac{c_o}{c}\right)\left\{r_o + (r_1 - n)\left(\frac{c_o}{c}\right) + r_2\left(\frac{c_o}{c}\right)^2 + \ldots\right\} \qquad \text{(A-34)}$$

where:

$n = \dfrac{4\gamma E}{c_o \sigma^2} = 2\left(\dfrac{\sigma_g}{\sigma^2}\right)$; n is separated for convenience but it should be realized that all r_n may be functions of $\underline{n}$.

In the Berry solution:

$r_o = 1$, $r_1 = 1$ and $r_n = 0$ for $n > 1$

$\left(\dfrac{2\pi}{k}\right)\left(\dfrac{E}{\rho}\right) = v_m^2$ = terminal or limiting velocity, which is not a function of σ.

$$\ddot{c} = \left(\frac{E}{\rho}\right)\left(\frac{c_o}{c^2}\right)\left\{(n + r_o - r_1) + 2(r_1 - r_2 - n)\left(\frac{c_o}{c}\right) + 3(r_2 - r_3)\left(\frac{c_o}{c}\right)^2 + \ldots\right\} \qquad \text{(A-35)}$$

These equations are general representations of the complete dynamic problem.

TABLE I

Crack Propagation Data for
Test No. 112-1

Experimental Data		Data from Faired Curve*		
t (seconds)	c (inches)	t (seconds)	c (inches)	v (inches/sec)
0	0.350	0.100	0.362	0.109
0.1974	0.375	0.200	0.373	0.117
0.2763	0.395	0.300	0.386	0.129
0.4010	0.400	0.400	0.400	0.146
0.5050	0.415	0.500	0.415	0.163
0.5705	0.425	0.600	0.432	0.185
0.7030	0.452	0.700	0.452	0.210
0.7599	0.465	0.750	0.462	0.222
0.8419	0.485	0.800	0.474	0.248
0.8898	0.500	0.850	0.487	0.240
0.9123	0.515	0.870	0.493	0.325
0.9341	0.535	0.890	0.501	0.486
0.94480	0.550	0.910	0.512	0.709
0.95538	0.565	0.920	0.520	0.849
0.96054	0.585	0.930	0.530	1.075
0.96521	0.060	0.940	0.541	1.424
0.96583	>3.00	0.945	0.550	1.659
		0.950	0.559	1.970
		0.955	0.570	2.337
		0.960	0.583	2.837
		0.9652	0.600	3.566

* A plot of c versus t was made using the experimental data. A curve was then faired through these points. Velocity values, v , were determined from the slopes of the c versus t curve. During the last portion of the crack run, time values are presented to five places behind the decimal so that time spacing can be calculated during transition to high speed fracture.

TABLE II

Crack Propagation Data for
Test No. 112-2

Experimental Data		Data from Faired Curve		
t (seconds)	c (inches)	t (seconds)	c (inches)	v (inches/sec)
0	0.300	0	0.300	0
0.5384	0.330	0.200	0.310	0.050
0.7894	0.350	0.400	0.320	0.055
0.9738	0.350	0.600	0.332	0.067
1.1339	0.375	0.800	0.346	0.077
1.2806	0.400	1.000	0.363	0.096
1.4184	0.425	1.200	0.386	0.127
1.5500	0.450	1.400	0.415	0.175
1.6158	0.460	1.500	0.434	0.210
1.6770	0.475	1.600	0.456	0.243
1.7393	0.490	1.650	0.468	0.286
1.8008	0.525	1.700	0.483	0.304
1.86176	0.560	1.750	0.499	0.346
1.87401	0.560	1.800	0.518	0.431
1.88609	0.575	1.820	0.526	0.494
1.89826	0.600	1.840	0.537	0.575
		1.860	0.550	0.670
		1.870	0.557	0.744
		1.880	0.560	1.010
		1.890	0.577	1.706
		1.8983	0.600	3.313

TABLE III

Crack Propagation Data for
Test No. 112-3

Experimental Data		Data from Faired Curve		
t (seconds)	c (inches)	t (seconds)	c (inches)	v (inches/sec)
0	0.425	0	0.425	0.085
0.2900	0.460	0.200	0.446	0.108
0.3920	0.475	0.400	0.471	0.148
0.4810	0.480	0.600	0.506	0.220
0.6360	0.510	0.700	0.530	0.257
0.7710	0.575	0.800	0.558	0.292
0.8920	0.590	0.900	0.589	0.338
1.0050	0.640	1.000	0.625	0.430
1.0590	0.665	1.050	0.650	0.577
1.1110	0.690	1.100	0.683	0.711
1.1620	0.740	1.150	0.725	0.946
1.2120	0.790	1.200	0.779	1.228
1.2360	0.825	1.220	0.802	1.402
1.2600	0.860	1.240	0.832	1.497
1.2840	0.915	1.260	0.863	1.657
1.2980	0.950	1.280	0.898	2.003
1.3080	0.975	1.290	0.920	2.358
1.3120	0.990	1.300	0.947	2.994
1.3177	1.025	1.305	0.962	3.677
1.3201	1.030	1.310	0.983	4.450
1.3224	1.065	1.315	1.008	5.601
1.3243	1.065	1.320	1.040	7.507
1.32525	1.075	1.32582	1.100	18.661
1.32563	1.075	1.32601	2.375	6658.
1.32582	1.110	1.32620	3.575	6316.
1.32601	2.375			
1.32620	3.575			

TABLE IV

Crack Propagation Data for
Test No. 112-4

Experimental Data		Data from Faired Curve		
t (seconds)	c (inches)	t (seconds)	c (inches)	v (inches/sec)
0	0.30	0	0.30	-
0.3570	0.305	0.200	0.301	0.012
0.5940	0.310	0.400	0.305	0.032
0.7870	0.325	0.600	0.312	0.052
0.9590	0.350	0.800	0.327	0.076
1.0650	0.360	1.000	0.348	0.139
1.1660	0.375	1.100	0.364	0.211
1.2620	0.425	1.200	0.391	0.309
1.3560	0.475	1.300	0.430	0.458
1.4470	0.503	1.350	0.456	0.532
1.4900	0.560	1.400	0.484	0.662
1.5350	0.615	1.450	0.522	0.827
1.5570	0.640	1.500	0.568	1.045
1.5790	0.640	1.520	0.592	1.124
1.5880	0.685	1.540	0.616	1.238
1.5924	0.710	1.560	0.643	1.440
1.5946	0.725	1.570	0.658	1.605
1.5963	0.730	1.580	0.675	1.965
1.5970	0.750	1.585	0.686	2.560
1.59735	0.775	1.590	0.702	3.775
1.59746	2.000	1.5946	0.725	6.818
1.59757	3.125	1.5970	0.750	10.331
1.59768	4.250	1.59735	0.775	5,100.
		1.59746	2.000	10,500.
		1.59757	3.125	11,100.
		1.59768	4.250	12,000.

TABLE V

Crack Propagation Data for
Test No. 112-5

Experimental Data		Data from Faired Curve		
t (seconds)	c (inches)	t (seconds)	c (inches)	v (inches/sec)
0	0.470	0	0.470	-
0.000103	0.475	0.000103	0.475	-
0.000206	0.475	0.000206	0.480	-
0.000309	0.600	0.000309	0.600	3670
0.000412	1.075	0.000412	1.070	5800
0.000515	1.575	0.000515	1.575	6200
0.000618	2.125	0.000618	2.100	6360
0.000721	2.625	0.000721	2.635	6700

TABLE VI

Crack Propagation Data for
Test No. 112-6

Experimental Data		Data from Faired Curve		
t (seconds)	c (inches)	t (seconds)	c (inches)	v (inches/sec)
0	0.300	0	0.300	-
0.2160	0.310	0.200	0.313	0.048
0.6340	0.325	0.400	0.324	0.062
1.0120	0.360	0.600	0.336	0.060
1.3900	0.390	0.800	0.348	0.061
1.7360	0.425	1.000	0.361	0.067
1.9800	0.440	1.200	0.376	0.083
2.2320	0.490	1.400	0.393	0.086
2.4830	0.540	1.600	0.411	0.090
2.9798	0.600	1.800	0.430	0.100
3.1040	0.675	2.000	0.450	0.110
3.3524	0.675	2.200	0.472	0.129
3.6008	0.725	2.400	0.500	0.147
3.7250	0.815	2.600	0.534	0.165
3.8492	0.865	2.800	0.569	0.185
3.9734	0.925	3.000	0.609	0.215
4.0976	0.975	3.200	0.655	0.252
4.2218	1.075	3.400	0.710	0.292
4.2839	1.100	3.600	0.775	0.348
4.3460	1.135	3.800	0.852	0.412
4.4081	1.215	4.000	0.940	0.487
4.4702	1.275	4.200	1.050	0.636
4.5323	1.375	4.400	1.214	0.973
4.5944	1.475			
4.6068	1.500	4.500	1.325	1.435
4.6316	1.550	4.550	1.402	1.599

TABLE VI (Cont'd.)

Experimental Data		Data from Faired Curve		
t (seconds)	c (inches)	t (seconds)	c (inches)	v (inches/sec)
4.6440	1.575	4.600	1.487	1.929
4.6564	1.625	4.650	1.611	3.169
4.6688	1.675	4.700	1.792	3.973
4.6812	1.725	4.710	1.835	4.259
4.6936	1.775	4.720	1.881	5.150
4.7060	1.825	4.730	1.937	6.350
4.7184	1.870	4.740	2.008	7.883
4.7246	1.810	4.750	2.099	10.477
4.7308	1.940	4.7535	2.160	37.154
4.7348	1.975			
4.7388	2.000			
4.7428	2.035			
4.7468	2.060			
4.7484	2.075			
4.7500	2.100			
4.7516	2.125			
4.7526	2.125			
4.7535	2.160			

TABLE VII

Crack Propagation Data for
Test No. 112-7

Experimental Data		Data from Faired Curve		
t (seconds)	c (inches)	t (seconds)	c (inches)	v (inches/sec)
0	0.300	0	0.300	-
0.715	0.325	0.500	0.318	0.035
1.430	0.350	1.000	0.336	0.037
2.145	0.375	1.500	0.356	0.044
2.860	0.470	2.000	0.379	0.051
3.575	0.500	2.500	0.410	0.072
3.933	0.540	3.000	0.449	0.085
4.291	0.585	3.500	0.495	0.095
4.649	0.635	3.750	0.520	0.105
5.007	0.710	4.000	0.548	0.117
5.221	0.730	4.250	0.578	0.131
5.435	0.800	4.500	0.612	0.148
5.578	0.825	4.750	0.652	0.168
5.649	0.860	5.000	0.698	0.199
5.721	0.875	5.250	0.752	0.232
5.792	0.910	5.500	0.817	0.292
5.864	0.975	5.625	0.855	0.338
5.936	1.000	5.750	0.902	0.386
6.007	1.030	5.875	0.953	0.468
6.078	1.075	6.000	1.020	0.614
6.150	1.120	6.100	1.105	0.710
6.222	1.185	6.150	1.122	0.861
6.294	1.275	6.200	1.165	0.885
6.366	1.375	6.250	1.211	0.943
6.402	1.390	6.300	1.261	1.057
6.420	1.415	6.350	1.317	1.237

TABLE VII (Cont'd.)

Experimental Data		Data from Faired Curve		
t (seconds)	c (inches)	t (seconds)	c (inches)	v (inches/sec)
6.437	1.450	6.400	1.387	1.577
6.455	1.515	6.420	1.422	1.878
6.464	1.535	6.440	1.462	2.264
6.473	1.565	6.460	1.513	2.809
6.482	1.590	6.480	1.578	3.765
6.491	1.640	6.490	1.619	4.637
6.499	1.665	6.500	1.675	6.777
6.503	1.690	6.509	1.750	16.087
6.507	1.750			

TABLE VIII

Crack Propagation Data for

Test No. 120-1

Experimental Data		Data from Faired Curve		
t (seconds)	c (inches)	t (seconds)	c (inches)	v (inches/sec)
0	0.300	0	0.300	-
0.725	0.325	0.500	0.320	0.036
1.449	0.375	1.000	0.340	0.047
2.172	0.425	1.500	0.370	0.058
2.900	0.500	2.000	0.400	0.084
3.262	0.575	2.500	0.450	0.117
3.407	0.610	3.000	0.520	0.178
3.552	0.650	3.200	0.560	0.207
3.697	0.700	3.400	0.605	0.242
3.842	0.750	3.600	0.665	0.306
3.914	0.775	3.800	0.732	0.398
3.986	0.825	4.000	0.825	0.545
4.058	0.840	4.100	0.840	0.664
4.130	0.900	4.200	0.960	0.804
4.202	0.975	4.300	1.050	0.997
4.274	1.030	4.400	1.160	1.197
4.346	1.125	4.500	1.300	1.498
4.418	1.190	4.600	1.475	2.074
4.490	1.290	4.630	1.513	2.726
4.562	1.390	4.660	1.602	3.249
4.598	1.425	4.690	1.710	4.057
4.634	1.535	4.720	1.843	4.645
4.652	1.575	4.740	1.940	5.059
4.670	1.635	4.760	2.046	5.638
4.688	1.700	4.780	2.175	7.002
4.706	1.800	4.790	2.250	8.292

TABLE VIII (Cont'd.)

Experimental Data		Data from Faired Curve		
t (seconds)	c (inches)	t (seconds)	c (inches)	v (inches/sec)
4.724	1.860	4.800	2.342	9.770
4.733	1.925	4.810	2.448	11.504
4.742	1.950	4.815	2.510	12.815
4.751	2.000	4.820	2.578	15.301
4.760	2.050	4.825	2.666	21.123
4.769	2.100	4.830	2.810	41.126
4.778	2.165			
4.787	2.225			
4.796	2.310			
4.805	2.400			
4.814	2.500			
4.819	2.575			
4.821	2.590			
4.823	2.610			
4.825	2.650			
4.826	2.680			
4.828	2.760			
4.830	2.810			

TABLE IX

Crack Propagation Data for
Test No. 120-2

Experimental Data		Data from Faired Curve		
t (seconds)	c (inches)	t (seconds)	c (inches)	v (inches/sec)
0	0.360	0	0.350	-
0.288	0.365	0.250	0.362	0.039
0.432	0.375	1.000	0.396	0.045
0.576	0.390	2.000	0.444	0.053
1.152	0.400	3.000	0.505	0.067
1.296	0.415	4.000	0.581	0.090
1.872	0.430	4.500	0.630	0.100
2.160	0.440	5.000	0.685	0.115
2.448	0.475	5.500	0.747	0.134
2.592	0.490	6.000	0.825	0.167
3.024	0.500	6.250	0.860	0.184
3.456	0.535	6.500	0.917	0.198
3.744	0.575	6.750	0.970	0.221
4.032	0.600	7.000	1.029	0.246
4.320	0.625	7.250	1.095	0.285
4.608	0.640	7.500	1.175	0.340
4.896	0.675	7.632	1.225	0.368
5.184	0.725			
5.328	0.750			
5.616	0.765			
5.760	0.775			
5.904	0.800			
6.048	0.825			
6.192	0.860			
6.336	0.895			
6.480	0.930			

TABLE IX (Cont'd.)

Experimental Data		Data from Faired Curve		
t (seconds)	c (inches)	t (seconds)	c (inches)	v (inches/sec)
6.624	0.950			
6.768	0.980			
6.912	1.010			
7.056	1.050			
7.200	1.075			
7.344	1.125			
7.488	1.150			
7.632	1.225			

TABLE X

Crack Propagation Data for
Test M-1 (Silicon-Iron)

Experimental Data		Data from Faired Curve		
t (seconds)	c (inches)	t (seconds)	c (inches)	v (inches/sec)
0	0.350	0	0.350	-
0.0078	0.375	0.0050	0.365	1.862
0.0093	0.400	0.0100	0.378	2.328
0.0117	0.425	0.0150	0.390	2.840
0.0233	0.425	0.0200	0.405	3.726
0.0288	0.475	0.0250	0.430	5.360
0.0349	0.500	0.0300	0.460	7.586
0.0370	0.500	0.0350	0.505	10.769
0.0400	0.575	0.0400	0.570	15.550
0.0431	0.625	0.045	0.660	22.562
0.0463	0.700	0.0475	0.720	27.286
0.0478	0.750	0.0500	0.800	34.646
0.0509	0.820	0.0525	0.910	50.802
0.0524	0.900	0.0550	1.050	65.362
0.0539	0.975	0.0563	1.140	73.521
0.0554	1.150	0.0575	1.240	81.176
0.0570	1.225	0.0588	1.345	89.632
0.0577	1.275	0.0600	1.465	100.872
0.0583	1.375	0.0613	1.605	118.232
0.05949	1.375	0.0625	1.770	158.144
0.06010	1.425	0.0635	2.000	318.888
0.06071	1.450			
0.06132	1.550			
0.06162	1.675			
0.06193	1.725			
0.06224	1.775			

TABLE X (cont'd.)

Experimental Data		Data from Faired Curve		
t	c	t	c	v
(seconds)	(inches)	(seconds)	(inches)	(inches/sec)
0.06256	1.825			
0.06288	1.825			
0.06320	1.900			
0.06351	2.000			
0.06382	2.025			
0.06414	2.040			

TABLE XI

Crack Propagation Data for
Test No. M-2

Experimental Data		Data from Faired Curve		
t (seconds)	c (inches)	t (seconds)	c (inches)	v (inches/sec)
0	0.350	0	0.350	-
0.113	0.375	0.050	0.352	0.036
0.159	0.375	0.100	0.355	0.146
0.182	0.390	0.150	0.365	0.163
0.228	0.410	0.200	0.370	0.163
0.347	0.410	0.250	0.380	0.255
0.407	0.425	0.300	0.395	0.346
0.432	0.460	0.350	0.412	0.346
0.457	0.460	0.400	0.425	0.346
0.469	0.515	0.430	0.438	0.655
0.482	0.550	0.450	0.460	1.535
0.494	0.600	0.480	0.520	2.638
0.507	0.600	0.500	0.570	3.921
0.519	0.635	0.520	0.688	6.232
0.522	0.700	0.530	0.752	7.786
0.535	0.825	0.540	0.845	8.950
0.541	0.890	0.550	0.955	10.24
0.547	0.925	0.555	1.050	23.07
0.55025	0.950	0.556	1.075	25.77
0.55188	0.975	0.558	1.200	61.34
0.55350	1.050			
0.55447	1.050	0.561	1.455	132.
0.55513	1.050	0.562	1.595	141.
0.55610	1.075	0.563	1.745	160.
0.55675	1.100	0.564	1.920	193.
0.55772	1.200	0.5644	1.995	212.

TABLE XI (Cont'd.)

Experimental Data		Data from Faired Curve		
t (seconds)	c (inches)	t (seconds)	c (inches)	v (inches/sec)
0.55838	1.200	0.5648	2.070	231.
0.55903	1.325	0.5652	2.180	259.
0.56021	1.400	0.5656	2.295	295.
0.56053	1.400	0.5660	2.420	339.
0.56085	1.550	0.5664	2.570	403.
0.56149	1.550	0.5668	2.755	498.
0.56213	1.610	0.5672	2.975	615.
0.56278	1.625	0.5676	3.255	804.
0.56342	1.665	0.5679	3.510	1023.
0.56374	1.675			
0.56406	1.700			
0.56438	1.700			
0.56470	1.700			
0.56502	2.300			
0.56534	2.600			
0.56567	2.600			
0.56599	2.650			
0.56631	2.650			
0.56663	2.800			
0.56695	2.850			
0.56727	3.150			
0.56759	3.275			
0.56791	3.500			
0.56823	3.550			
0.56856	3.575			
0.56888	3.625			

TABLE XII

Crack Propagation Data for
Test No. M-3

Experimental Data		Data from Faired Curve		
t (seconds)	c (inches)	t (seconds)	c (inches)	v (inches/sec)
0	0.350	0	0.350	-
0.055	0.355	0.200	0.364	0.069
0.112	0.365	0.400	0.380	0.087
0.168	0.375	0.600	0.403	0.123
0.226	0.375	0.800	0.430	0.167
0.285	0.375	1.000	0.470	0.238
0.466	0.375	1.200	0.528	0.346
0.529	0.385	1.300	0.565	0.419
0.592	0.385	1.400	0.612	0.528
0.632	0.385	1.500	0.672	0.660
0.671	0.450	1.600	0.746	0.803
0.737	0.450	1.700	0.834	0.941
0.861	0.450	1.800	0.937	1.088
1.143	0.475	1.850	0.992	1.157
1.224	0.550	1.900	1.053	1.213
1.276	0.570	1.950	1.117	1.269
1.354	0.625	2.000	1.182	1.339
1.367	0.690	2.050	1.250	1.464
1.469	0.720			
1.595	0.750			
1.658	0.775			
1.761	0.875			
1.823	0.950			
1.886	1.075			
1.911	1.100			

TABLE XII (Cont'd.)

Experimental Data		Data from Faired Curve		
t (seconds)	c (inches)	t (seconds)	c (inches)	v (inches/sec)
1.948	1.125			
2.0115	1.220			
2.0741	1.250			
2.137	1.275			
2.199	1.300			
2.300	1.300			

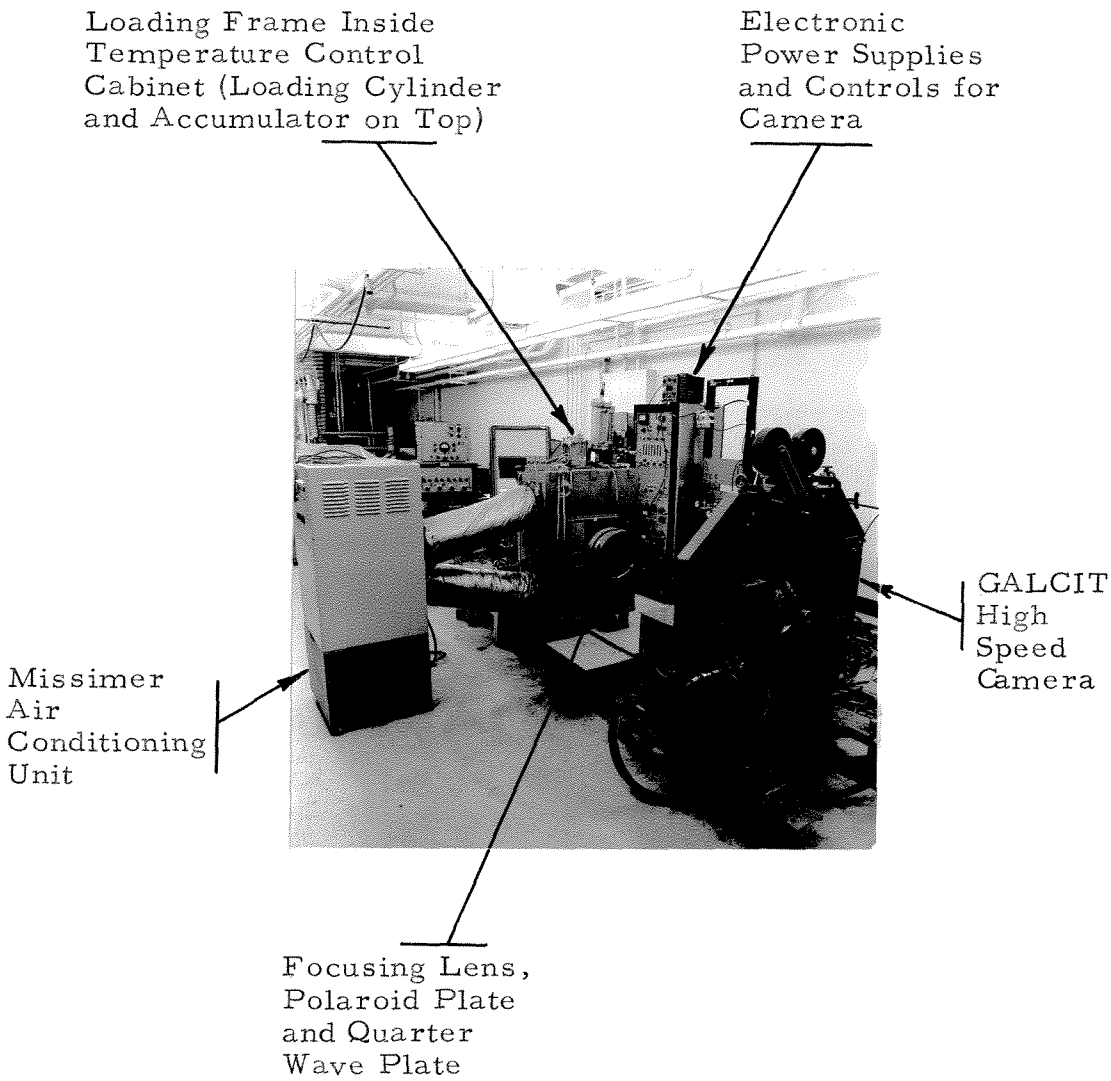

Figure 1. General View of Test Equipment from Camera Side

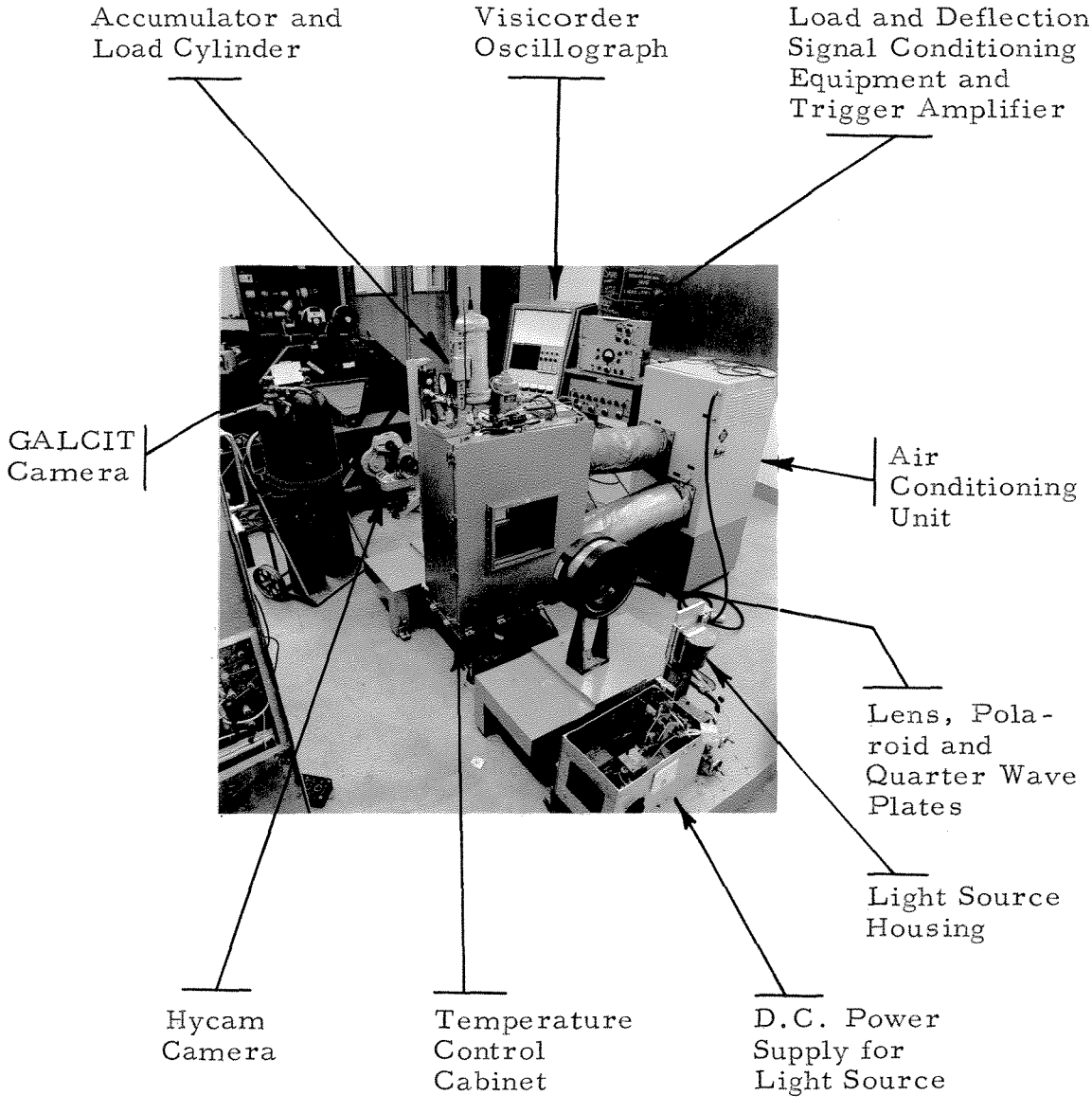

Figure 2. General View of Test Equipment from Light Source Side

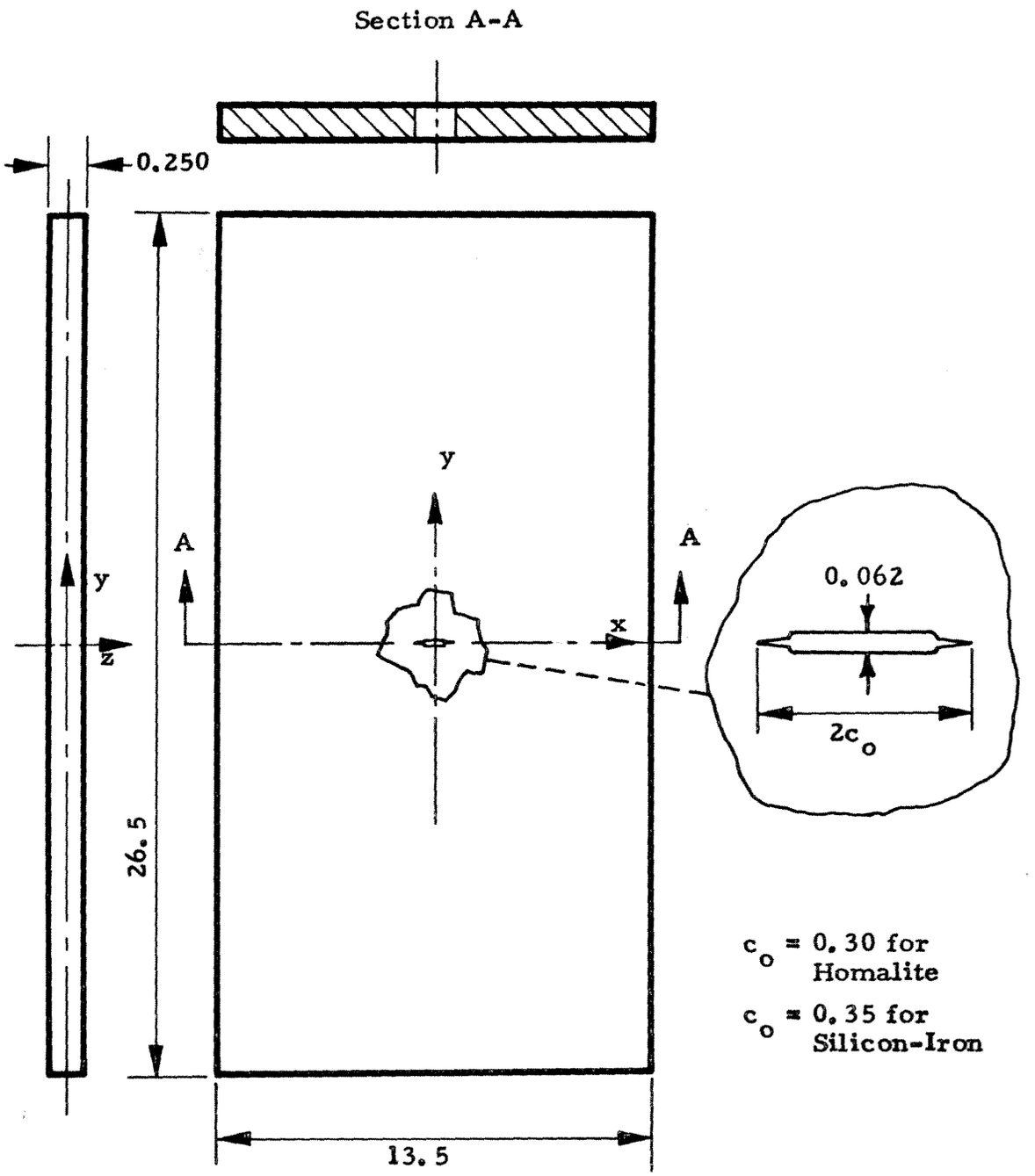

Figure 3 - Drawing of Specimen (All Dimensions in Inches)

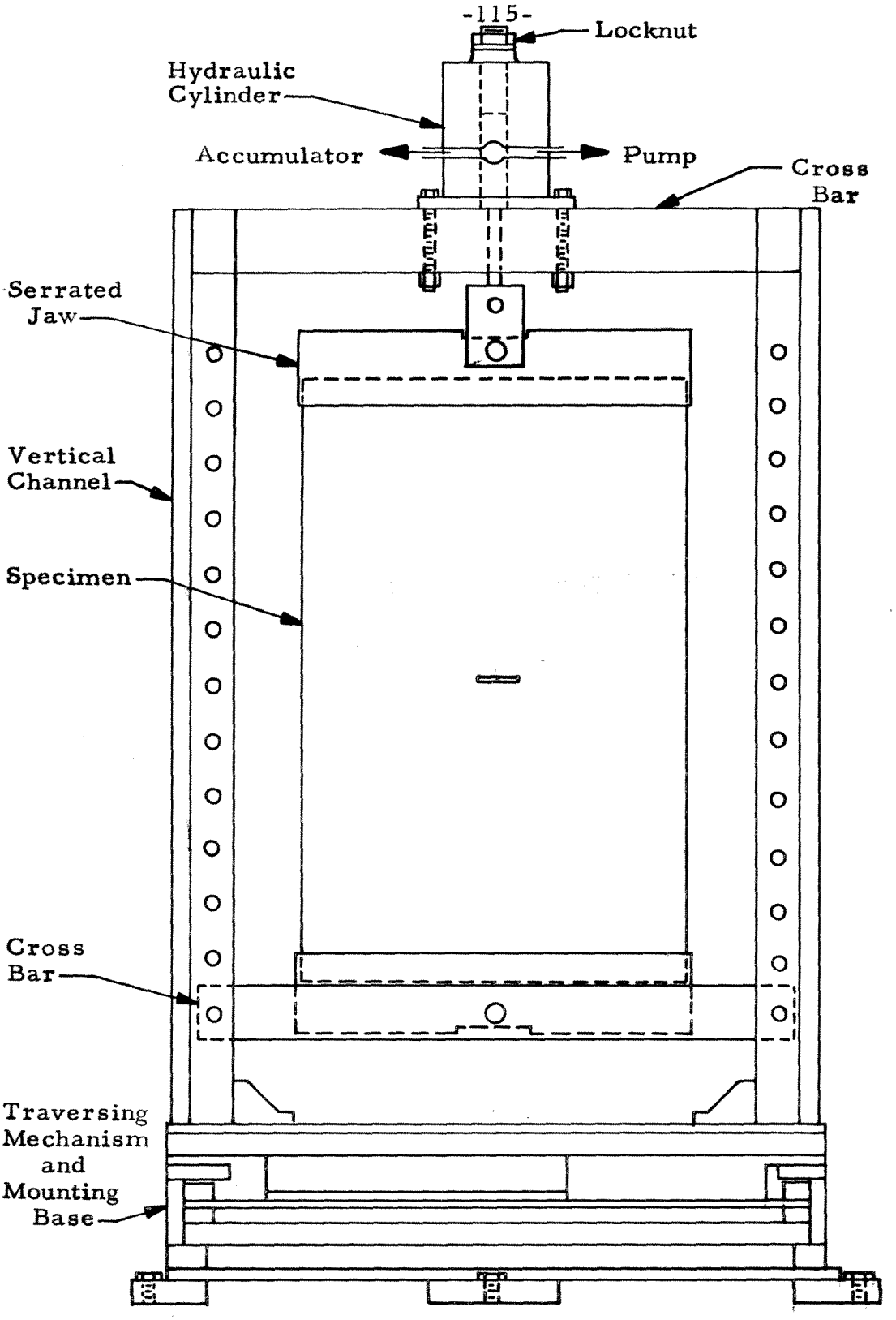

Figure 4. Front View of Loading Frame

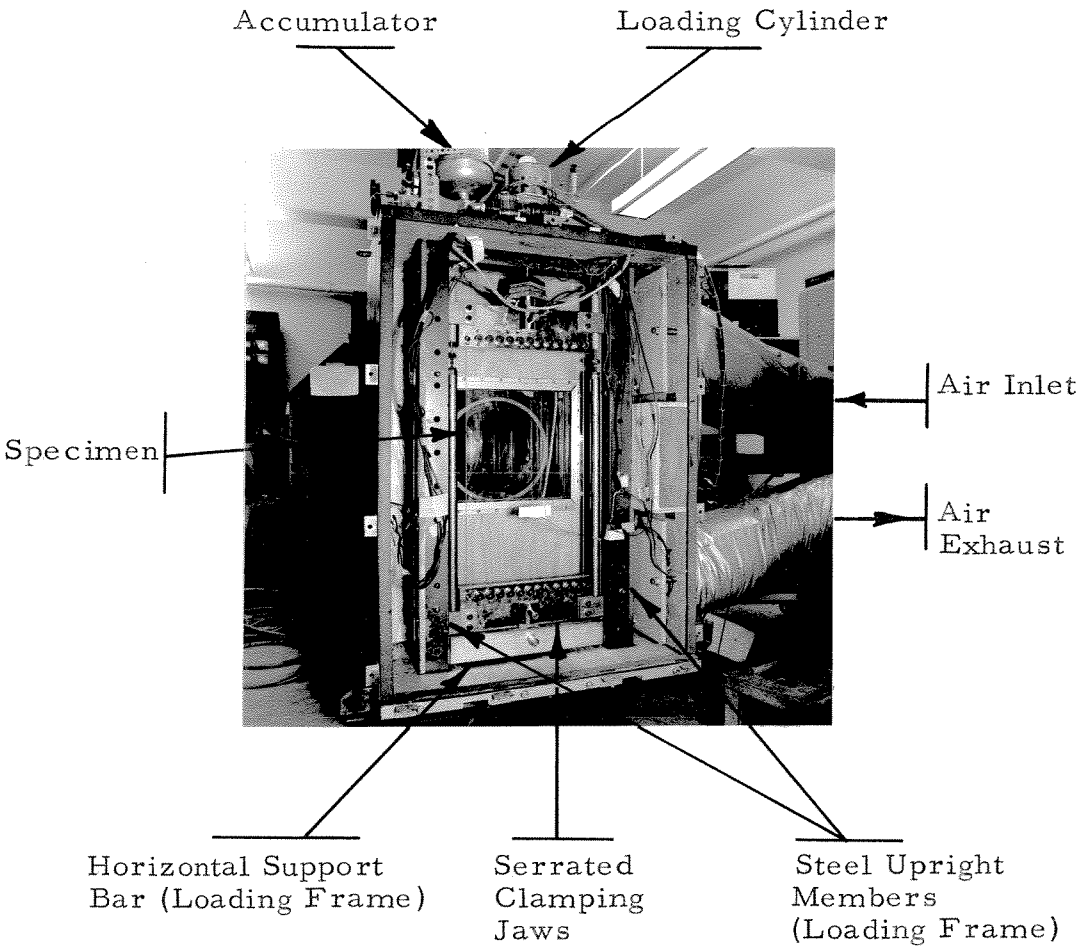

Figure 5. Loading Frame Enclosed in the Temperature Chamber with Specimen Mounted

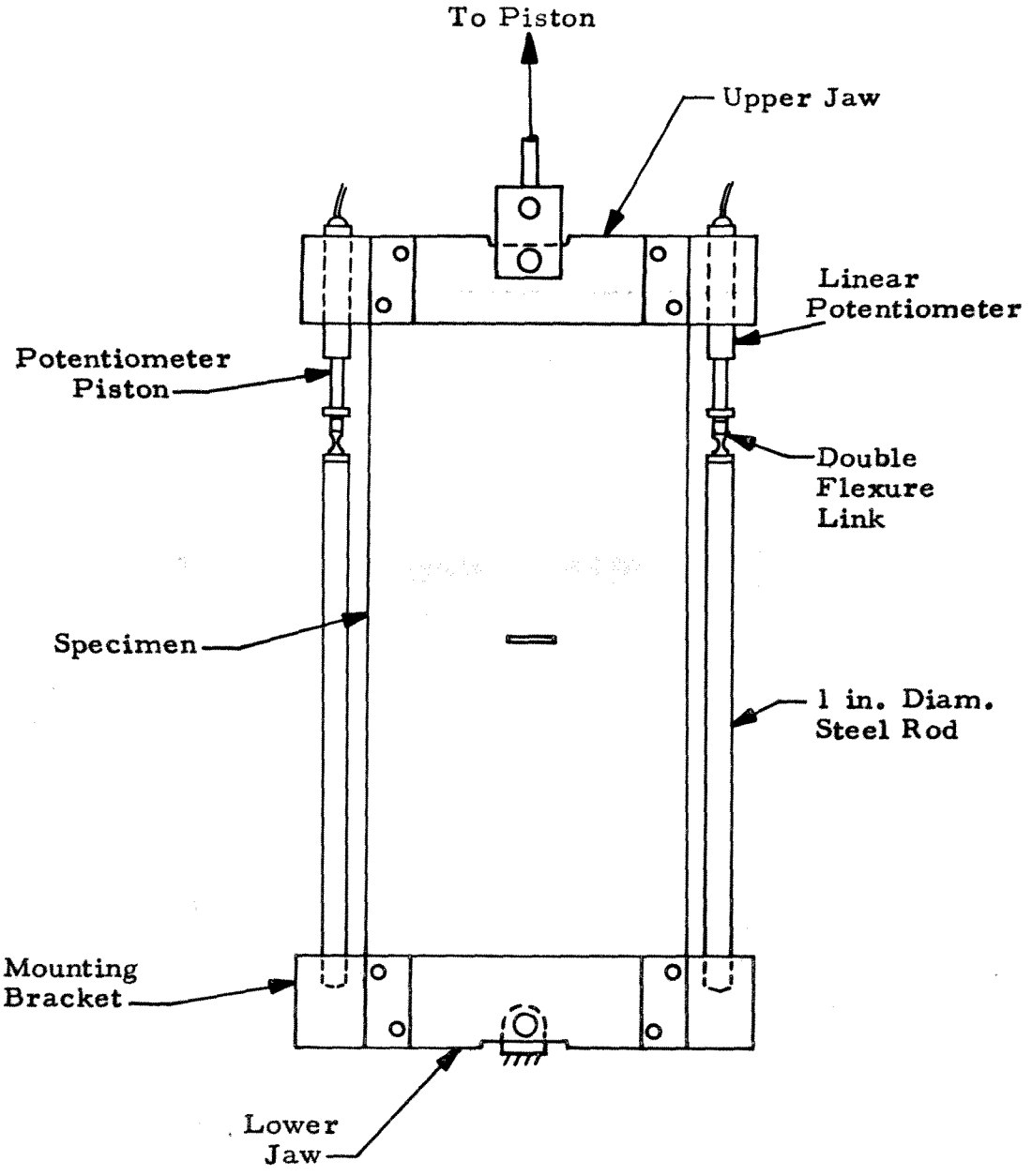

Figure 6. Specimen Clamping Fixtures and Deflection Measuring Equipment.

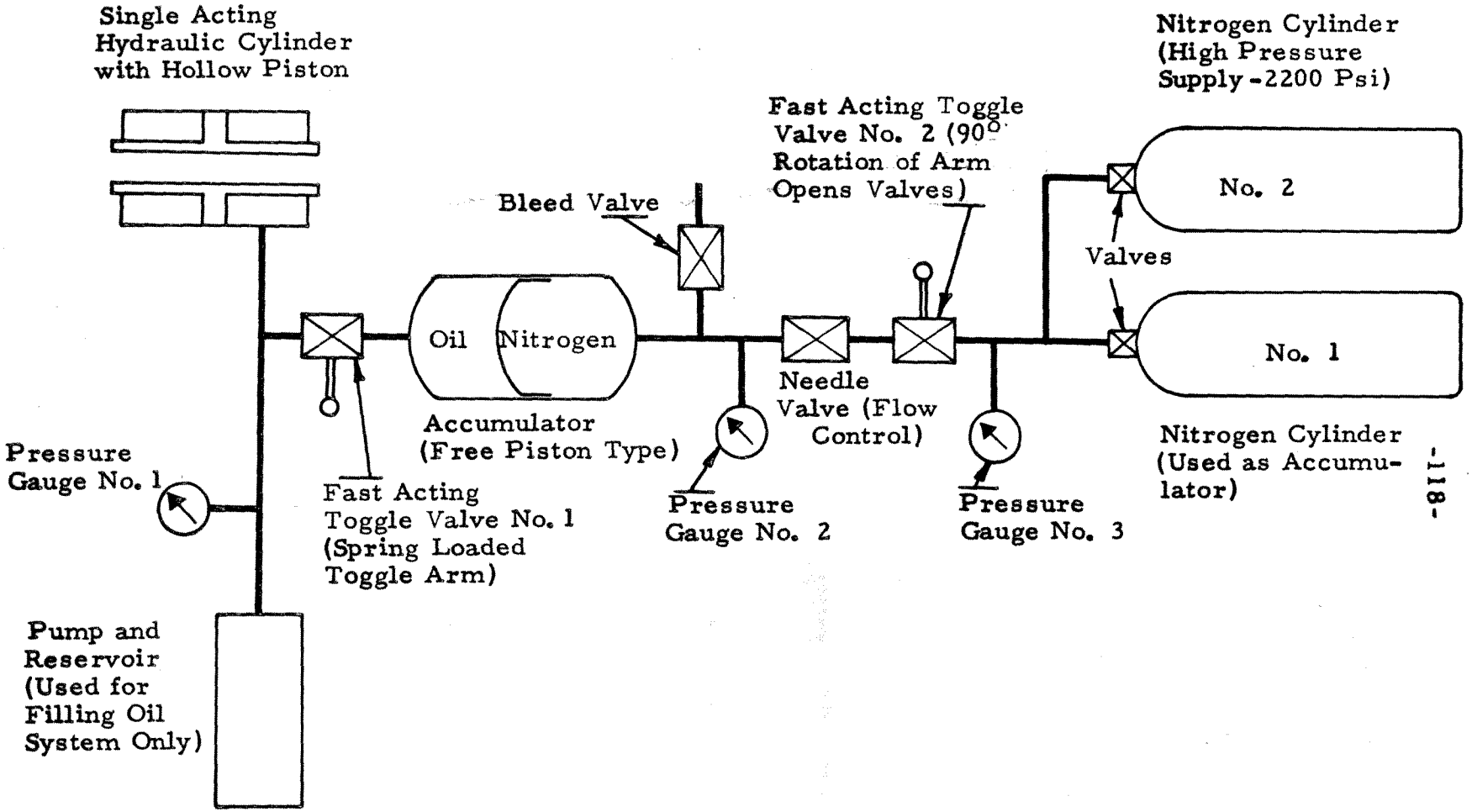

Figure 7 - Hydraulic Control System

HOMALITE TESTS: A = 0.062
SILICON-IRON TESTS: A = 0.250

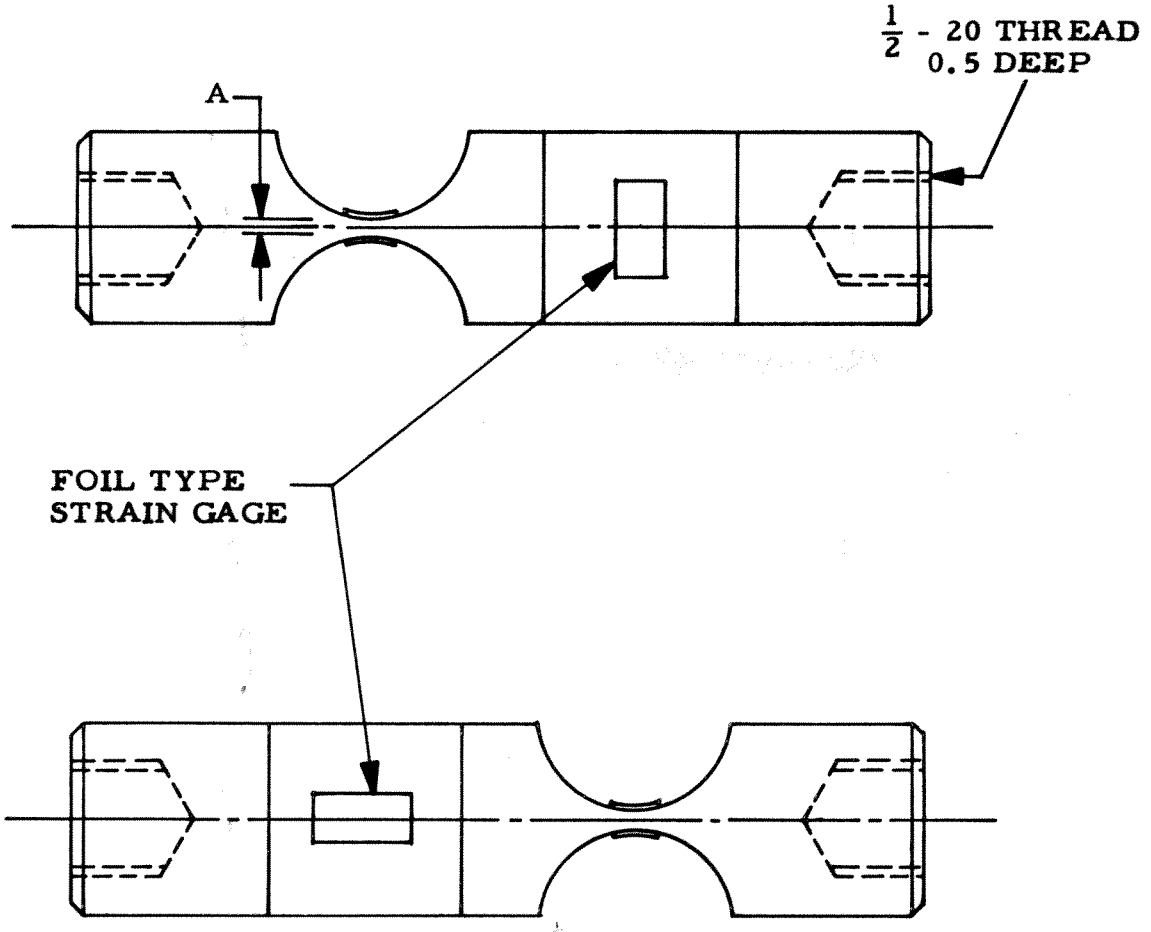

Figure 8. Load Cell

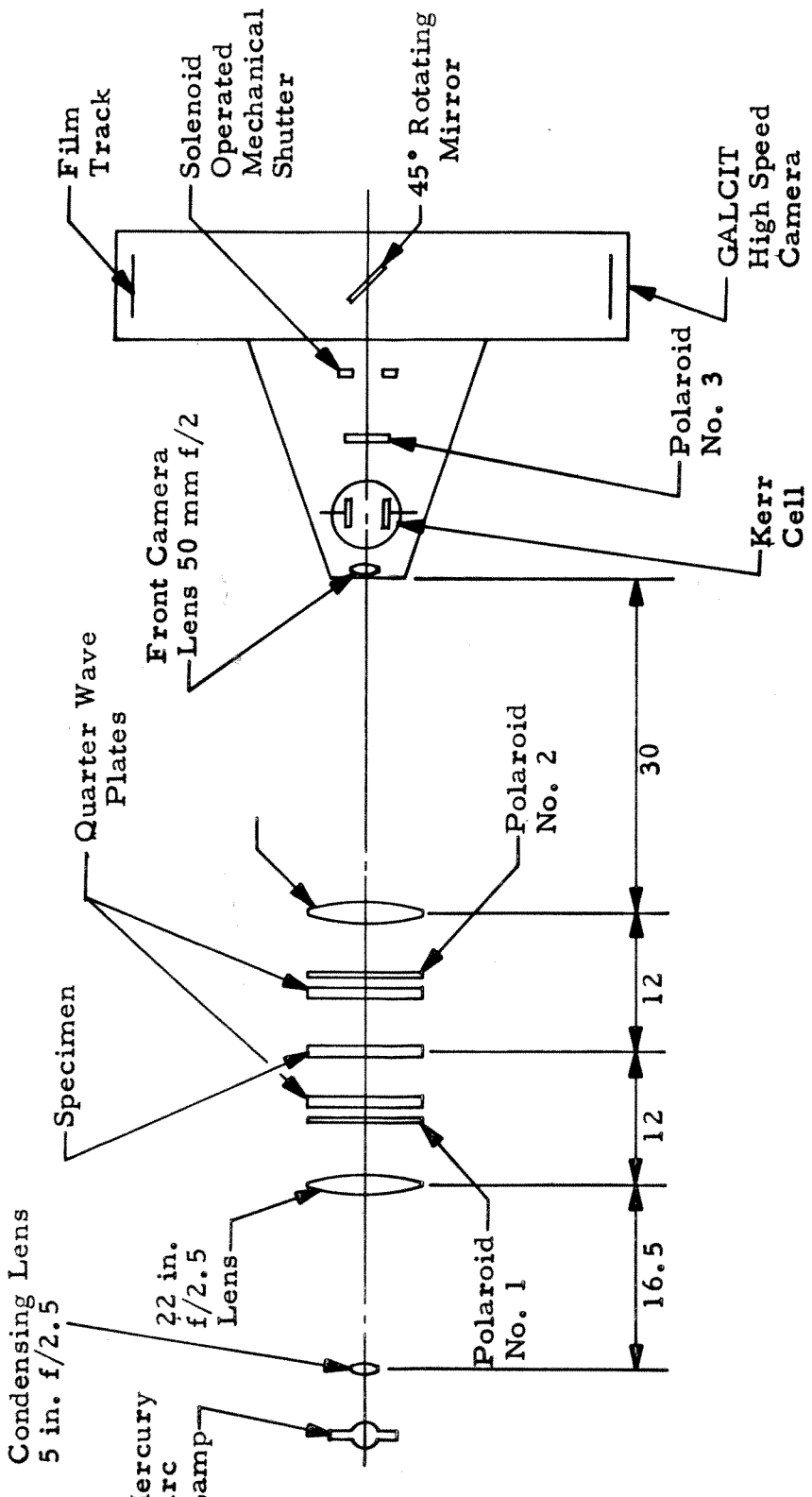

Figure 9. Optical System for High Loading Rate Tests. (All Dimensions in Inches).

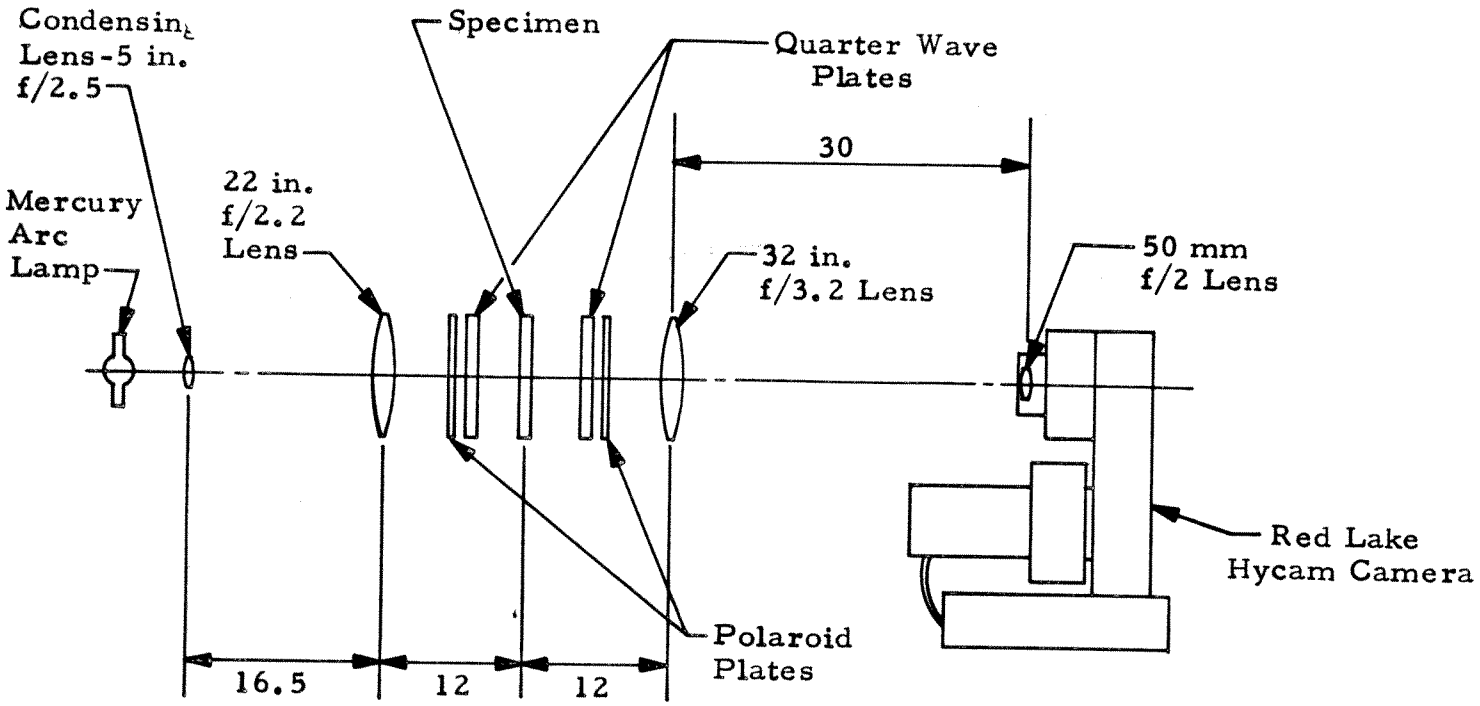

Figure 10. Optical System for High Temperature-Low Loading Rate Tests. (All Dimensions in Inches).

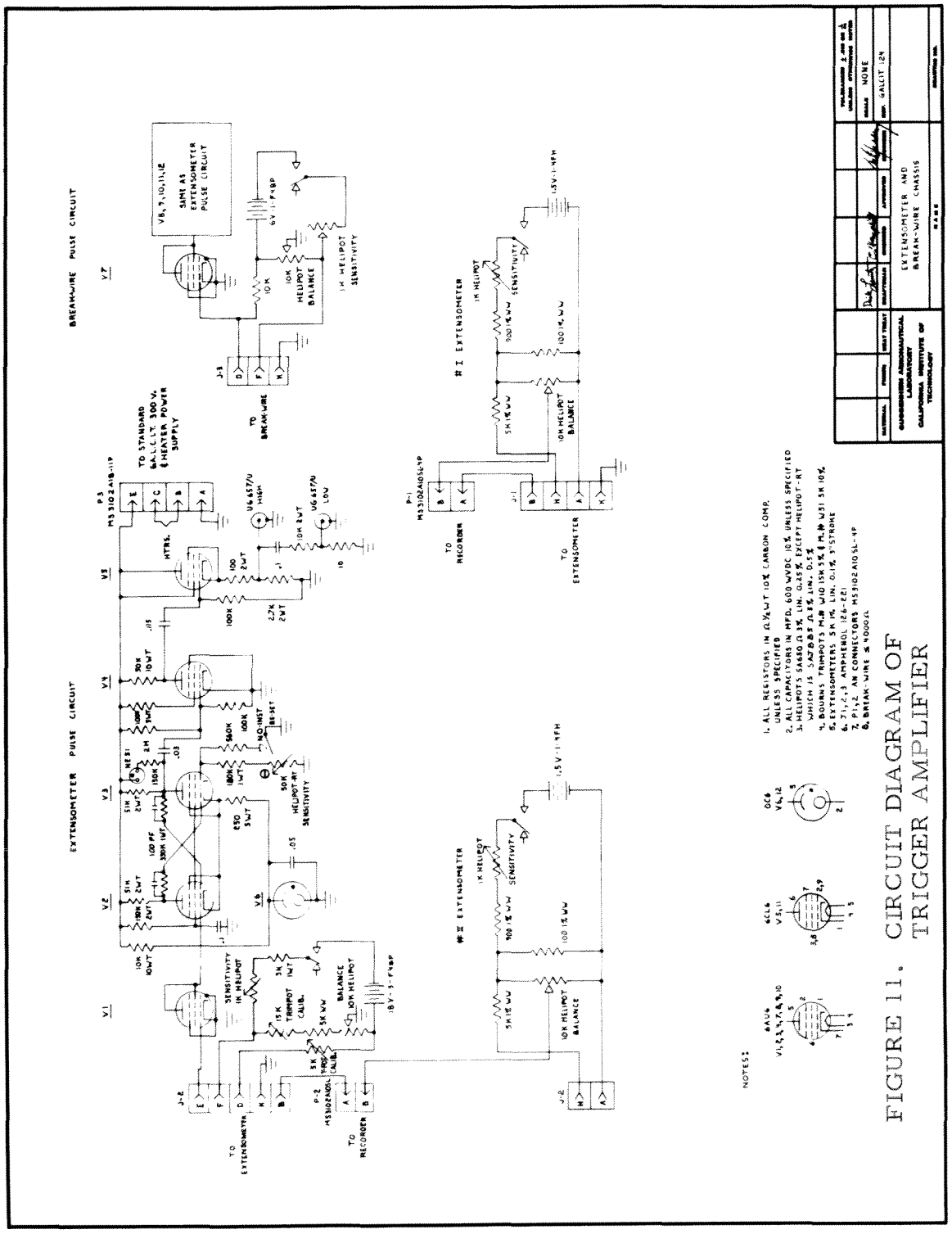

FIGURE 11. CIRCUIT DIAGRAM OF TRIGGER AMPLIFIER

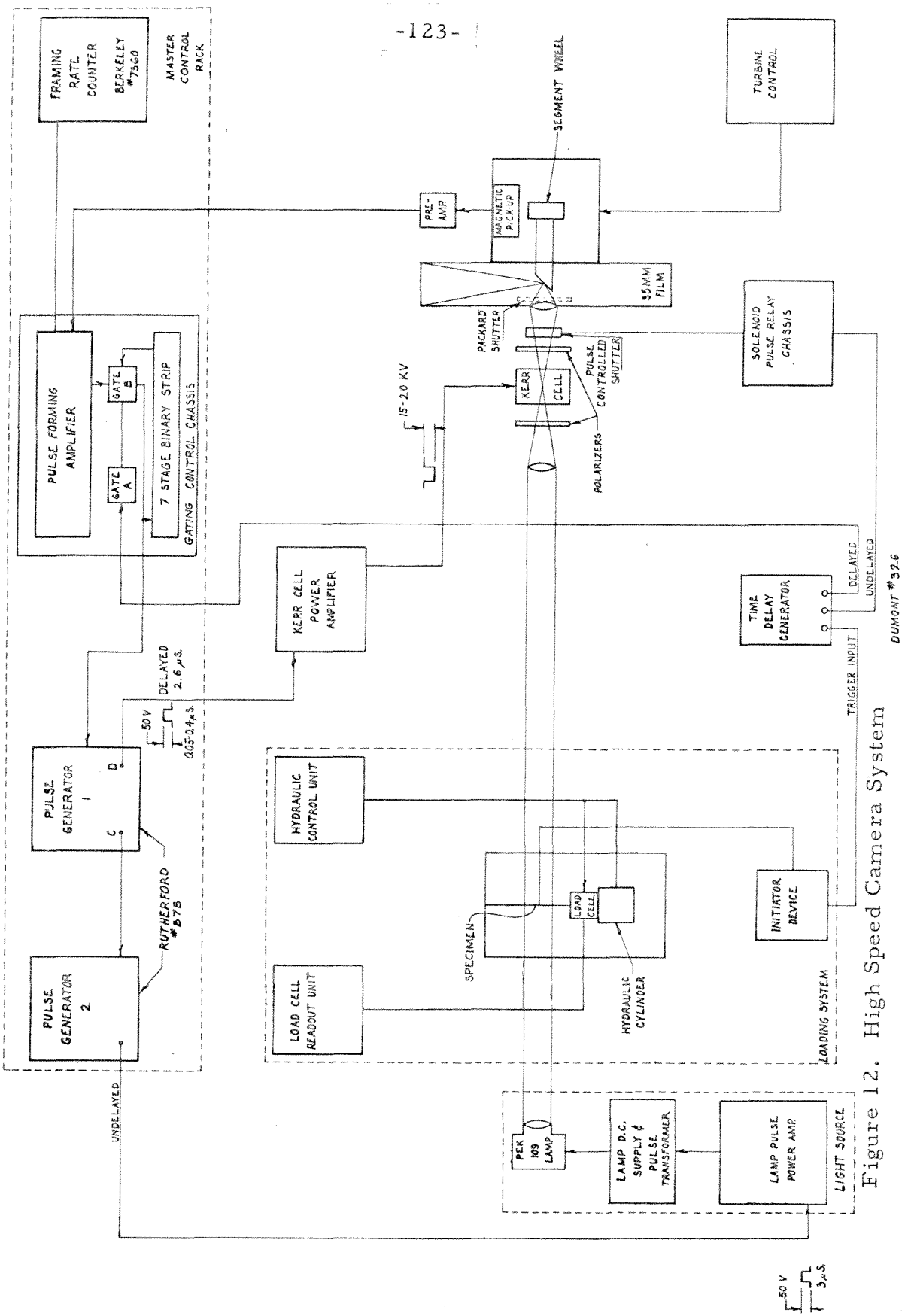

Figure 12. High Speed Camera System

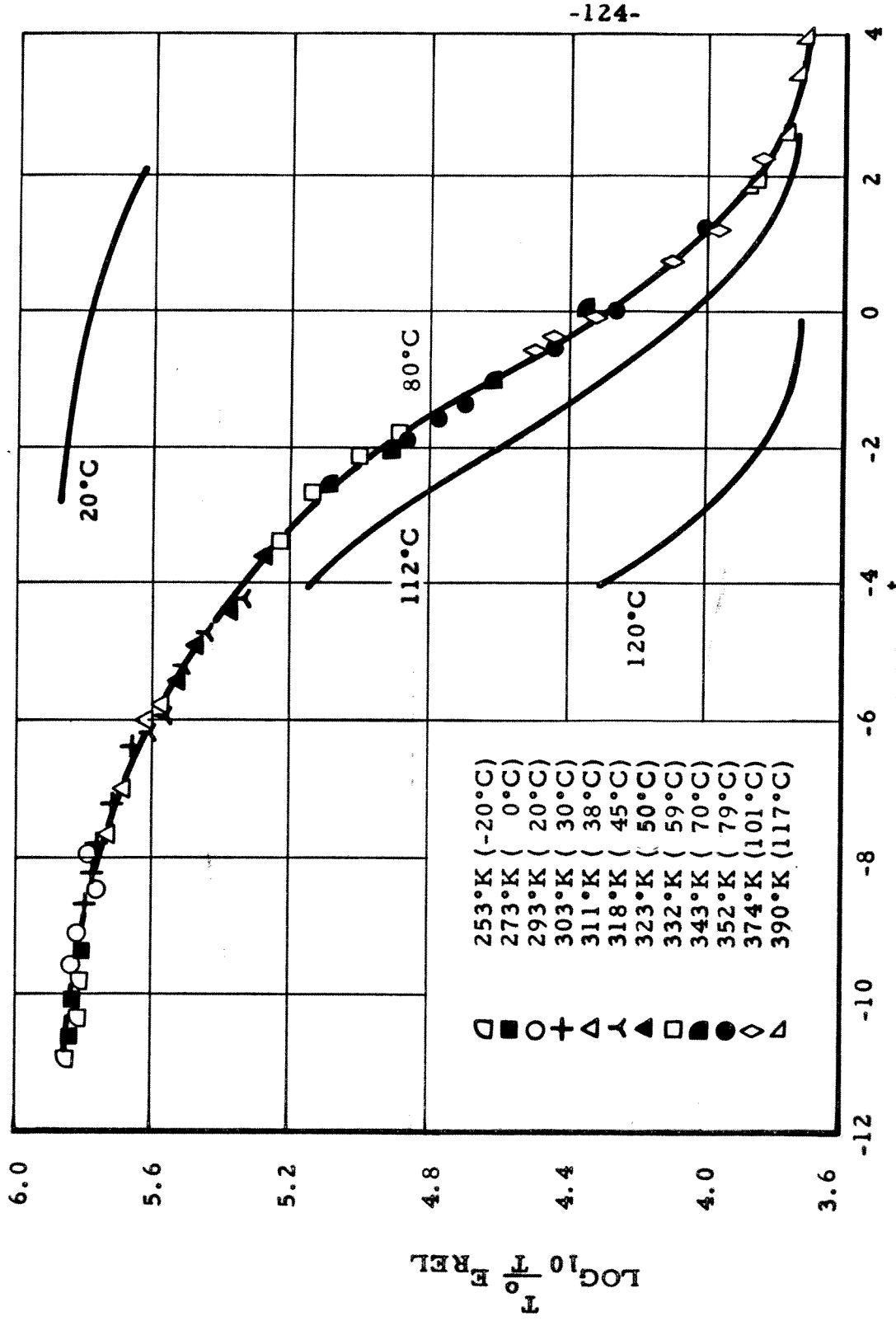

Figure 13. Master Curve of Relaxation Modulus for Homalite 100 (T_o = 80°C)

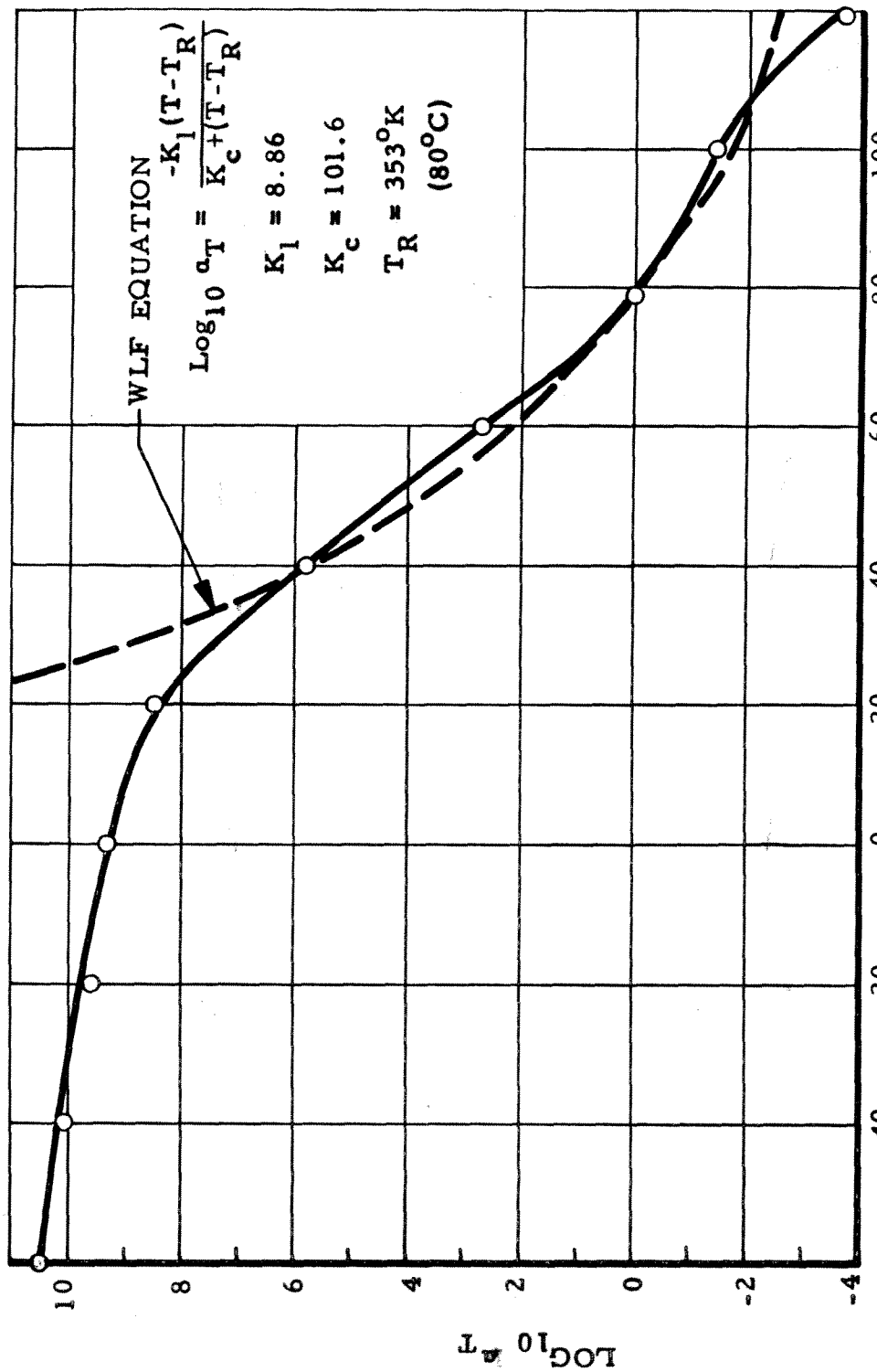

Figure 14. Time-Temperature Shift Factors for Homalite 100

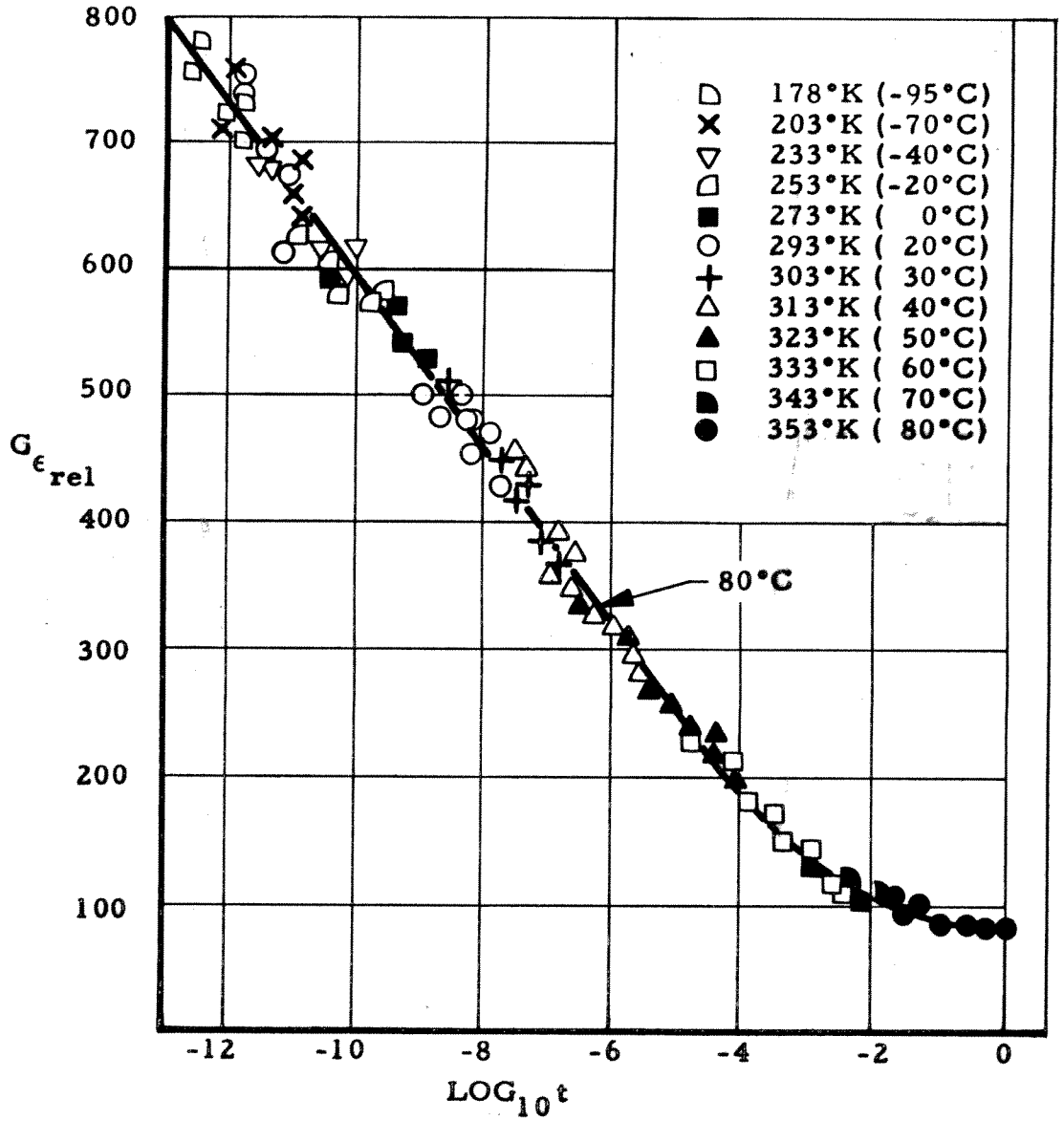

Figure 15. Master Curve for the Strain Optical Coefficient for Homalite 100

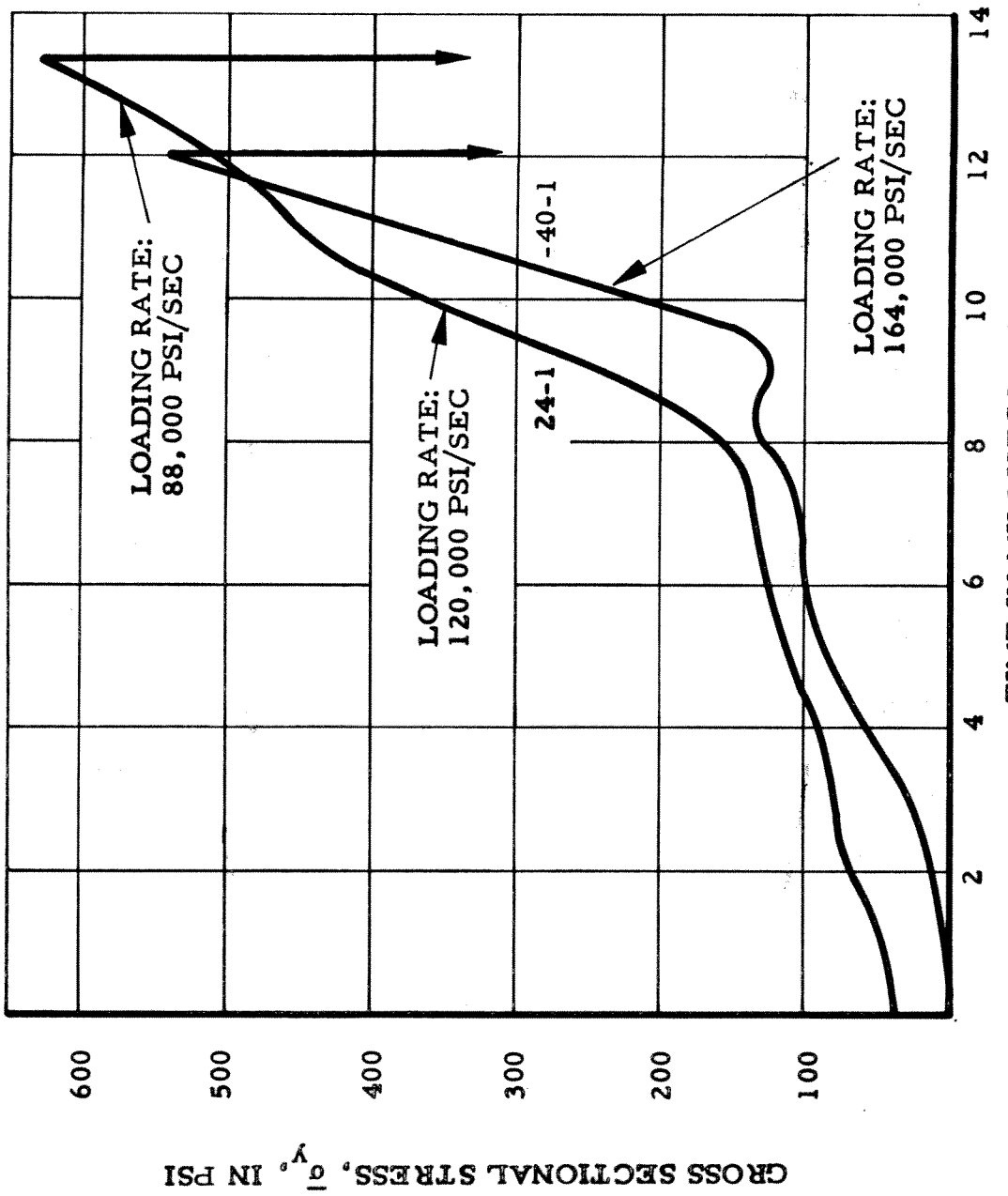

Figure 16. Loading Curves for High Loading Rate Tests at 24°C and -40°C

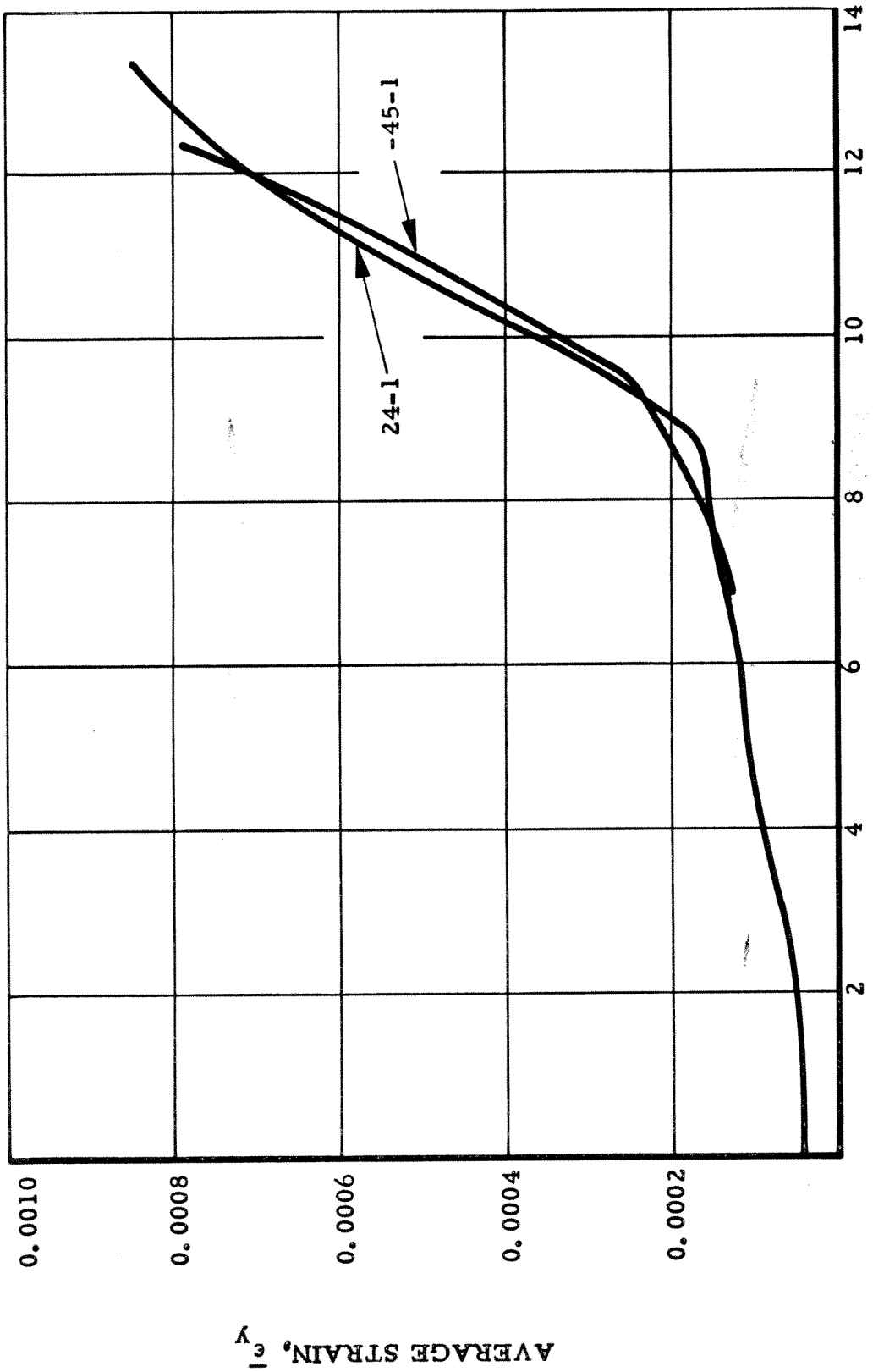

Figure 17 - Average Strain Curves for Tests 24-1 and -45-1

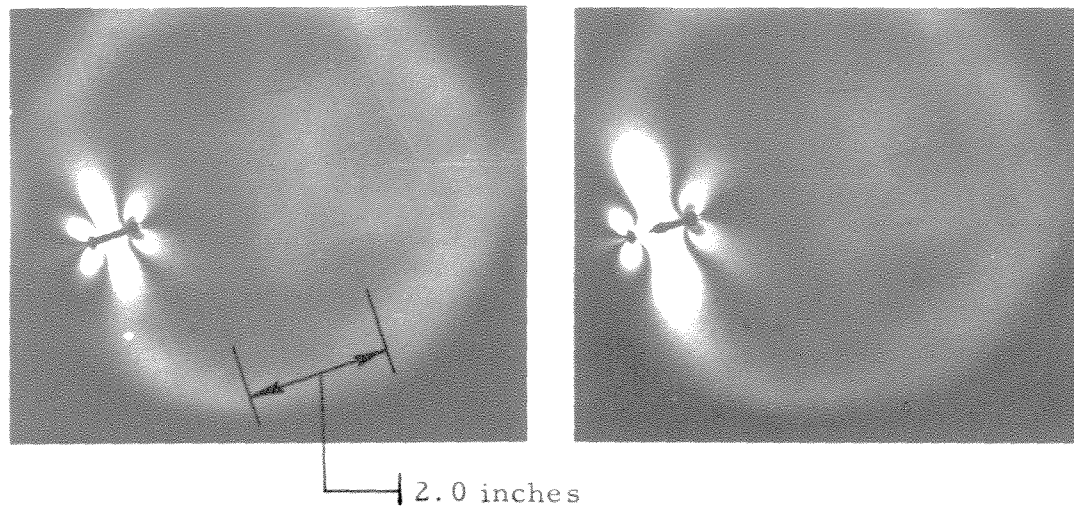

1. t = 0
   c = 0.30

2. t = 65.4 microseconds
   c = 0.30 (right side)
   c = 0.54 (left side)

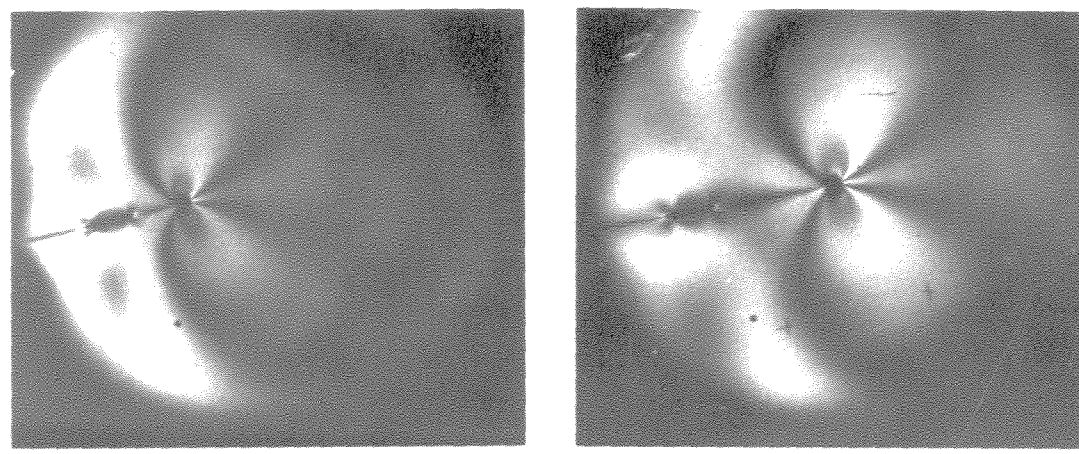

3. t = 130.8 microseconds
   c = 1.10

4. t = 196.2 microseconds
   c = 2.08

Figure 18a. Typical Crack Propagation Photographs from a Test at 24°C. (Framing Rate: 15,300 frames/second. Exposure: 0.2 Microseconds. c is in inches)

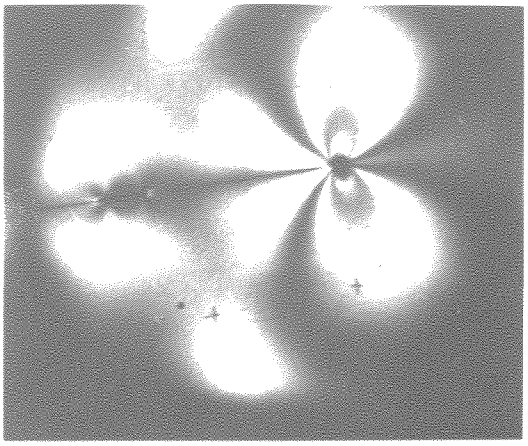

5. t = 261.6 microseconds
c = 3.09

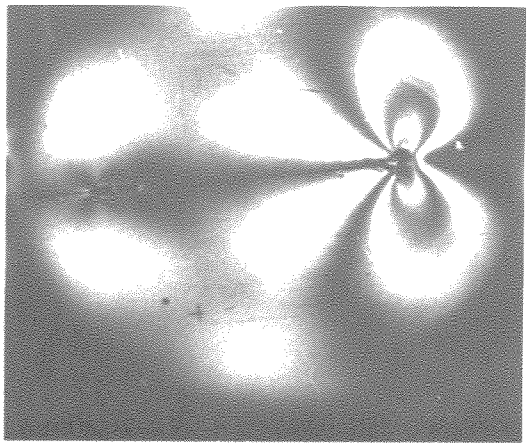

6. t = 327.0 microseconds
c = 4.07

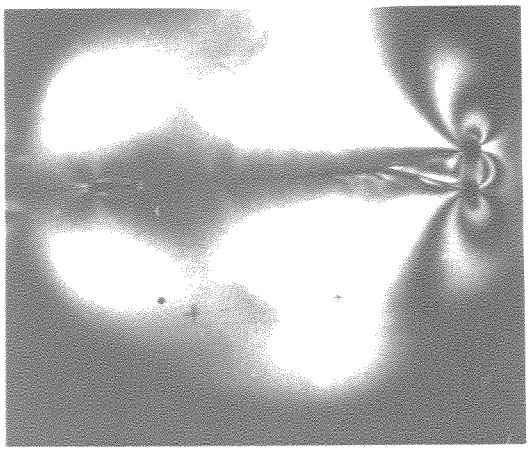

7. t = 392.4 microseconds
c = 5.01

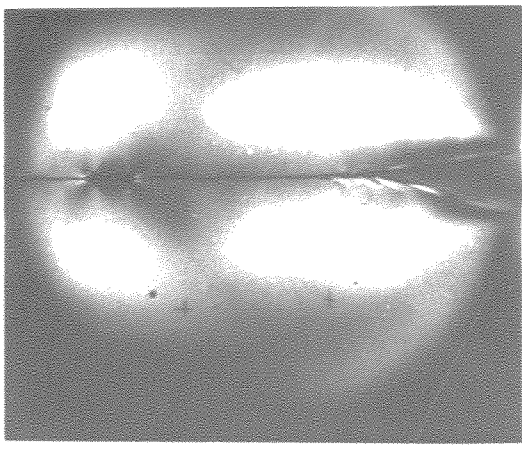

8. t = 467.8 microseconds
c > 5.50

Figure 18b. Typical Crack Propagation Photographs from Test at 24°C. (Continued)

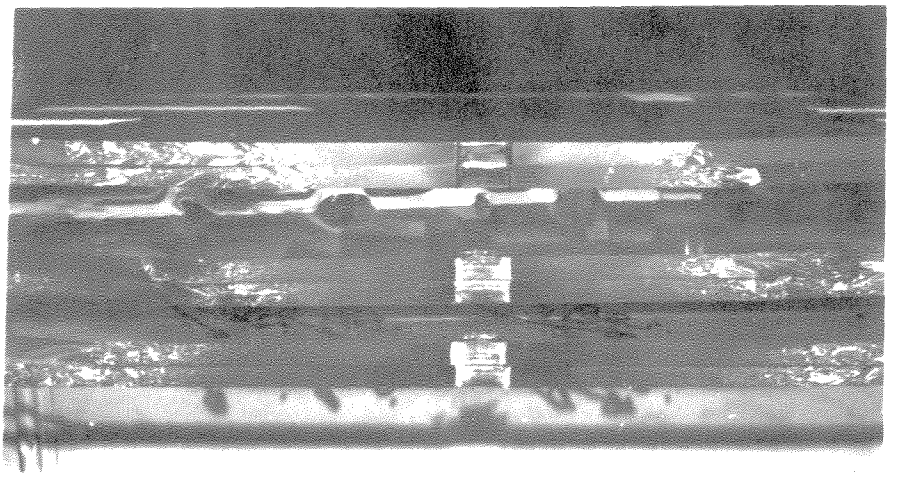

	Crack Length to Crack Branch (inches)	Applied Stress at Fracture Initiation (psi)
Top Specimen	2.0	715
Middle Specimen	2.3	762
Bottom Specimen	3.2	628

Figure 19. Photographs of Fracture Surfaces on Three Specimens from High Loading Rate Tests at 24°C.

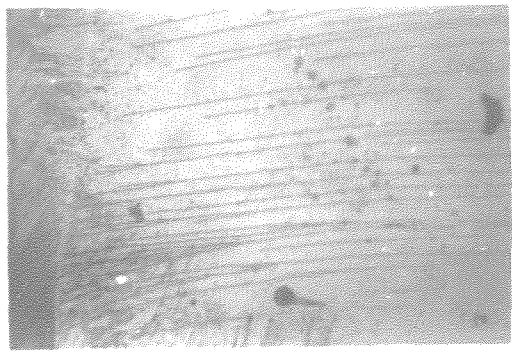

1. x = 0.3 inches
Centerline - Notch Vertex

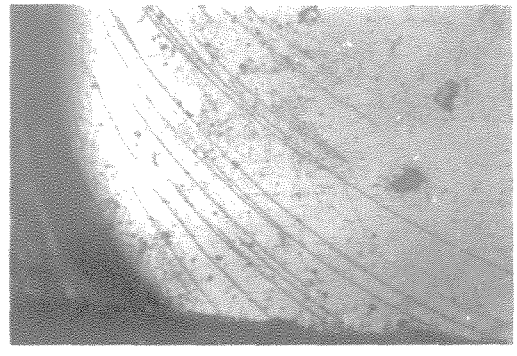

2. x = 0.3 inches
Specimen Edge

3. x = 0.44 inches
Edge

4. x = 0.70
Edge

5. x = 0.70 inches
Edge

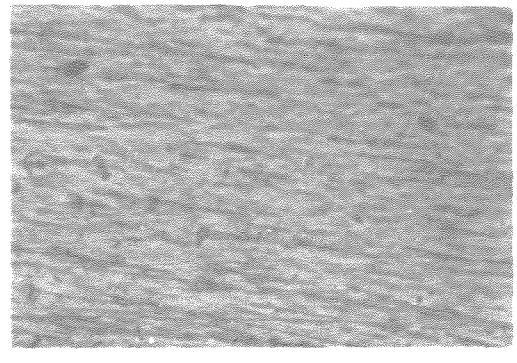

6. x = 1.30 inches
Edge

Figure 20a. Photomicrographs of Fracture Surface at Various Stations along the Crack Path for Specimen 24-1 Magnification 100x (See Figure 3, Section A-A)

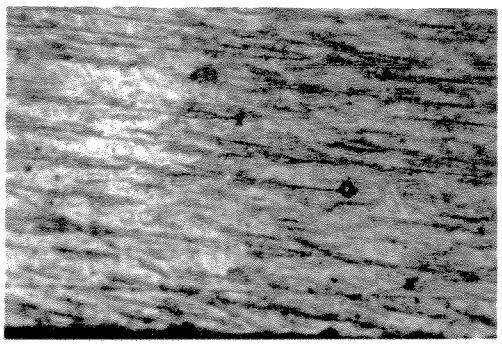

7. x = 1.55 inches
Edge

8. x = 2.05 inches
Edge

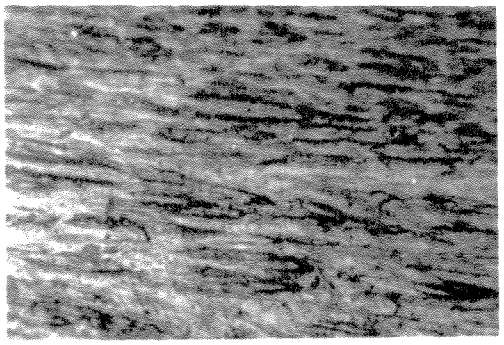

9. x = 2.55 inches
Edge

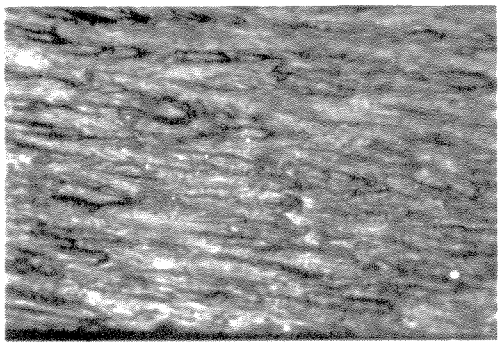

10. x = 3.05 inches
Edge

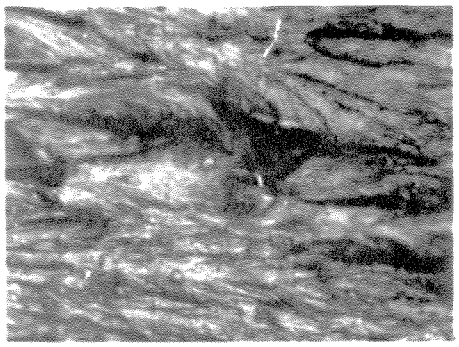

11. x = 5.1 inches
Centerline

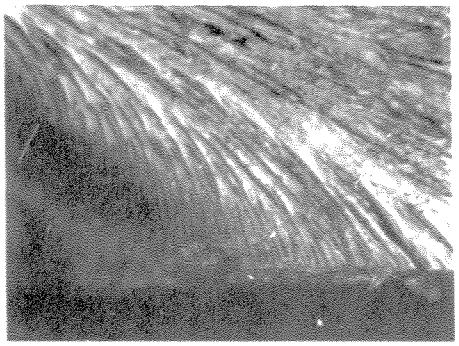

12. x = 5.1 inches
Edge

Figure 20b. Photomicrographs of Fracture Surface at Various Stations along the Crack Path for Specimen 24-1 Magnification 100x

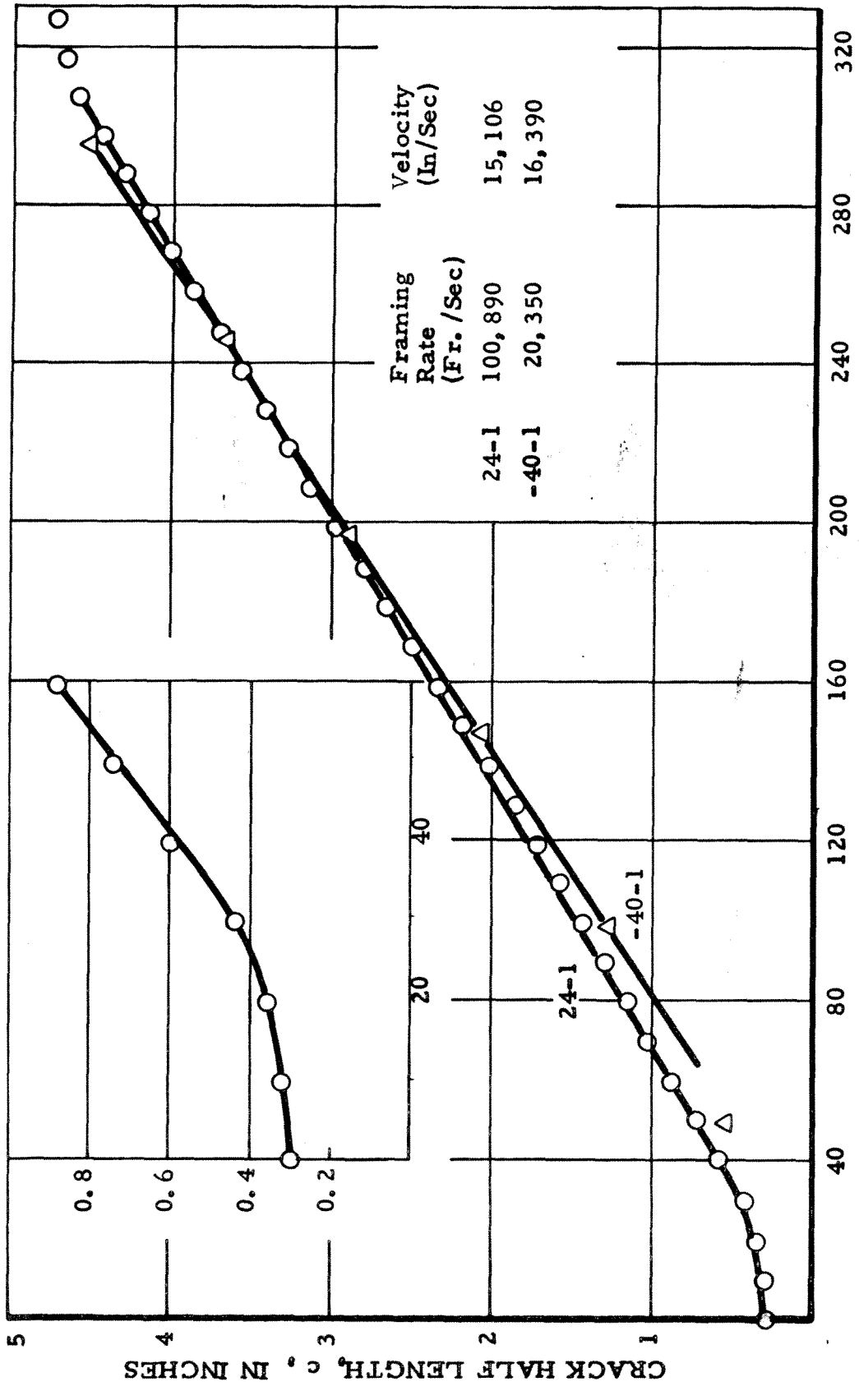

Figure 21 - Crack Length Versus Propagation Time for High Loading Rate Runs at 24°C and -40°C

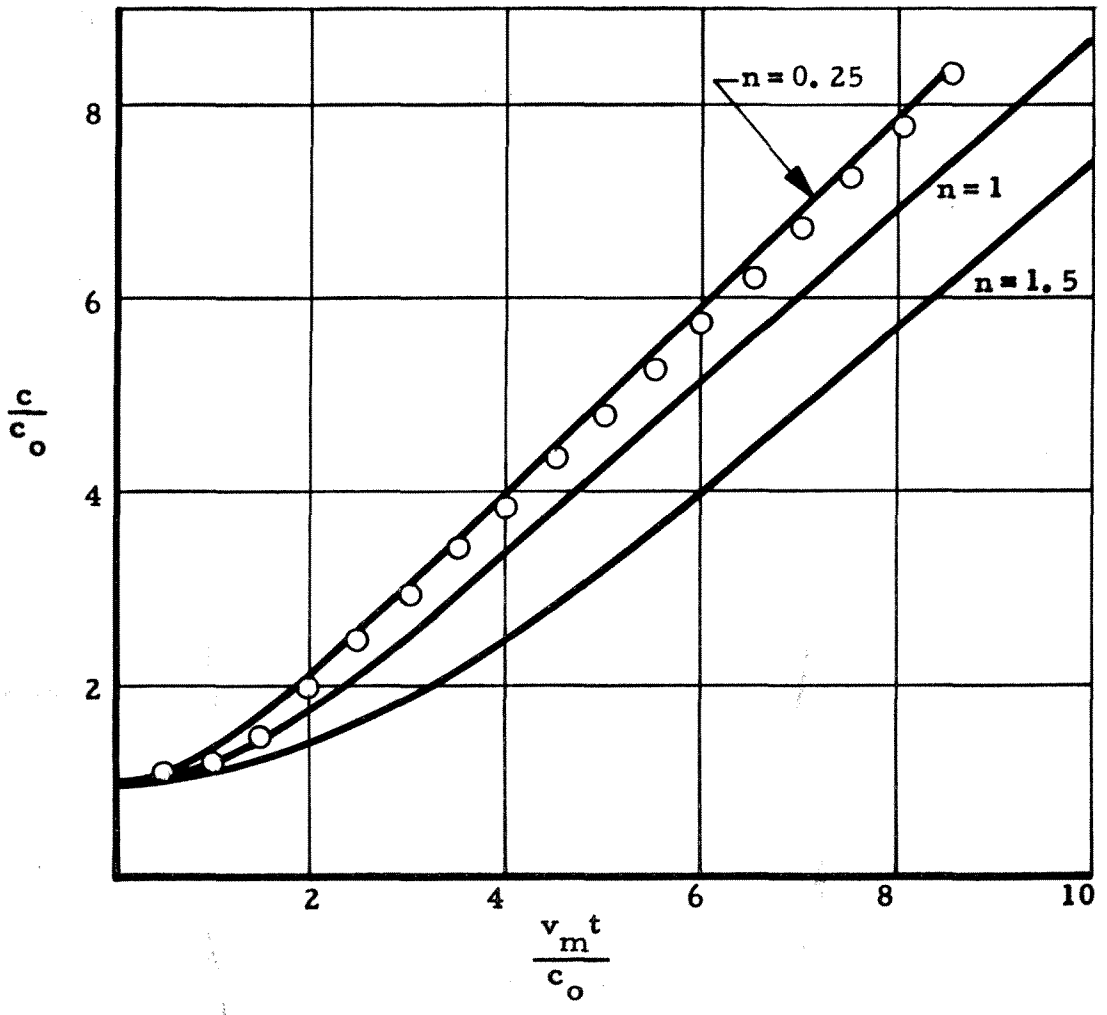

Data Points from $\frac{c}{}$ vs. t Curve for Run 24-1

Curves are for Constant Force Condition:

$$\frac{v_m t}{c_o} = (\alpha-1)^{\frac{1}{2}}[\alpha-(n-1)]^{\frac{1}{2}} + n\,\ell n\left\{(\alpha-1)^{\frac{1}{2}}+[\alpha-(n-1)]^{\frac{1}{2}}\right\} - \frac{n}{2}\ell n(2-n)$$

$\alpha = \frac{c}{c_o}$; v_m = maximum velocity

$$n = \frac{4E\gamma}{\pi c_o \sigma_c^2} = \frac{2\sigma_g^2}{\sigma_c^2}$$

Figure 22 - Correlation Between J. P. Berry's Theory for Crack Propagation in Elastic Material and the Experimental Data from a High Loading Rate Test

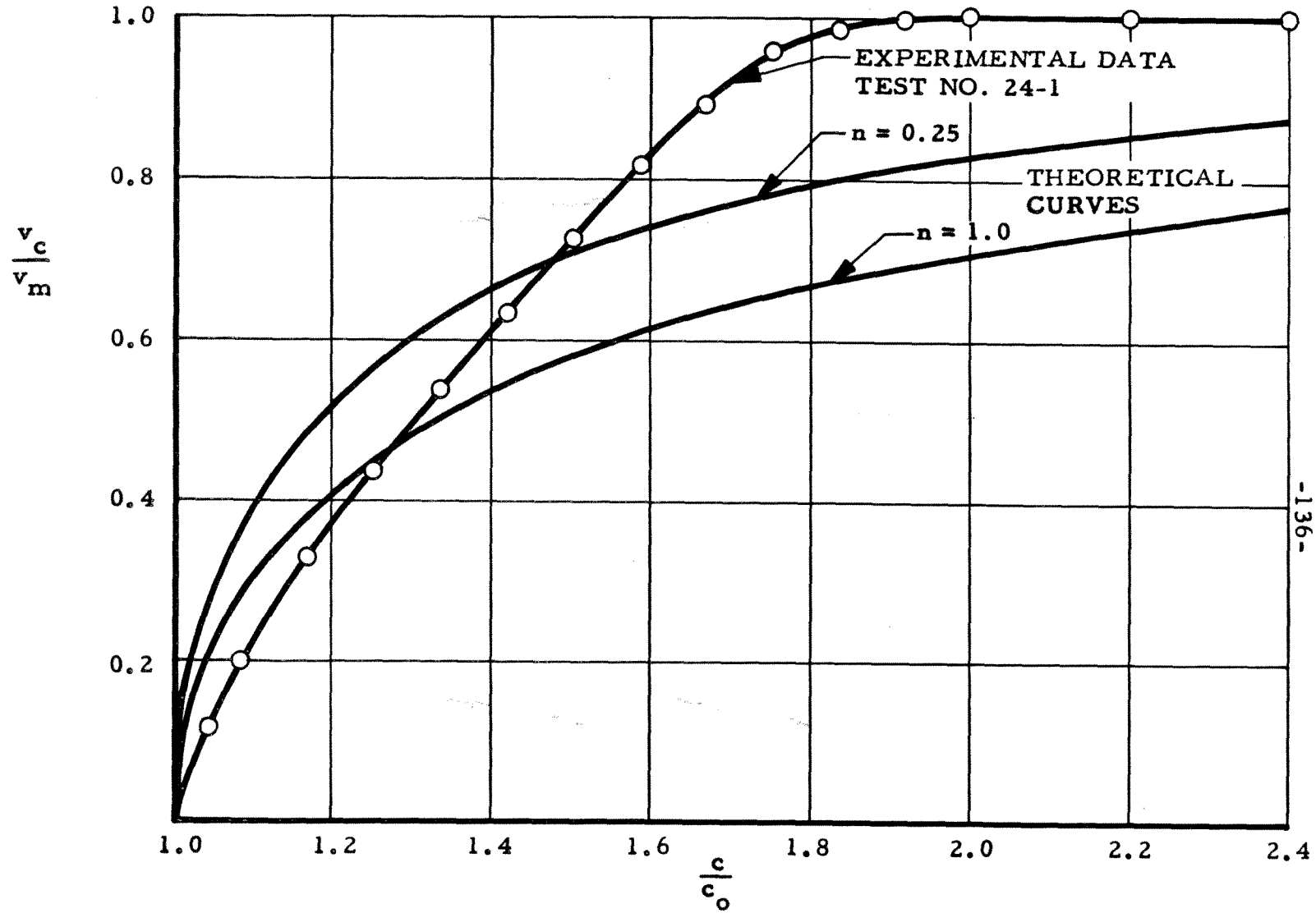

Figure 23. A Comparison of Experimental Velocity Data with Theory by Berry

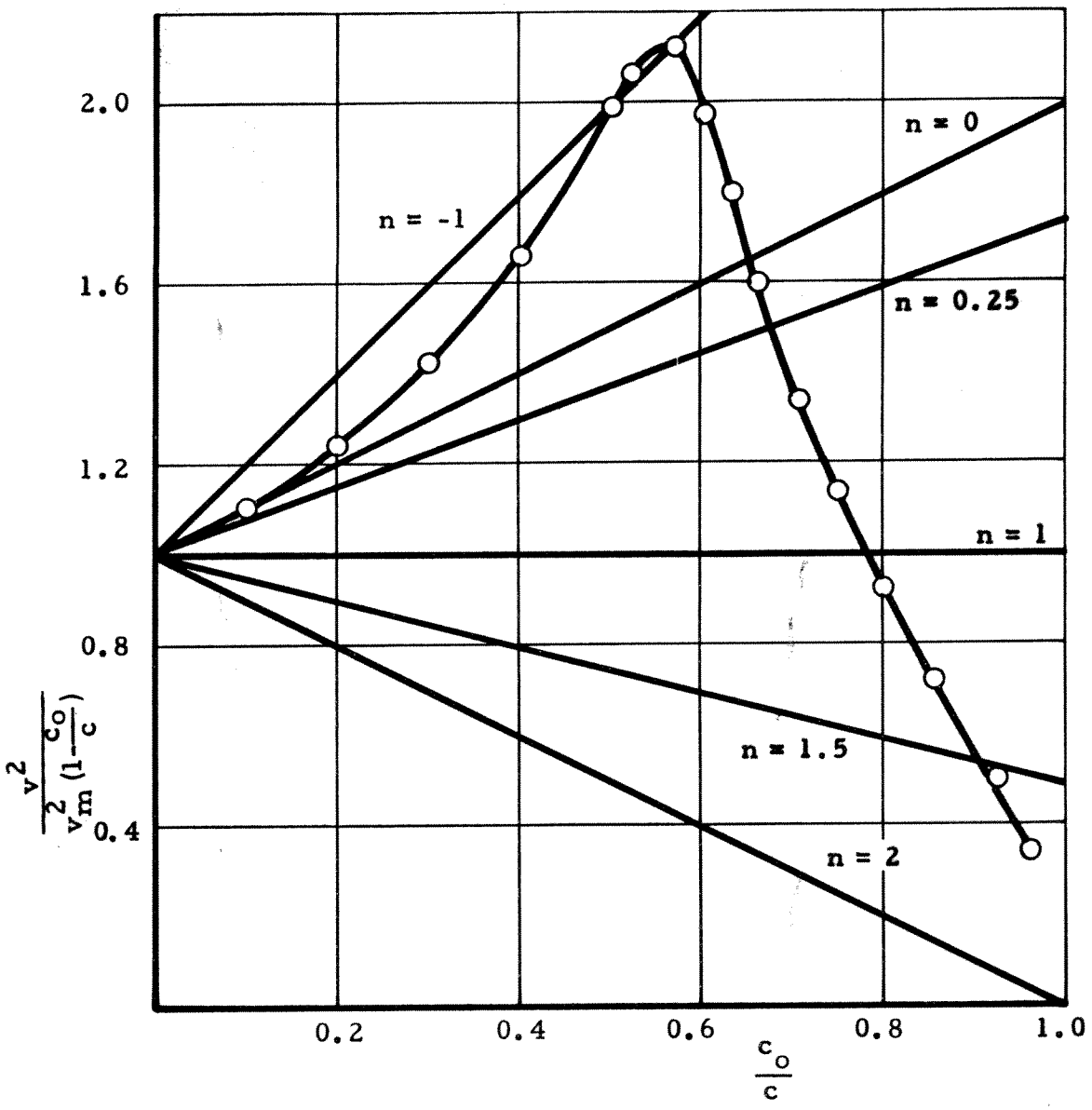

Figure 24. Comparison of Experimental Crack Velocity Data with Berry Theory. (Data Points are on Experimental Curve. Straight Lines for Various n Values are Theoretical Curves.)

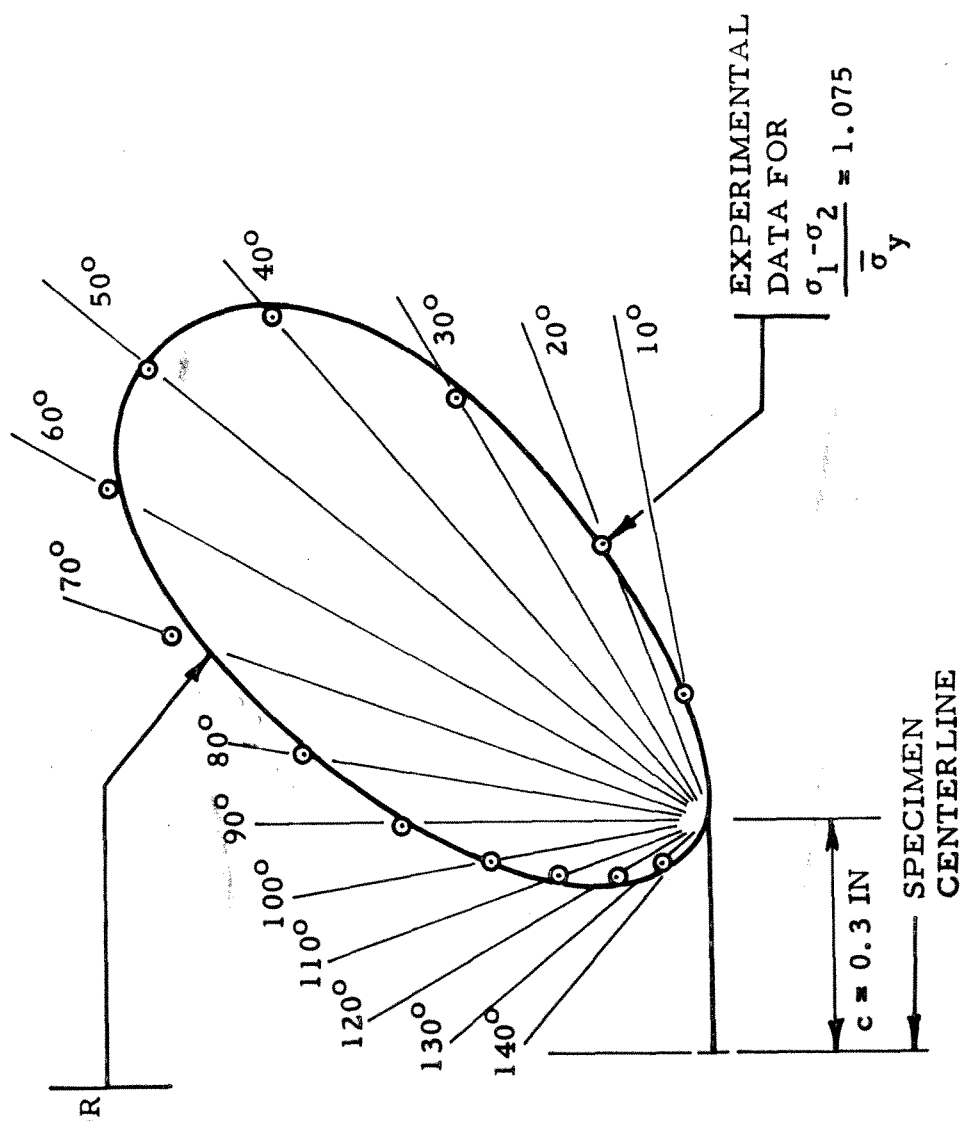

Figure 25. Comparison of Experimental Isochromatic Patterns from Test 24-1 with Theoretical Patterns for a Stationary Crack

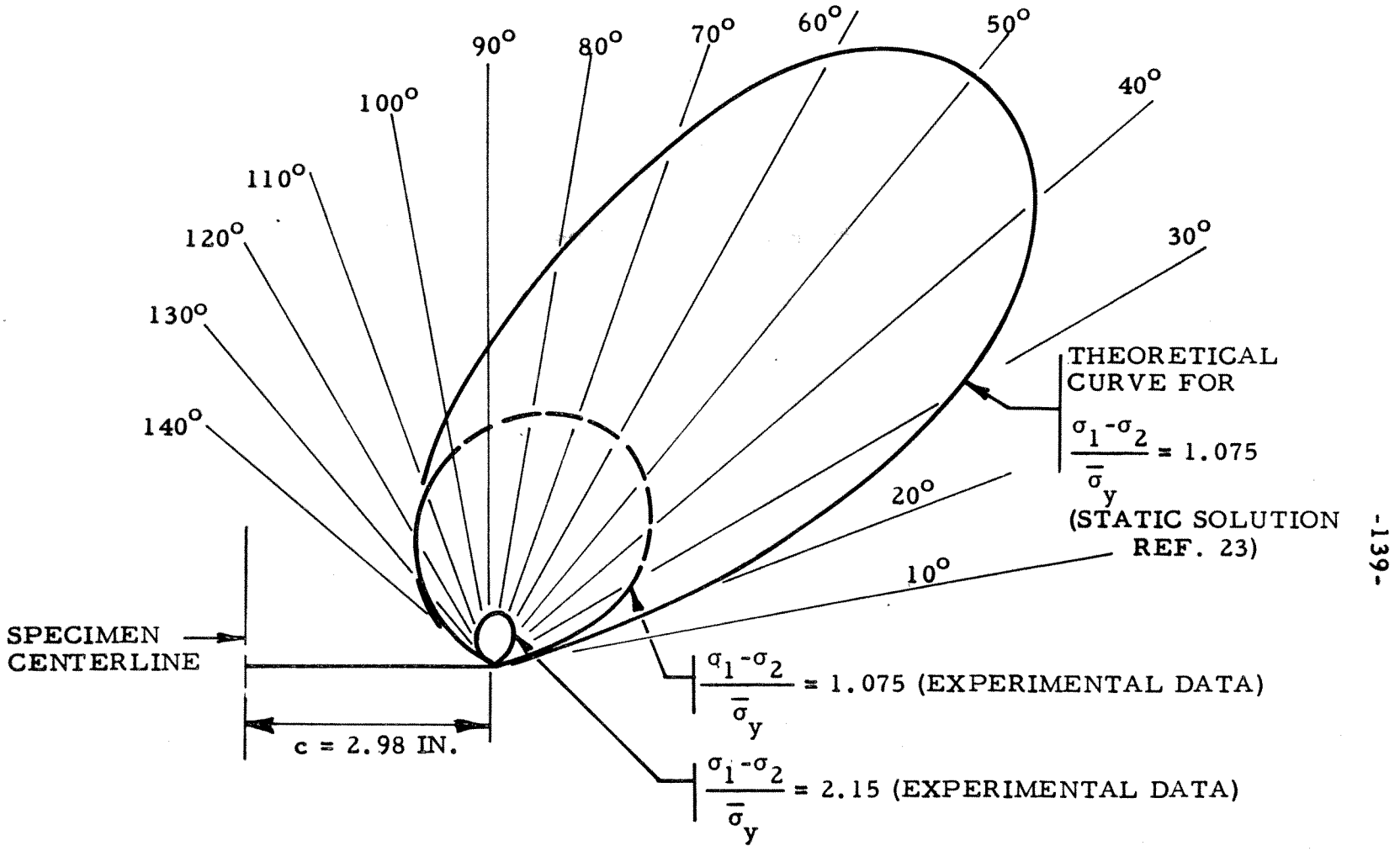

Figure 26a. Comparison of Experimental Isochromatic Patterns from Test 24-1 for Constant Crack Velocity Condition (Frame 5 - Figure 18b) with the Theoretical Pattern for a Stationary Crack.

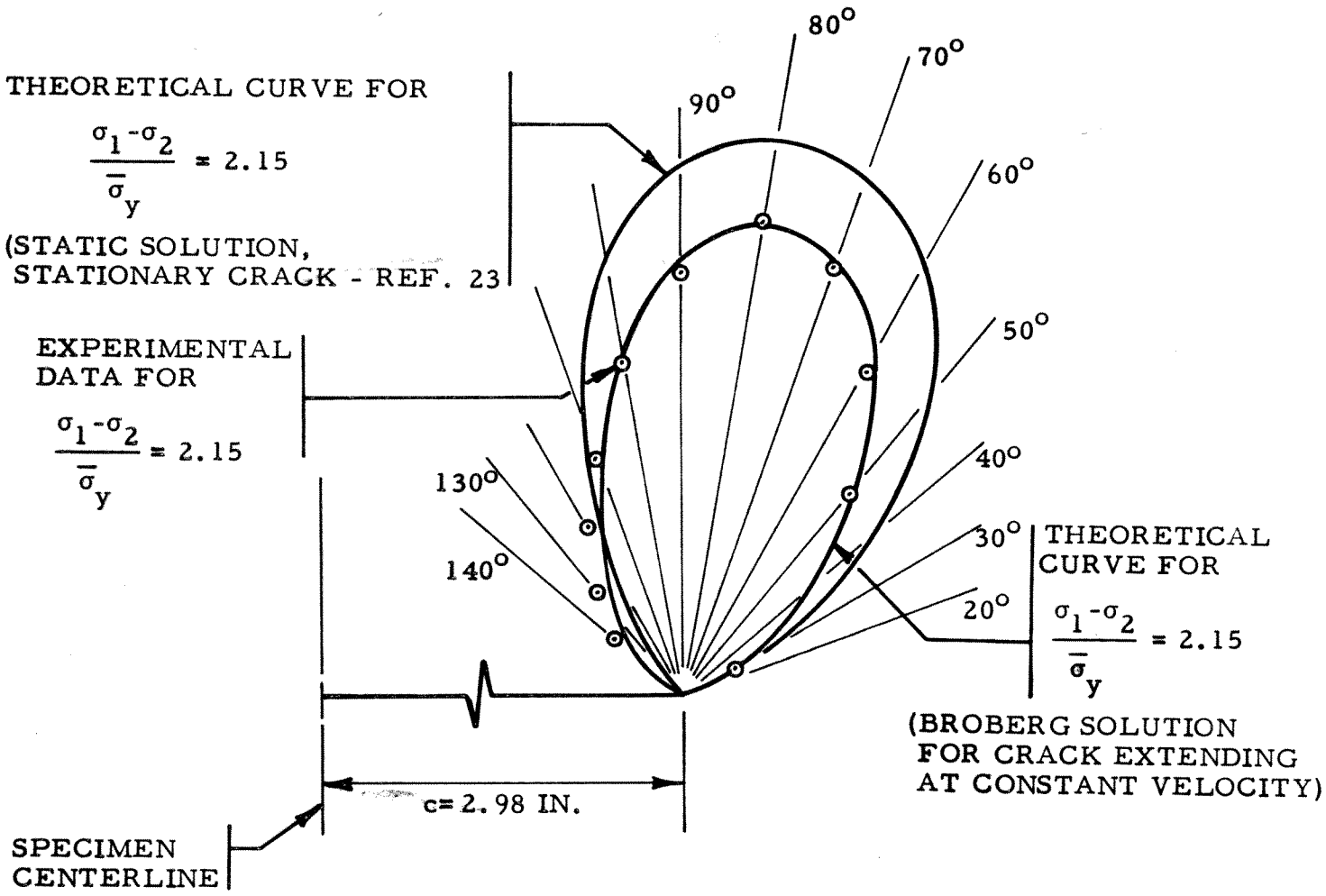

Figure 26b. Comparison of Experimental Patterns from Test 24-1 for Constant Crack Velocity Condition with Theoretical Patterns

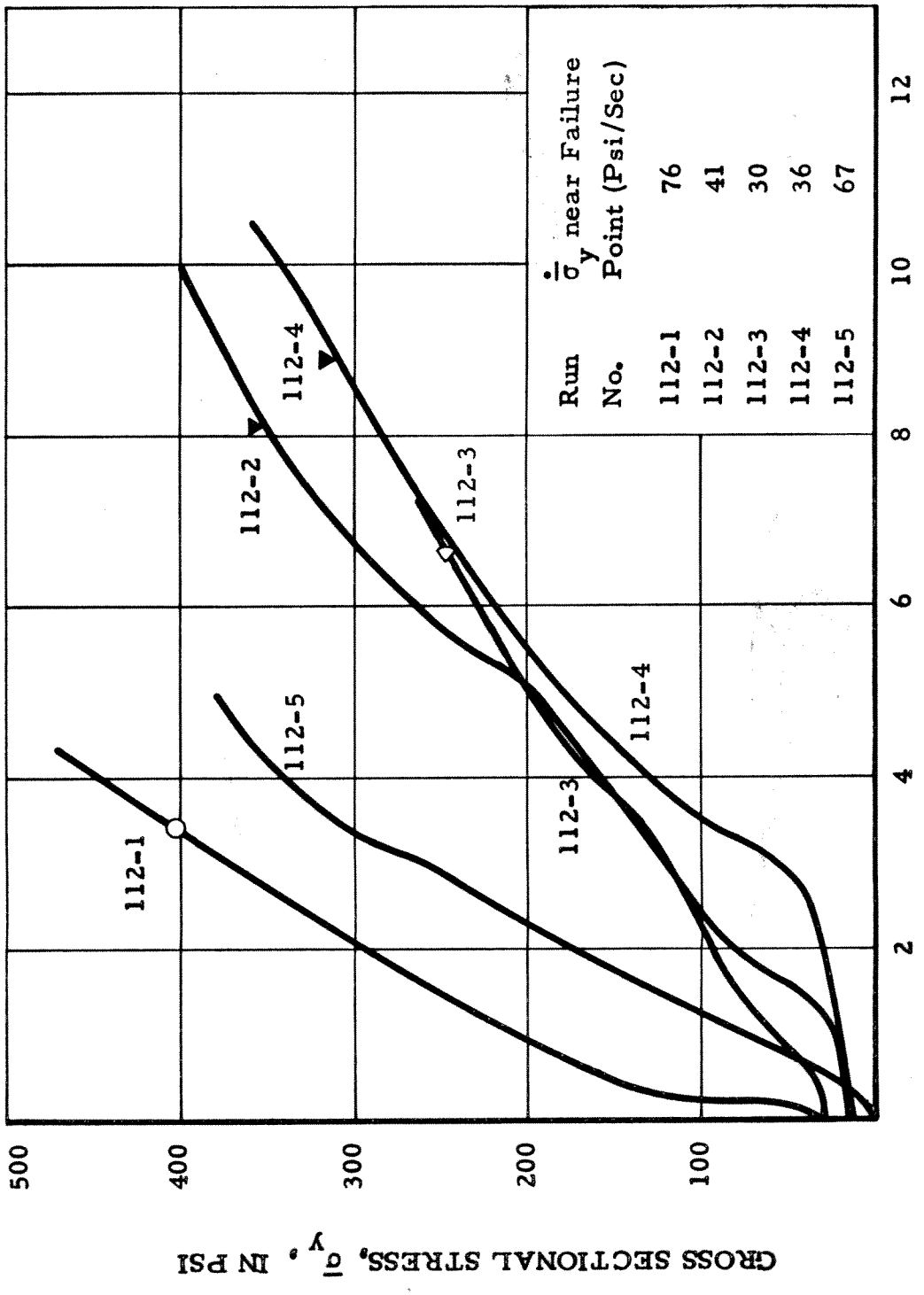

Figure 27 - Applied Loading Curves for Tests at 112°C

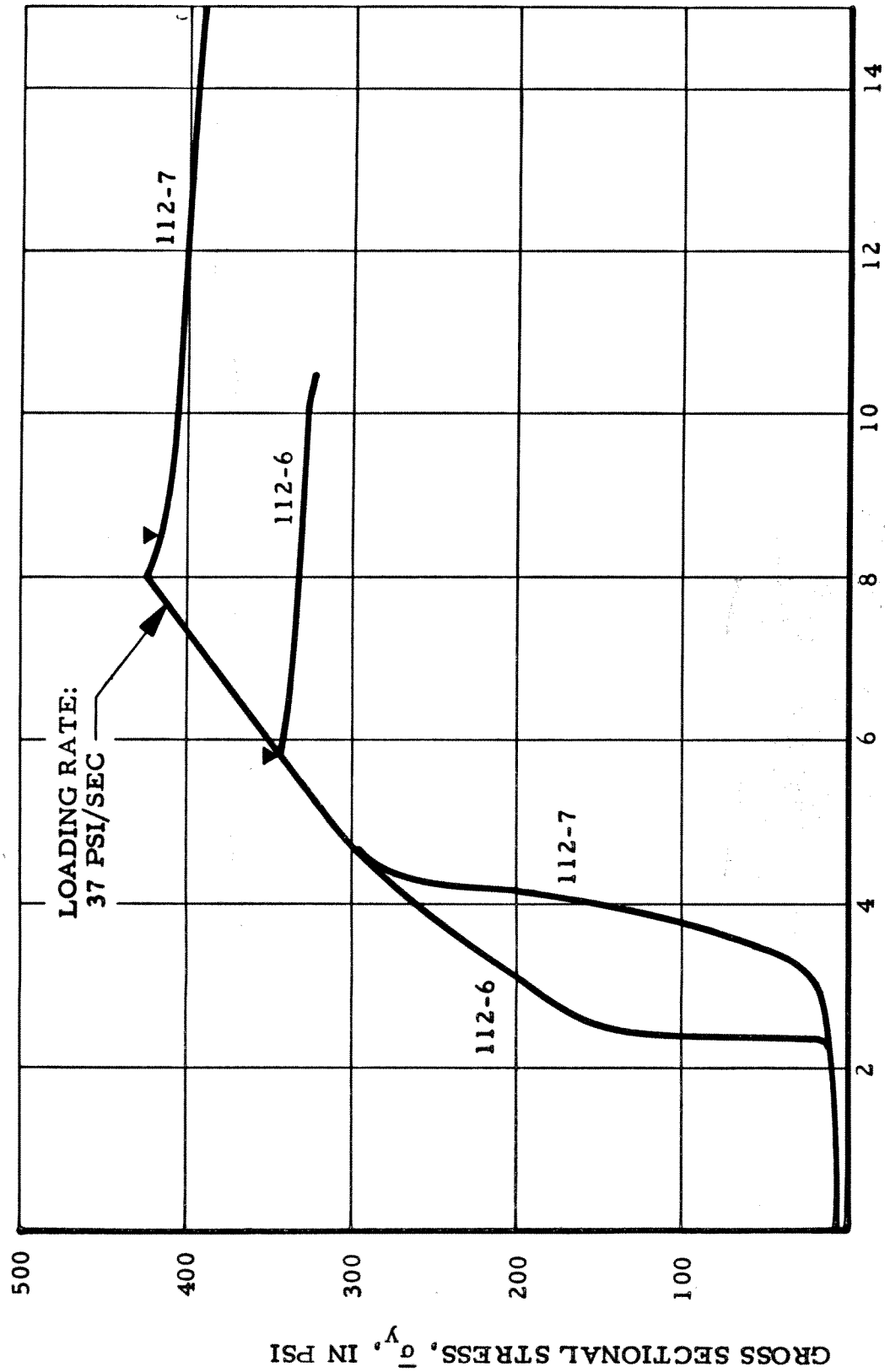

Figure 28. Applied Loading Curves for Tests at 112°C

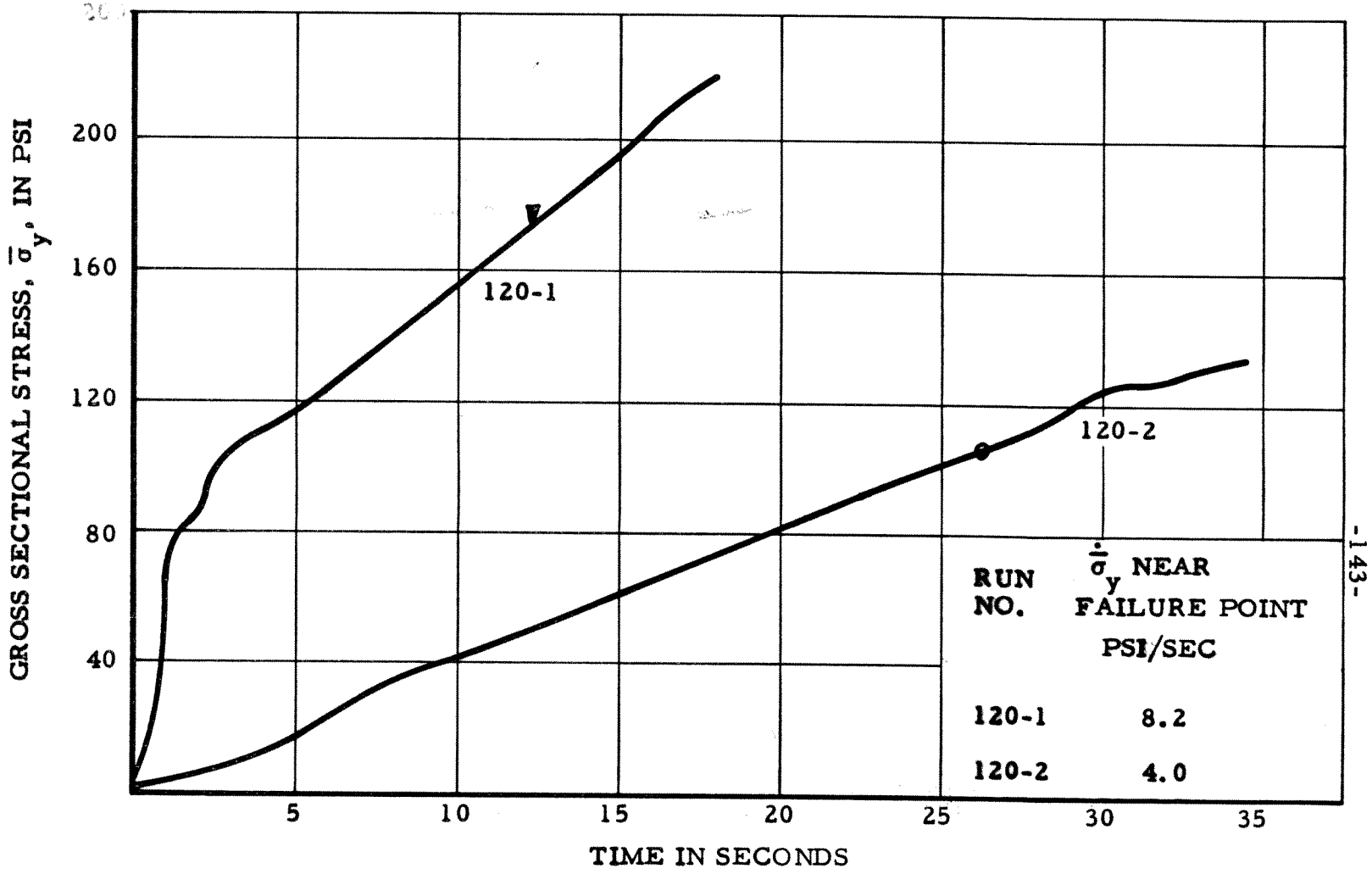

Figure 29. Loading Curves for Specimens at 120°C

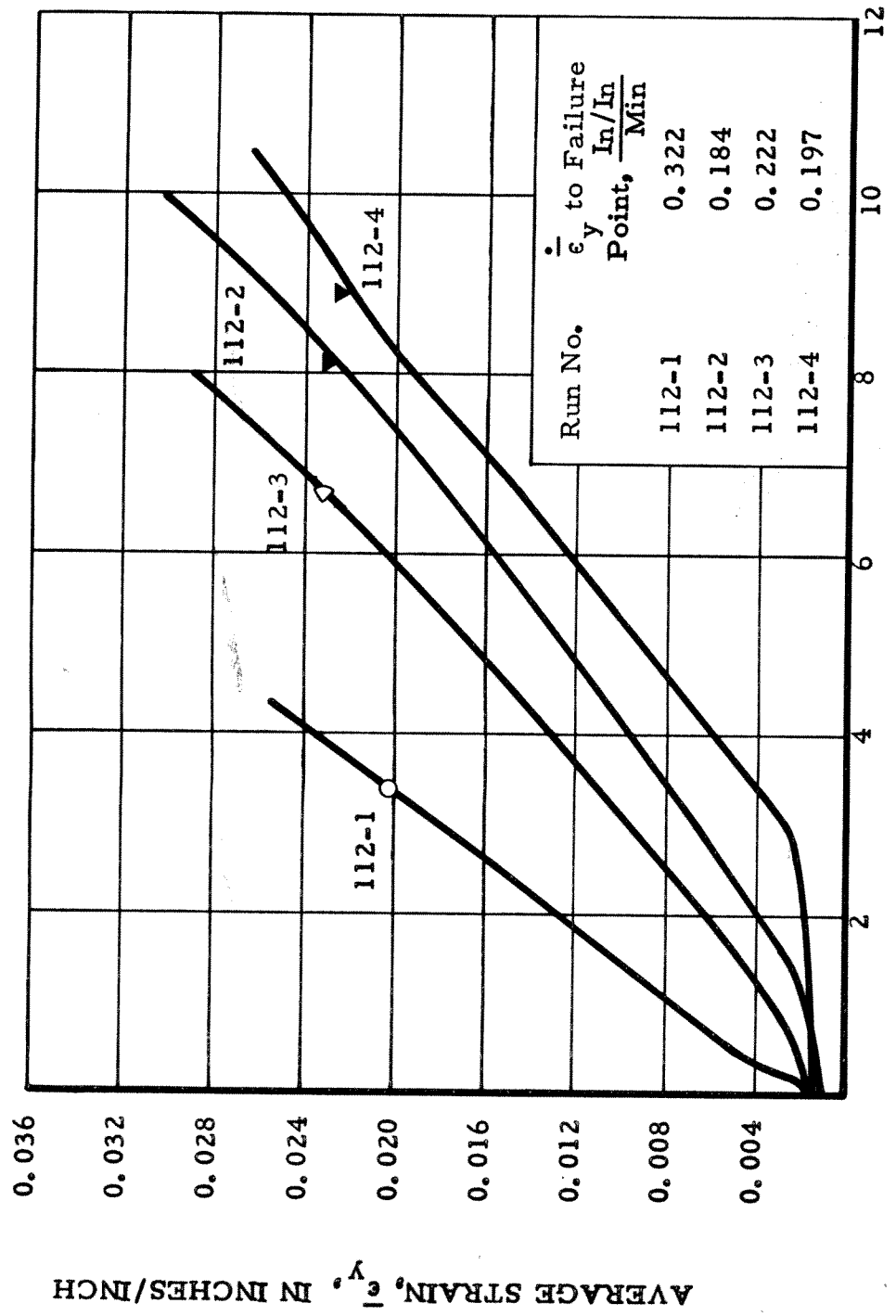

Figure 30 - Average Strain Curves for Tests at 112°C

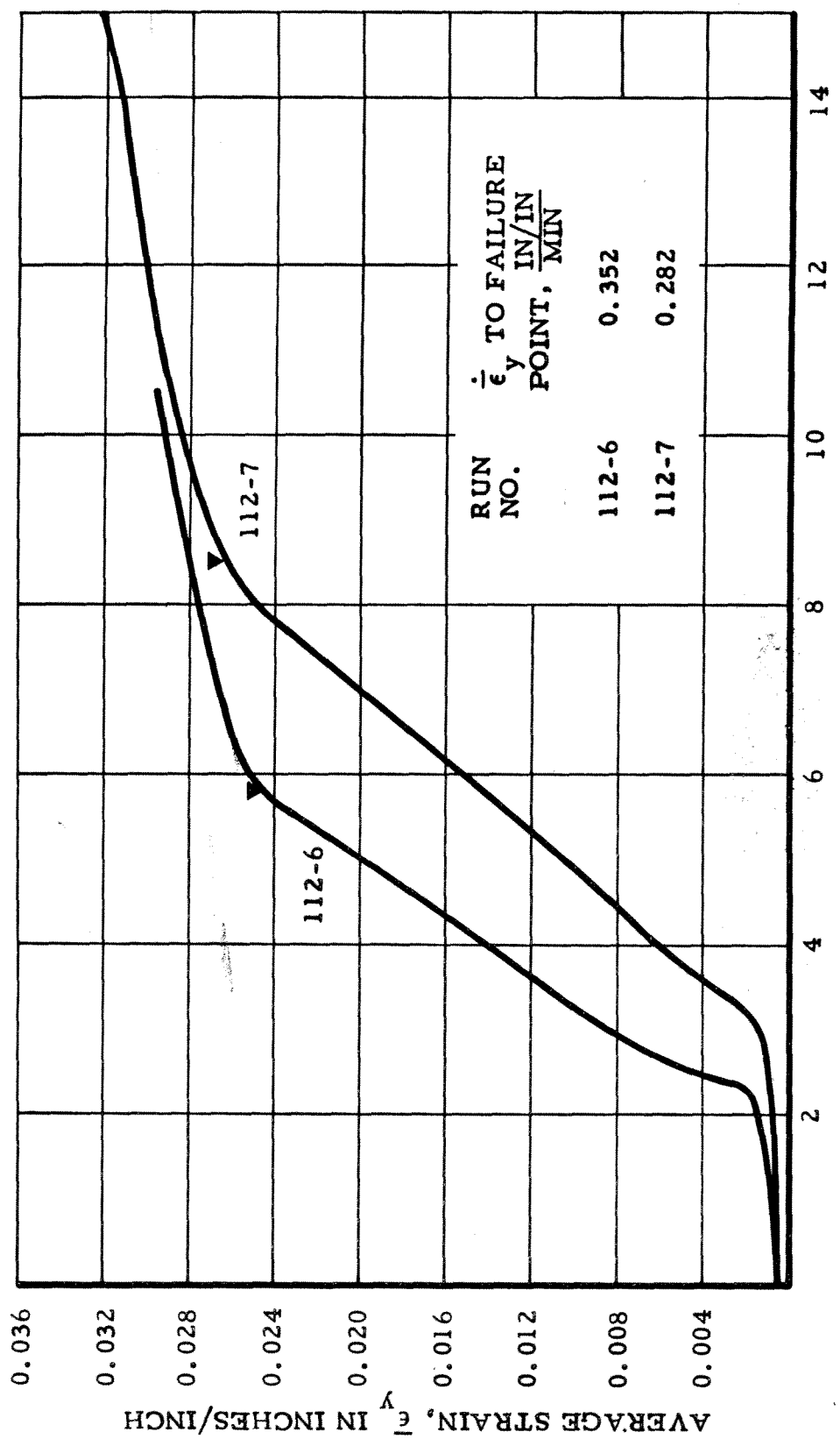

Figure 31. Average Strain Curves for Tests at 112°C

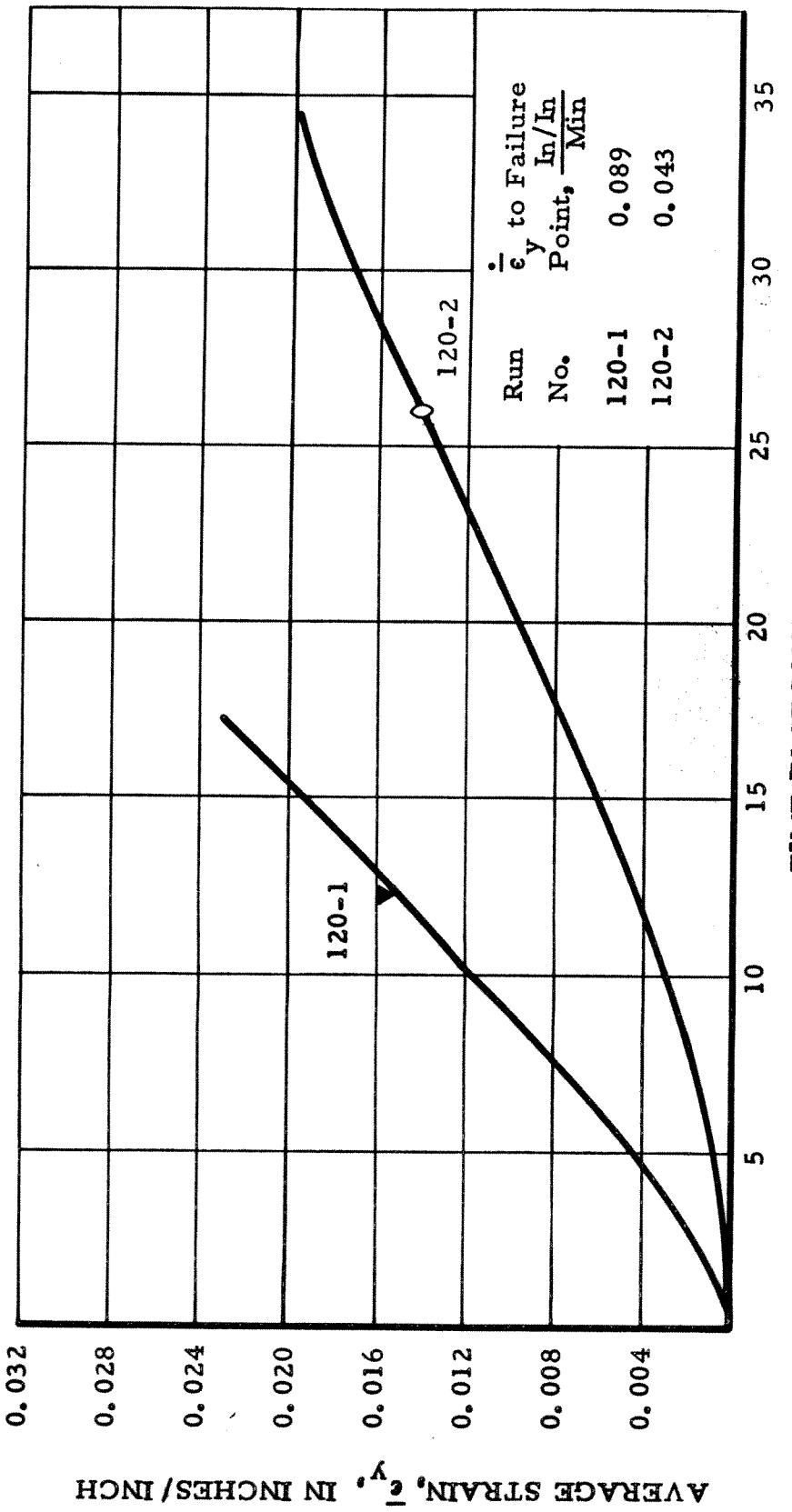

Figure 32 - Average Strain Curves for Tests at 120°C

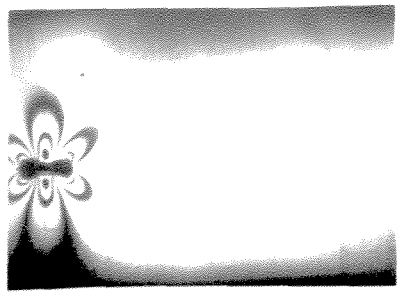

1. t = 0;
   c = 0.300

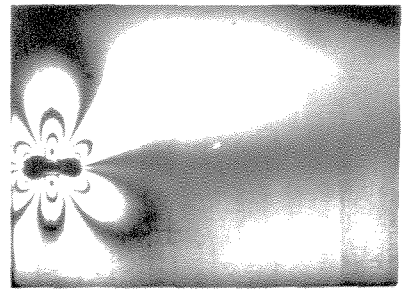

2. t = 0.9738;
   c = 0.350

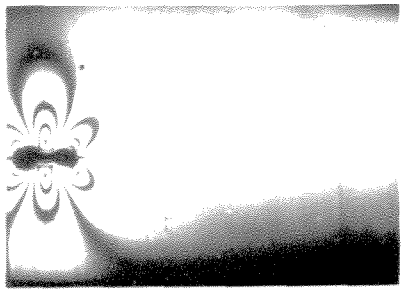

3. t = 1.4184
   c = 0.425

4. t = 1.7393;
   c = 0.490

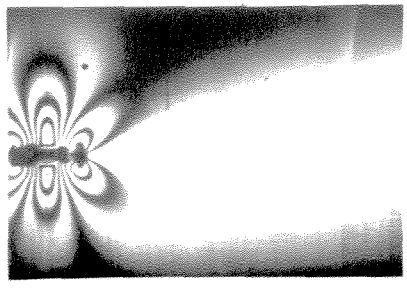

5. t = 1.89826;
   c = 0.600

Figure 33. Crack Propagation Photographs from Run 112-2 (t is time in seconds; c is half crack length in inches. Distance between crosses is 2.00 inches)

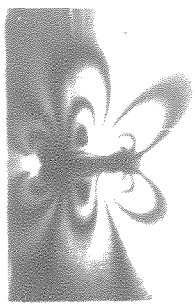

1. t = 0; t' = 1.3264
   c = 0.425

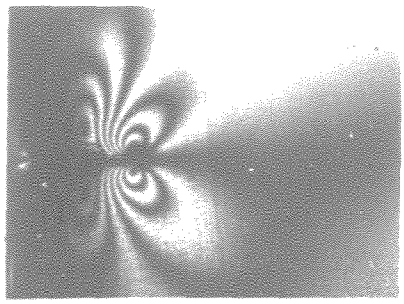

2. t = 0.8920; t' = 0.4344
   c = 0.590

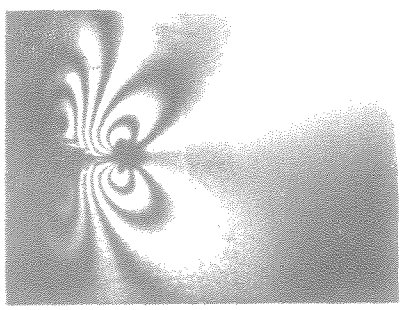

3. t = 1.1110; t' = 0.2154
   c = 0.690

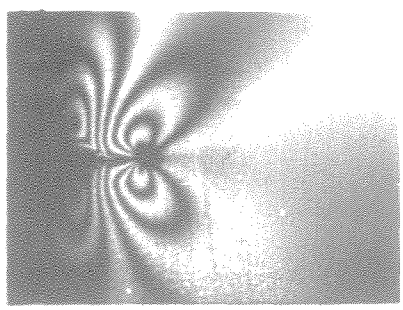

4. t = 1.2120; t' = 0.1144
   c = 0.79

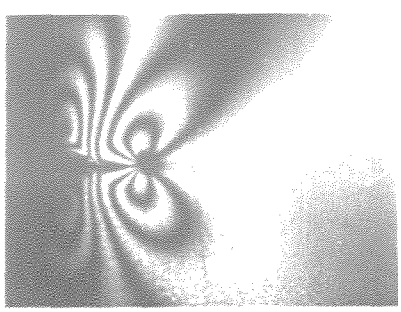

5. t = 1.2840; t' = 0.0424
   c = 0.915

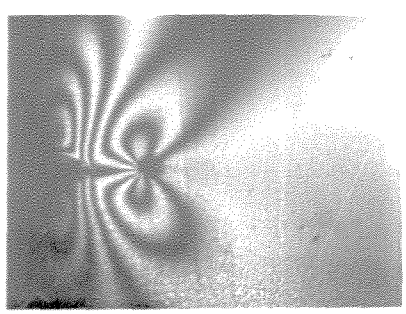

6. t = 1.3120; t' = 0.0144
   c = 0.990

Figure 34a. Crack Propagation Photograph from Run 112-3 (t and t' in seconds; $t' = t_f - t$; t_f = t at frame no. 10; c in inches)

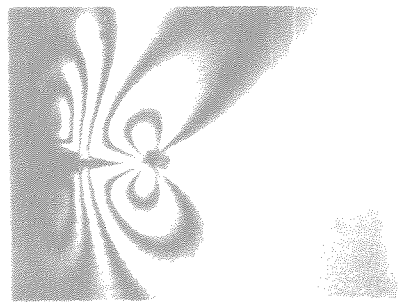

7. t = 1.32582, t' = 0.00057
   c = 1.110

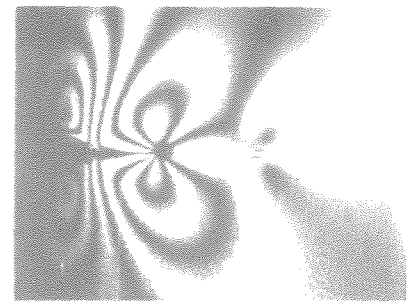

8. t = 1.32601; t' = 0.00038
   c = 2.375

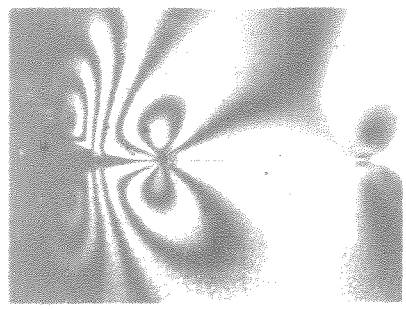

9. t = 1.32620; t' = 0.00019
   c = 3.575

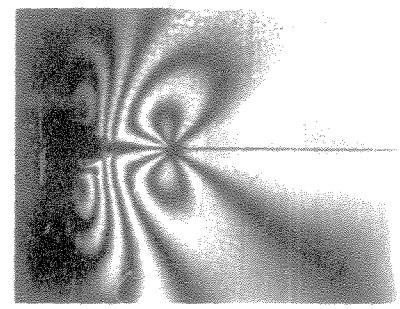

10. t = 1.32639; t' = 0
    c > 4.5

Figure 34b. Crack Propagation Photographs from Run 112-3 (Continued) (t and t' in seconds, c in inches)

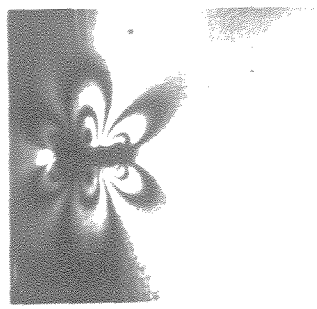

1. t = 0; t' = 1.5978
   c = 0.300

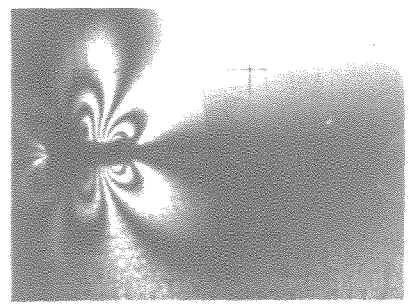

2. t = 0.7870; t' = 0.8108
   c = 0.325

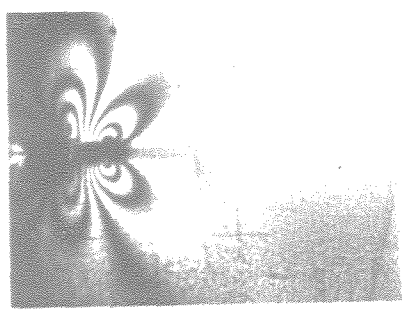

3. t = 1.2620; t' = 0.3358
   c = 0.425

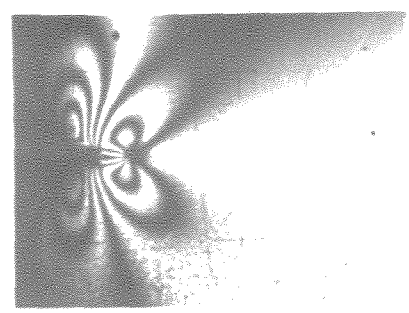

4. t = 1.5790; t' = 0.0188
   c = 0.640

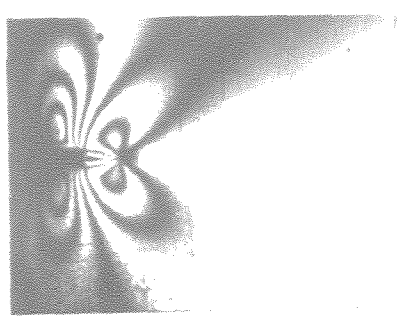

5. t = 1.59724; t' = 0.00055
   c = 0.750

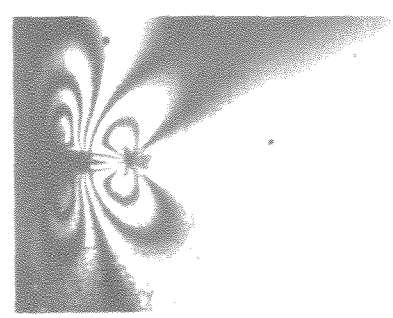

6. t = 1.59735; t' = 0.00044
   c = 0.775

Figure 35a. Crack Propagation Photographs from Run 112-4
(t and t' in seconds; c in inches)

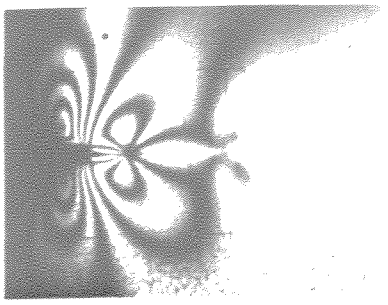

7. t = 1.59746; t' = 0.00033
   c = 2.000

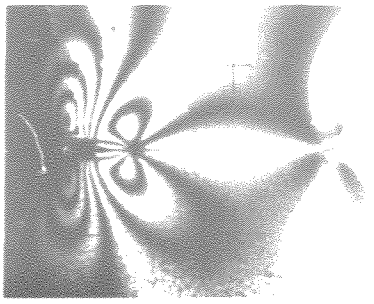

8. t = 1.59757; t' = 0.00022
   c = 3.125

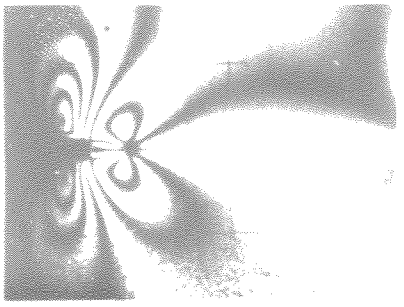

9. t = 1.59768; t' = 0.00011
   c = 4.25

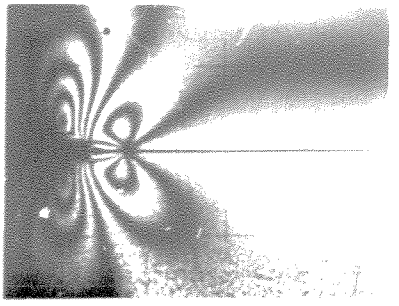

10. t = 1.59779; t' = 0
    c > 5.0

Figure 35b. Crack Propagation Photographs from Run 112-4 (Continued)(t and t' in seconds; c in inches)

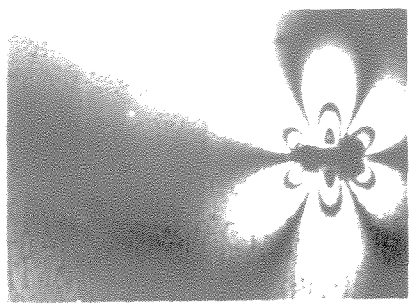

1. t = 0; t' = 4.7538
   c = 0.300

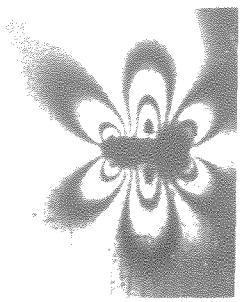

2. t = 1.0120; t' = 3.7418
   c = 0.360

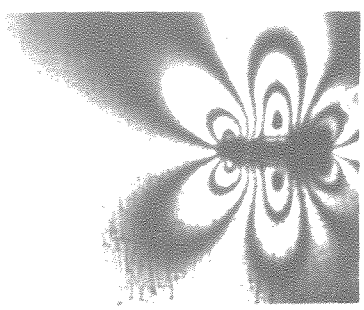

3. t = 2.7310; t' = 2.0228
   c = 0.550

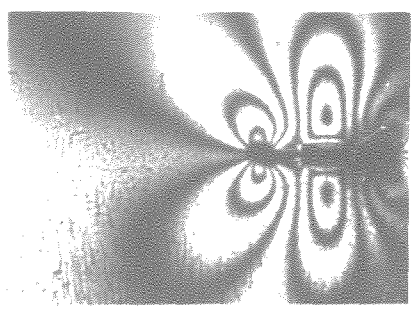

4. t = 3.7250; t' = 1.0288
   c = 0.815

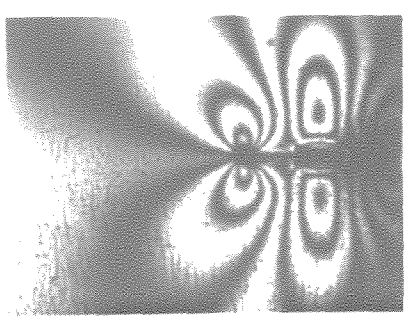

5. t = 3.9734; t' = 0.7804
   c = 0.925

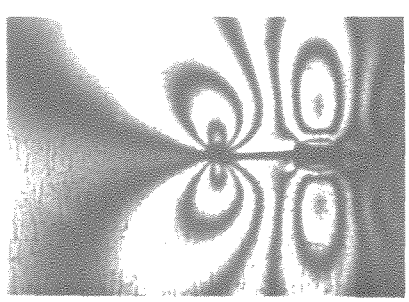

6. t = 4.4081; t' = 0.3457
   c = 1.215

Figure 36a. Crack Propagation Photographs from Run 112-6 (t and t' in seconds; c in inches)

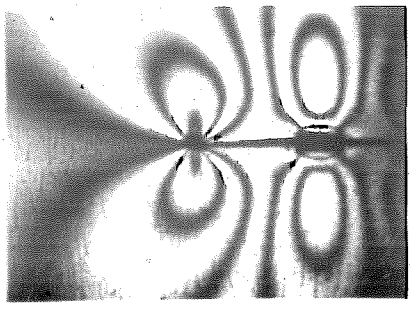

7. t = 4.6068; t' = 0.1470
   c = 1.500

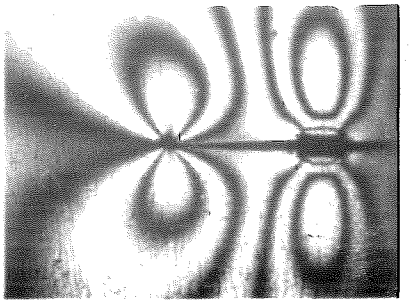

8. t = 4.7184; t' = 0.0354
   c = 1.870

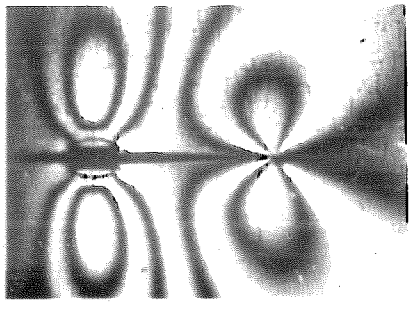

9. t = 4.7535; t' = 0.00031
   c = 2.160

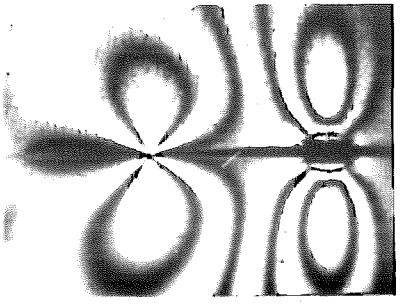

10. t = 4.7538; t' = 0
    c > 4

Figure 36b. Crack Propagation Photographs from Run 112-6 (Continued) (t and t' in seconds; c in inches)

1. t = -10.710
   c = 0.300

2. t = -9.270
   c = 0.300

3. t = -8.550
   c = 0.300

4. t = -7.830
   c = 0.300

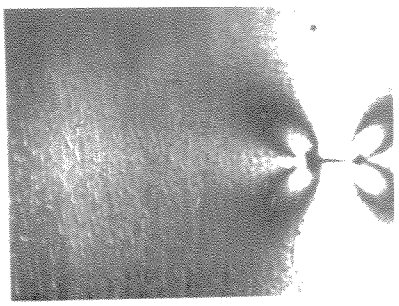

5. t = -7.330
   c = 0.300

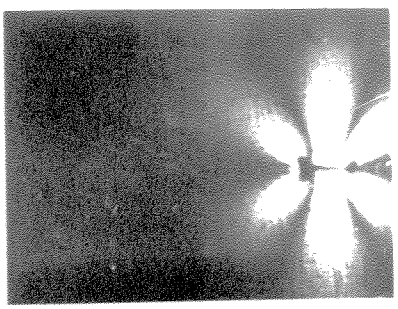

6. t = -0.720
   c = 0.300

Figure 37a. Crack Propagation Photographs from Run 120-1 (During Loading Prior to Initiation of Crack Propagation; t is time interval to initiation in seconds)

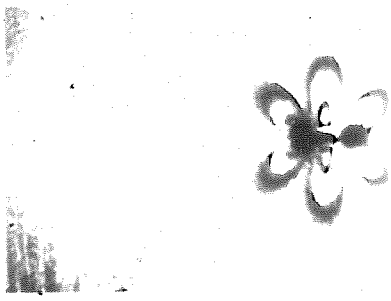

7. t = 0; t' = 4.830
c = 0.300

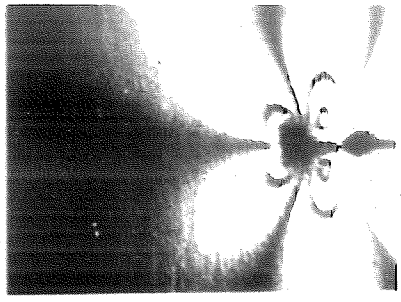

8. t = 2.172; t' = 2.658
c = 0.425

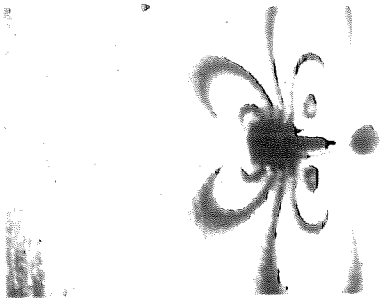

9. t = 3.552; t' = 1.278
c = 0.650

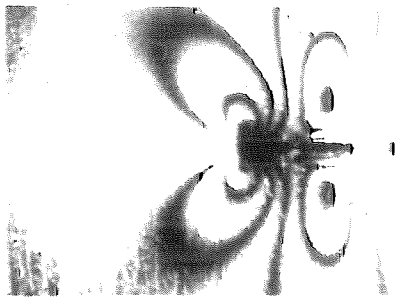

10. t = 4.202; t' = 0.628
c = 0.975

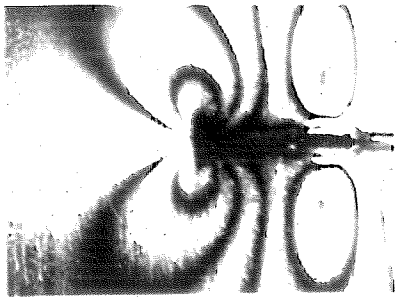

11. t = 4.562; t' = 0.268
c = 1.390

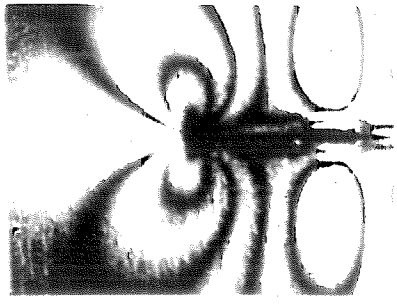

12. t = 4.670; t' = 0.160
c = 1.635

Figure 37b. Crack Propagation Photographs from Run 120-1 (Continued) (t and t' in seconds, c in inches)

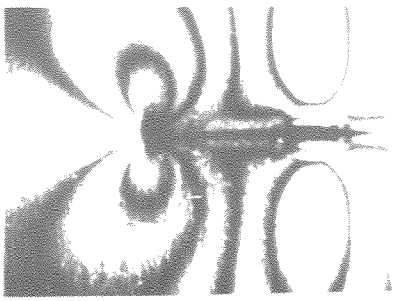

13. t = 4.742; t' = 0.088
c = 1.95

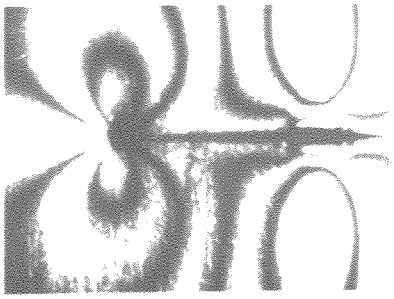

14. t = 4.805; t' = 0.025
c = 2.40

15. t = 4.828; t' = 0.002
c = 2.76

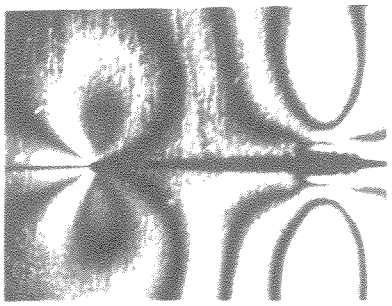

16. t = 4.830; t' = 0
c > 5

Figure 37c. Crack Propagation Photographs from Run 120-1 (Continued) (t and t' in seconds, c in inches)

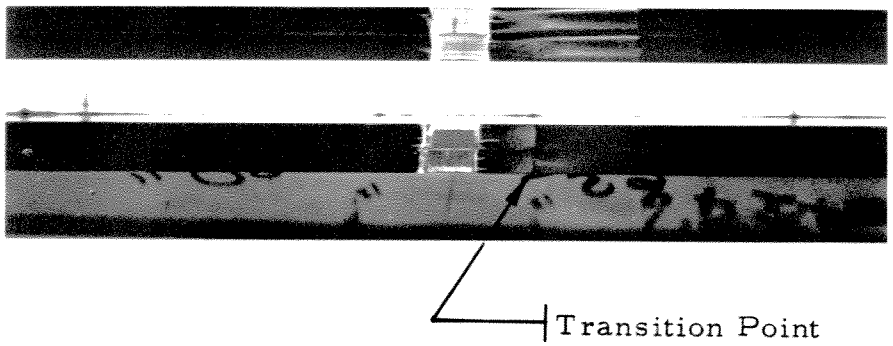

	Run Number	Strain Rate (in/in/min.)	Half Crack Length at Transition Point (inches)
Top Specimen	112-7	Const. load	1.75
Bottom Specimen	112-1	0.322	0.60
Other Specimens Not Shown	112-2	0.184	0.60
	112-3	0.222	1.10
	112-4	0.197	0.78
	112-6	Const. load	2.16
	120-1	0.089	2.81

Figure 38. Photographs of Fracture Surface from High Temperature Low Loading Rate Tests

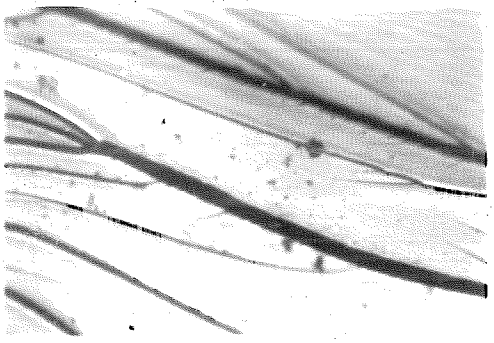

1. x = 0.30 inches
   Centerline Notch Vertex

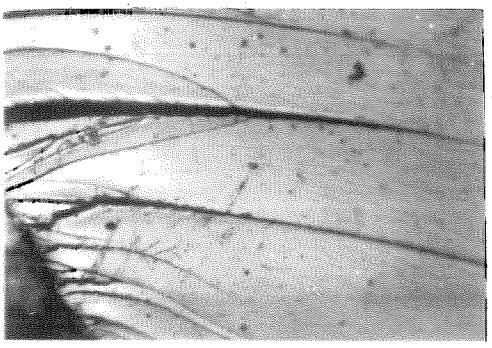

2. x = 0.30 inches
   Edge Notch Vertex

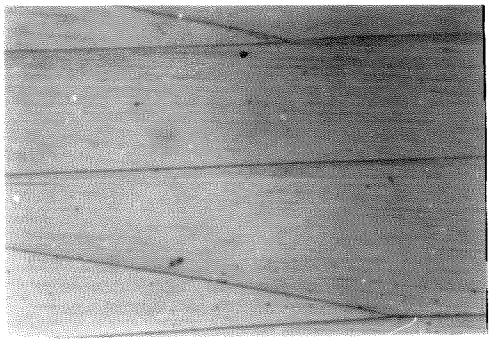

3. x = 0.75
   Centerline

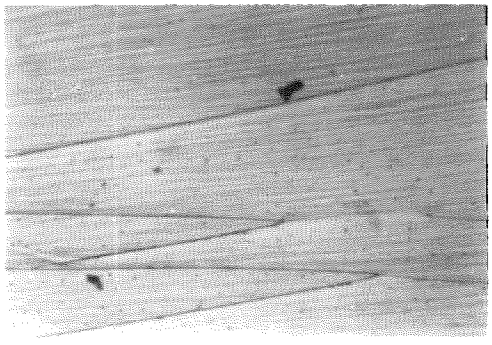

4. x = 0.75
   Edge

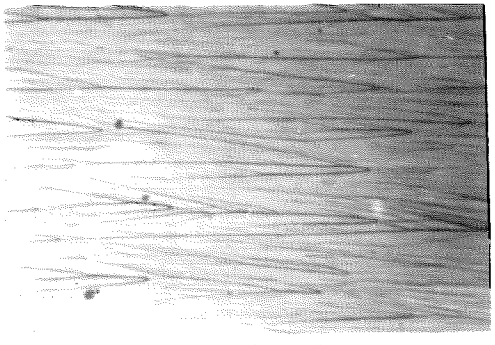

5. x = 1.30
   Centerline

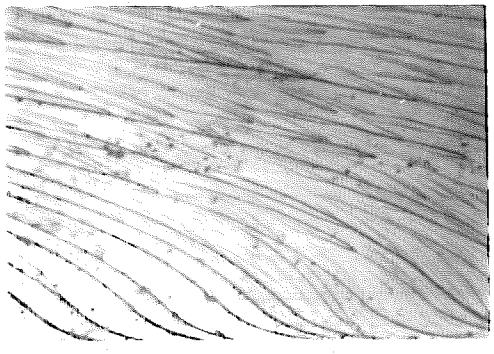

6. x = 1.30
   Edge

Figure 39a. Photomicrographs of Fracture Surface at Various Stations along the Crack Path for Specimen 112-7 Magnification 100x (See sketch in Figure 20a)

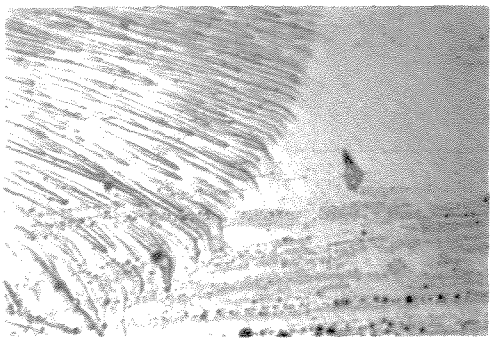

7. x = 1.70
Edge

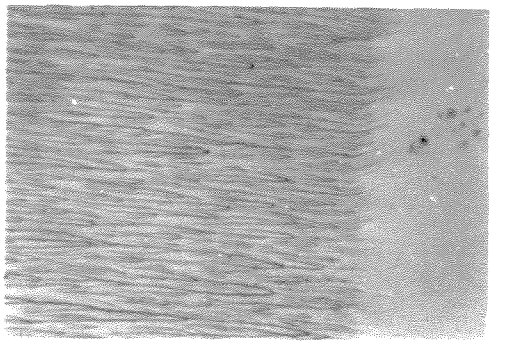

8. x = 1.70
Centerline

9. x = 2.05
Centerline

Figure 39b. Photomicrographs of Fracture Surface at Various Stations along the Crack Path for Specimen 112-7 Magnification 100x

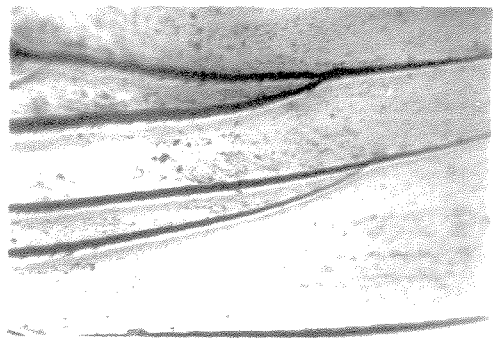

1. x = 0.30; 100x
   Centerline - Notch Vertex

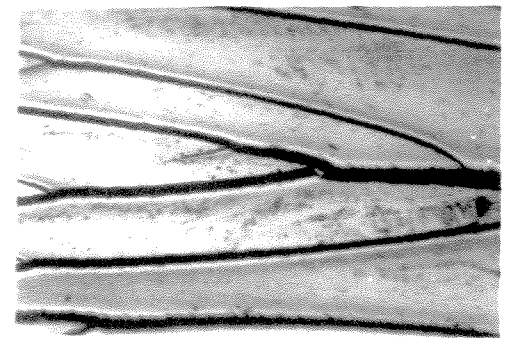

2. x = 0.30; 100x
   Edge - Notch Vertex

3. x = 0.30; 50x
   Centerline

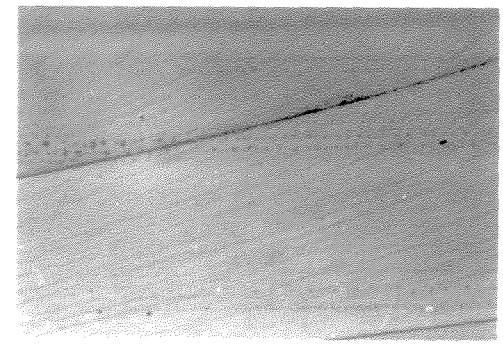

4. x = 1.30; 100x
   Edge

5. x = 2.05; 100x
   Centerline

6. x = 2.05; 200x
   Centerline

Figure 40a. Photomicrographs of Fracture Surface at Various Stations along the Crack Path for Specimen 120-1

7. x = 2.05; 100x
   Edge

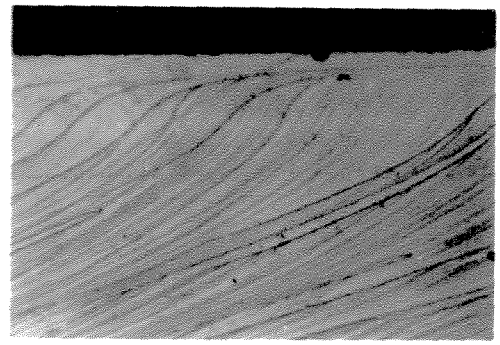

8. x = 2.30; 100x
   Edge

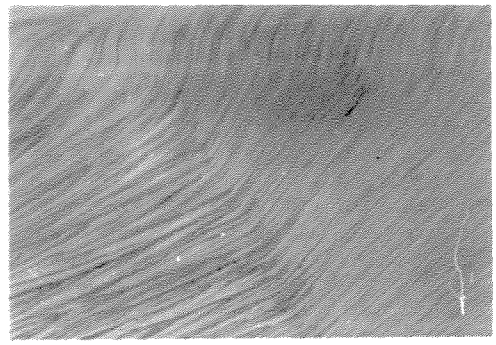

9. x = 2.50; 100x
   Edge

Figure 40b. Photomicrographs of Fracture Surface at Various Stations along the Crack Path for Specimen 120-1

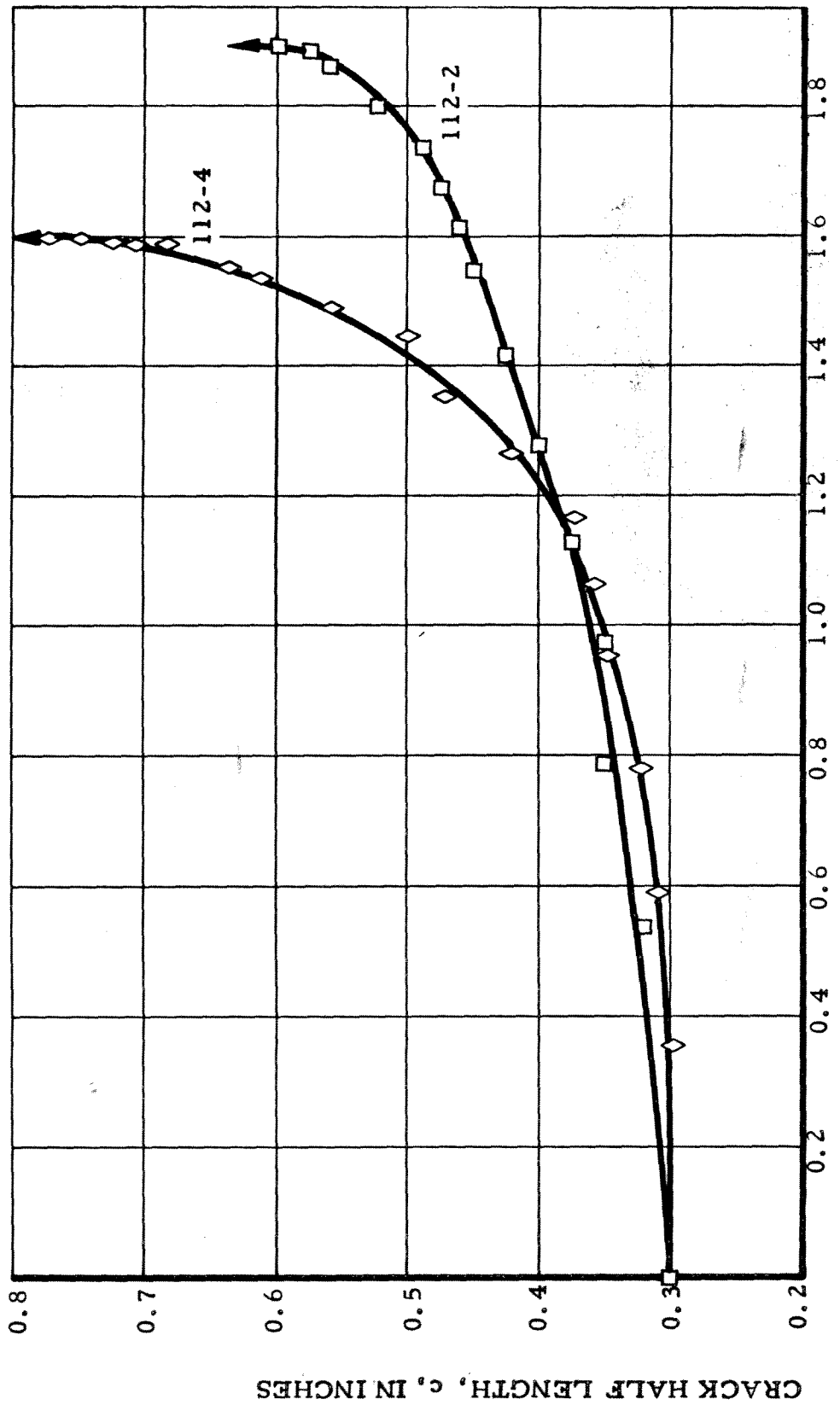

Figure 41. Crack Length Versus Time for Tests 112-2 and 112-4.

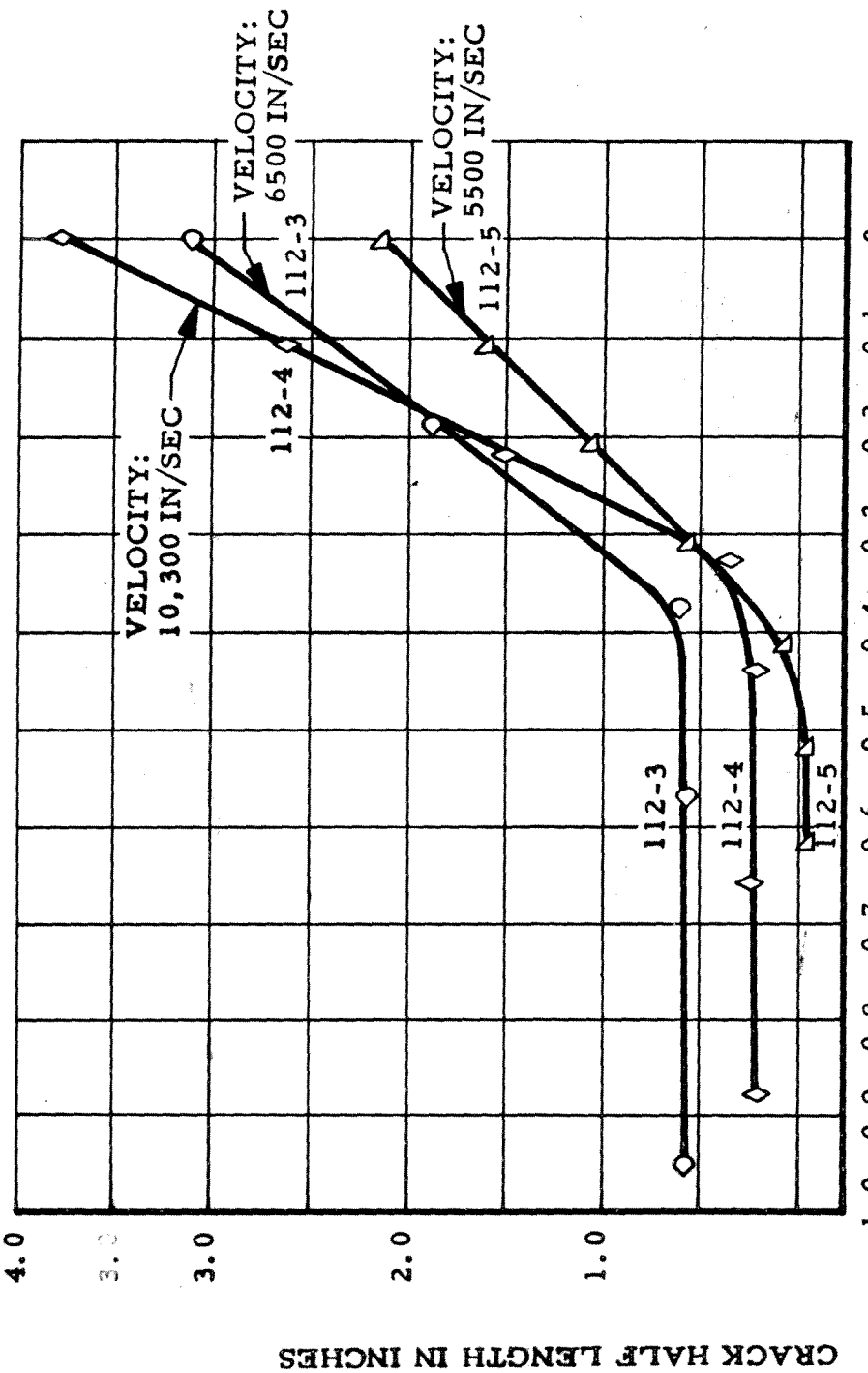

Figure 42. High Acceleration Region of Crack Propagation Curve for Specimen 112-3, 112-4 and 112-5.

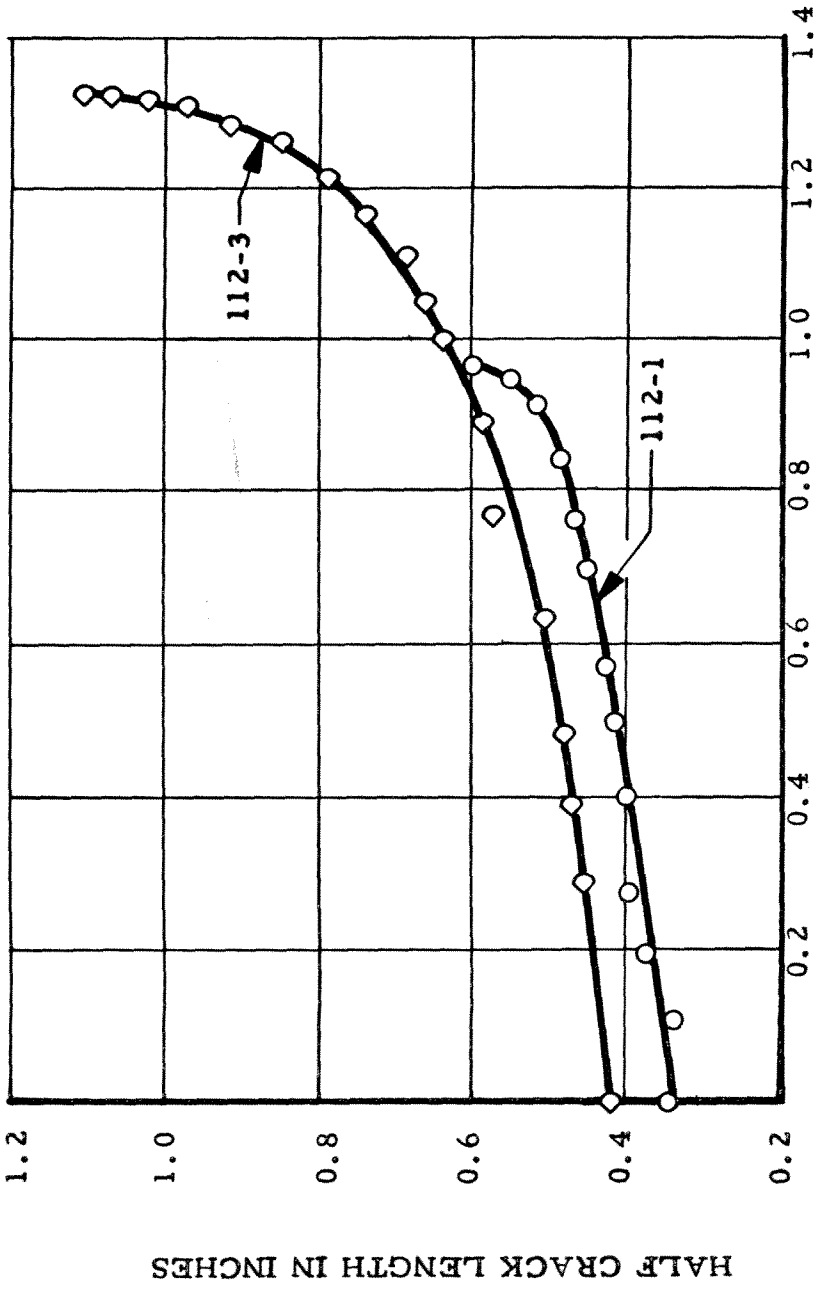

Figure 43. Crack Length Versus Time for Tests 112-1 and 112-3

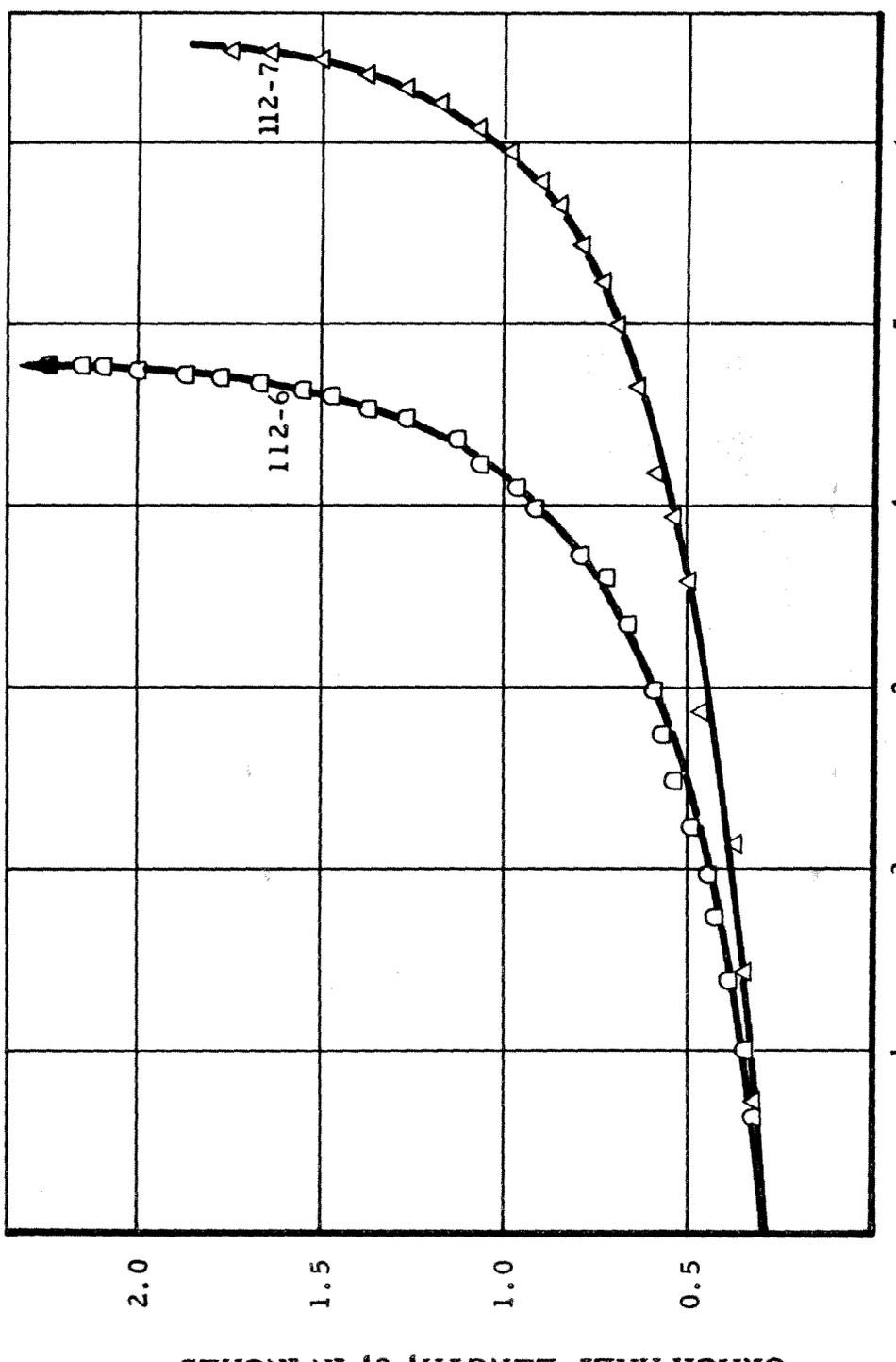

Figure 44. Crack Length as a Function of Time for Tests at 112°C

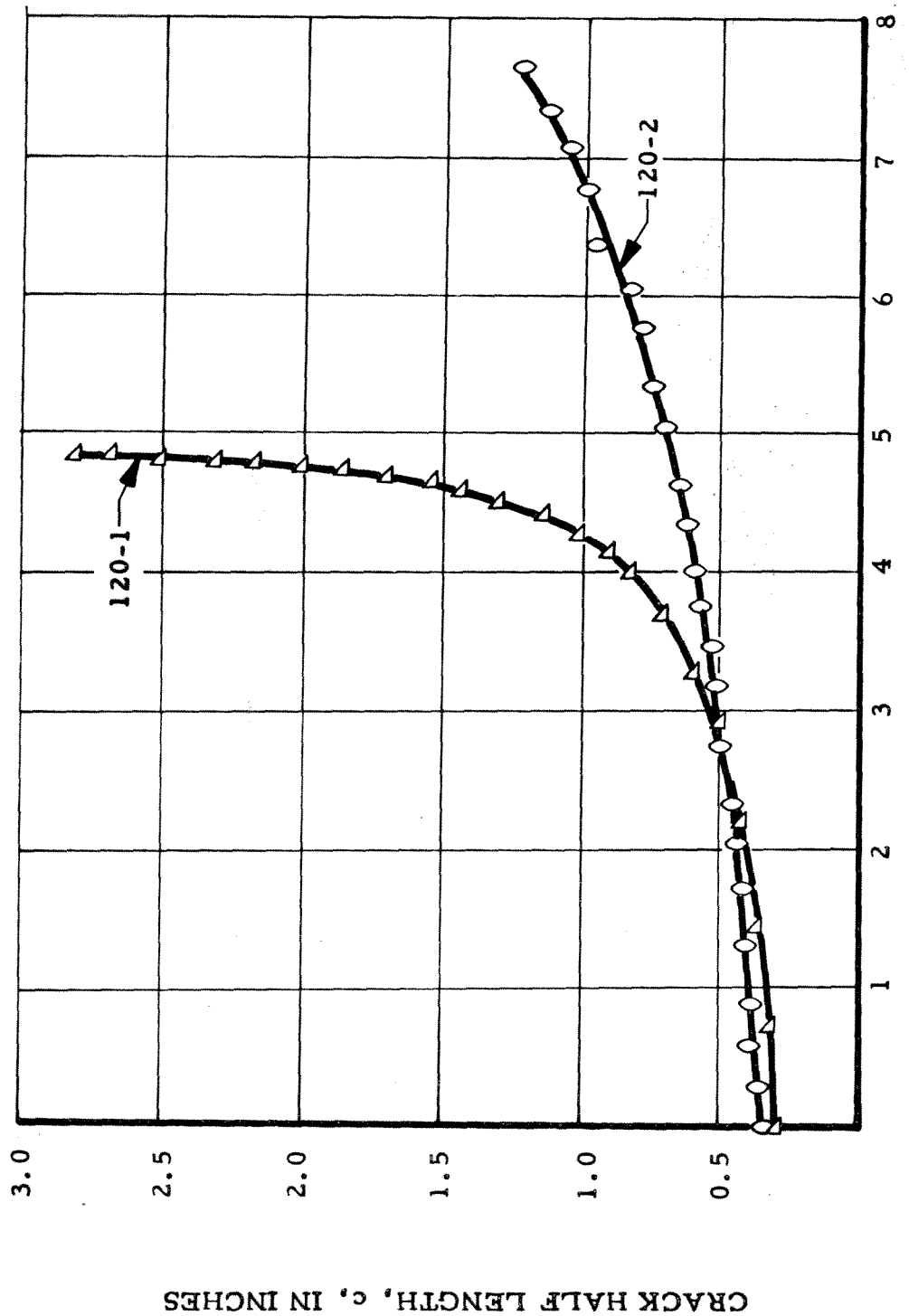

Figure 45. Crack Length Versus Propagation Time for Tests 120-1 and 120-2

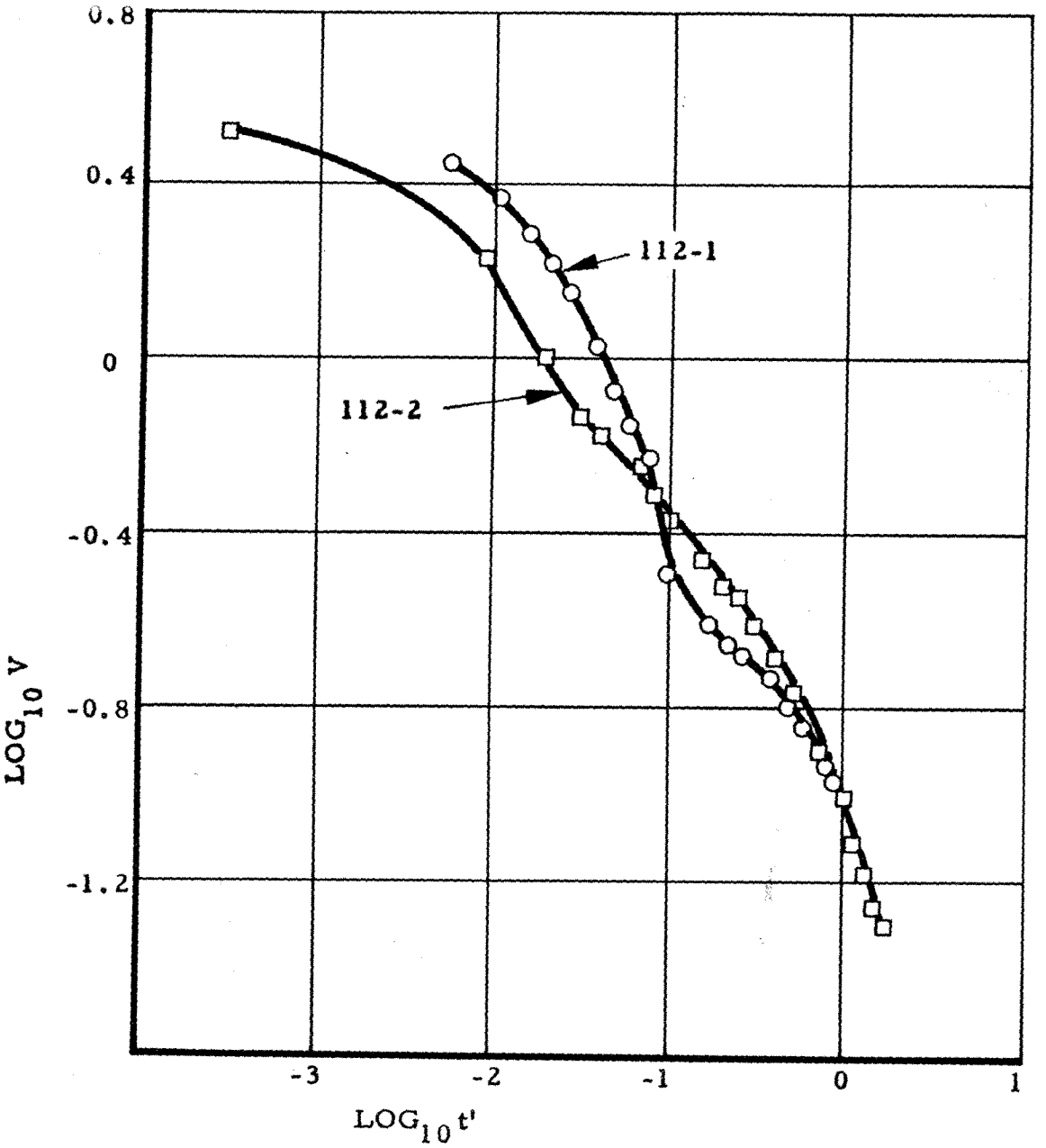

Figure 46. Crack Velocity Curves for Tests 112-1 and 112-2 (v = Crack Velocity; $t' = t_f - t$; t = Time from Start of Crack Run; t_f = Time of Last Data Point for the Run; All Times in Seconds)

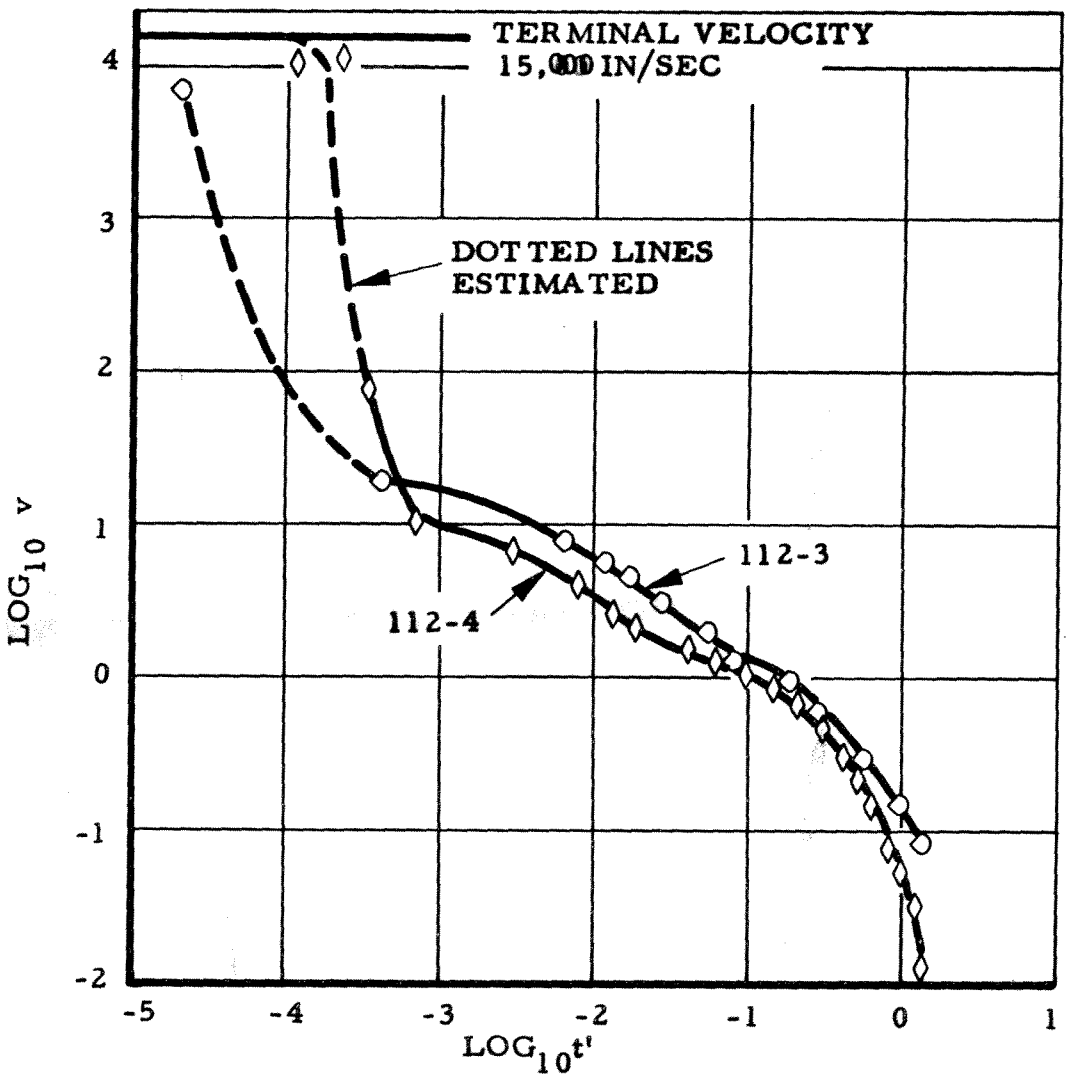

Figure 47. Crack Velocity Curves for Tests 112-3 and 112-4

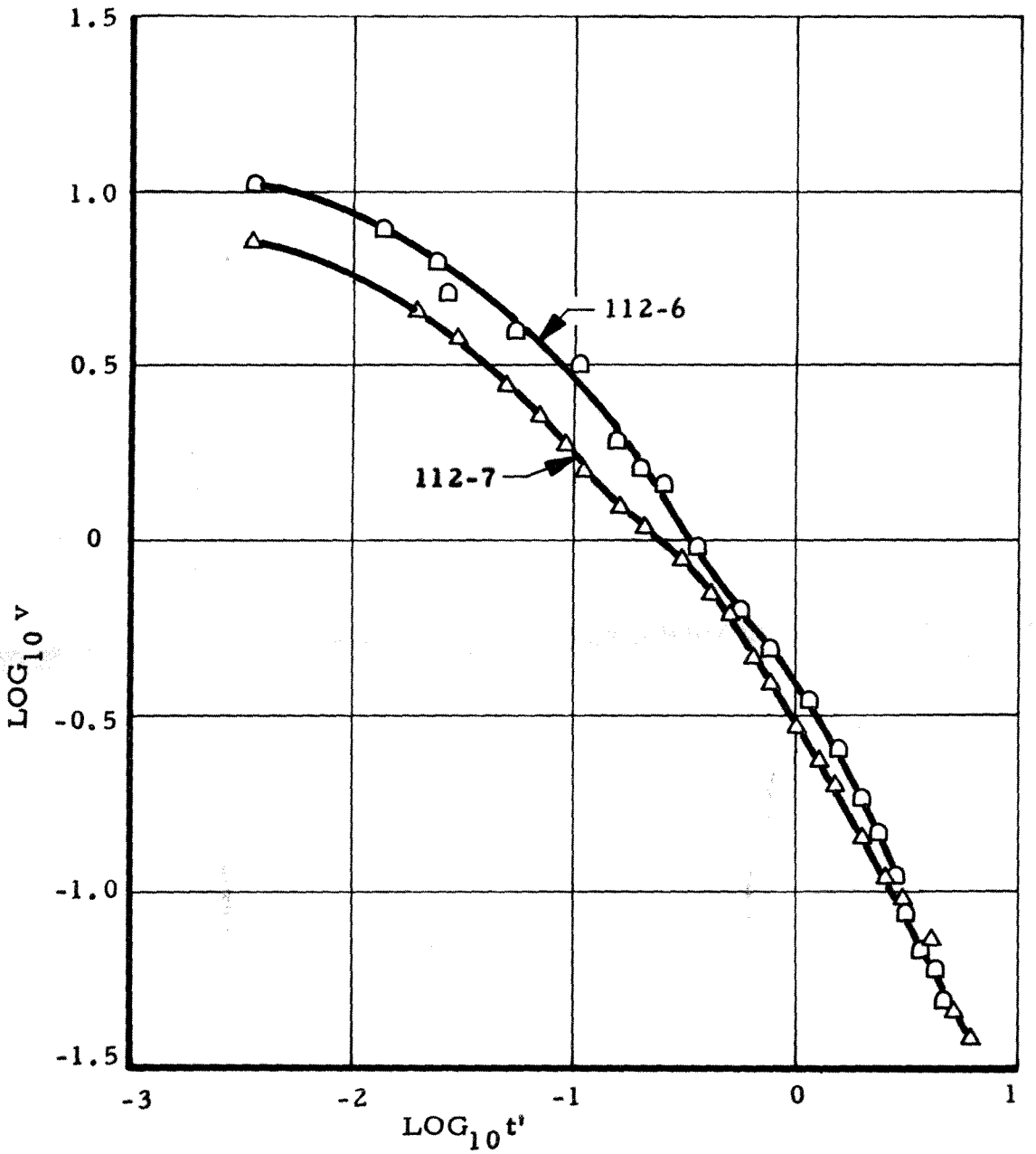

Figure 48. Crack Velocity Curves for Tests 112-6 and 112-7

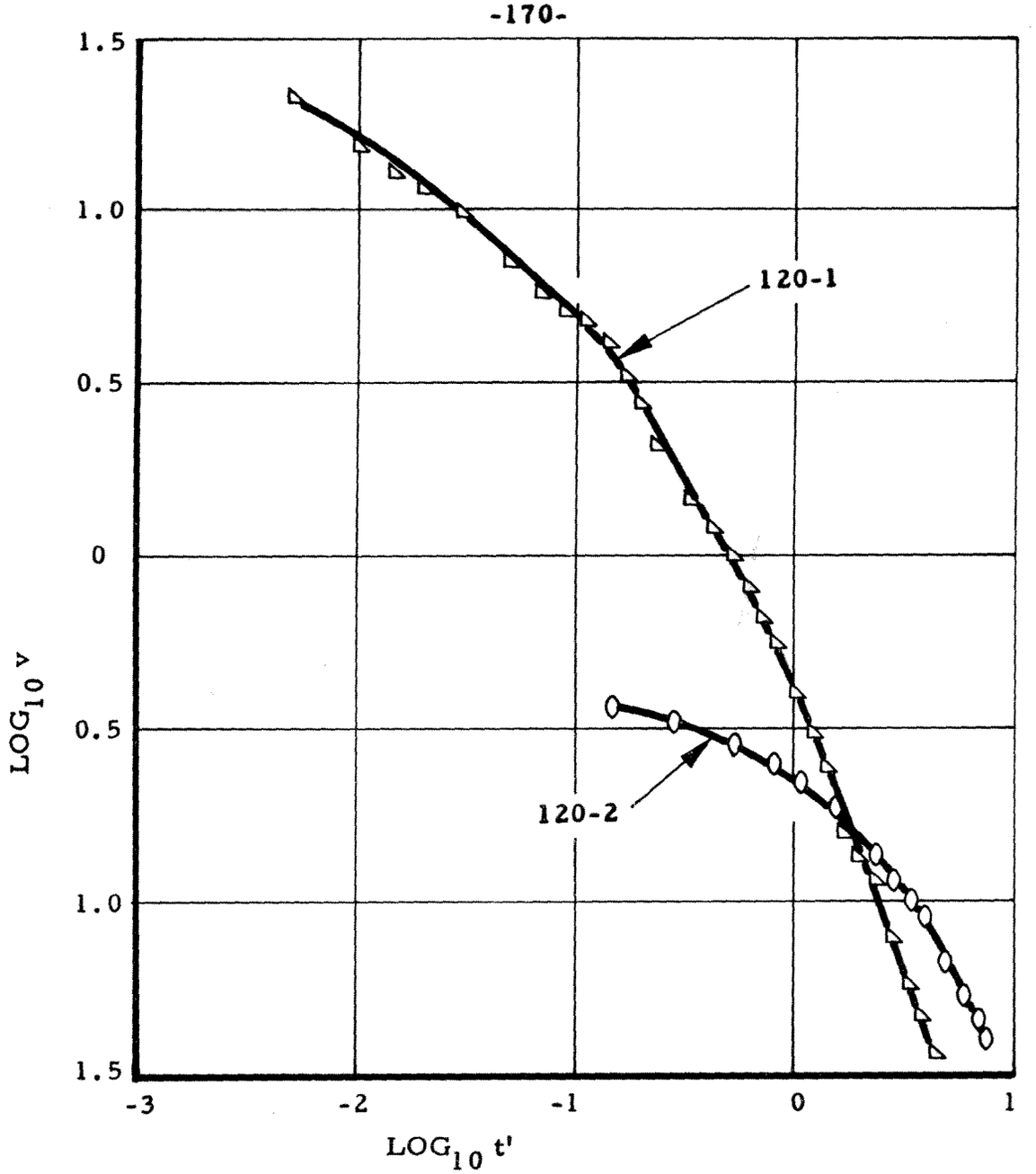

Figure 49. Crack Velocity Curves for Tests 120-1 and 120-2

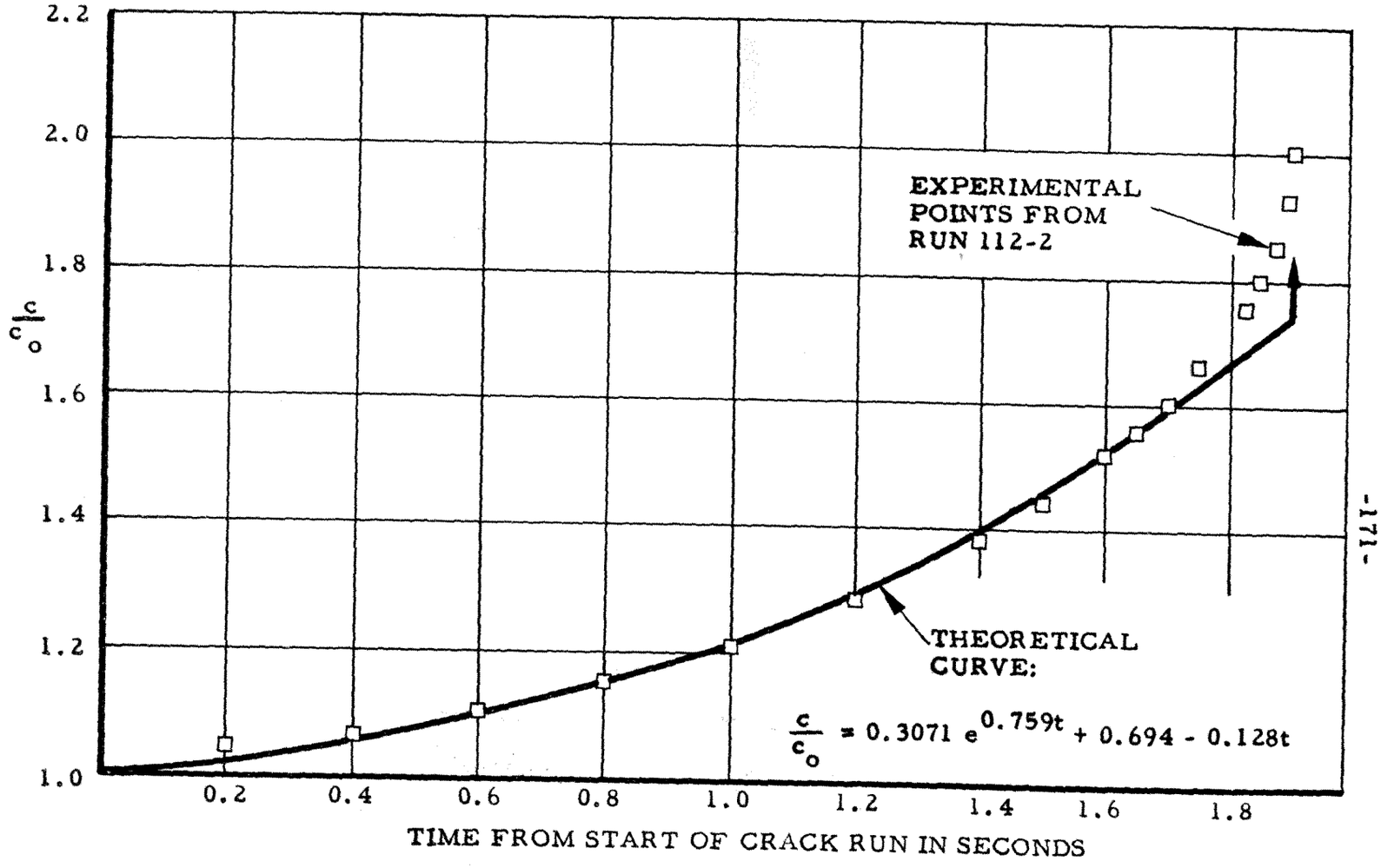

Figure 50. Comparison of Experimental Data in Run 112-2 with Schapery and Williams Theory for Slow Crack Propagation in Viscoelastic Material.

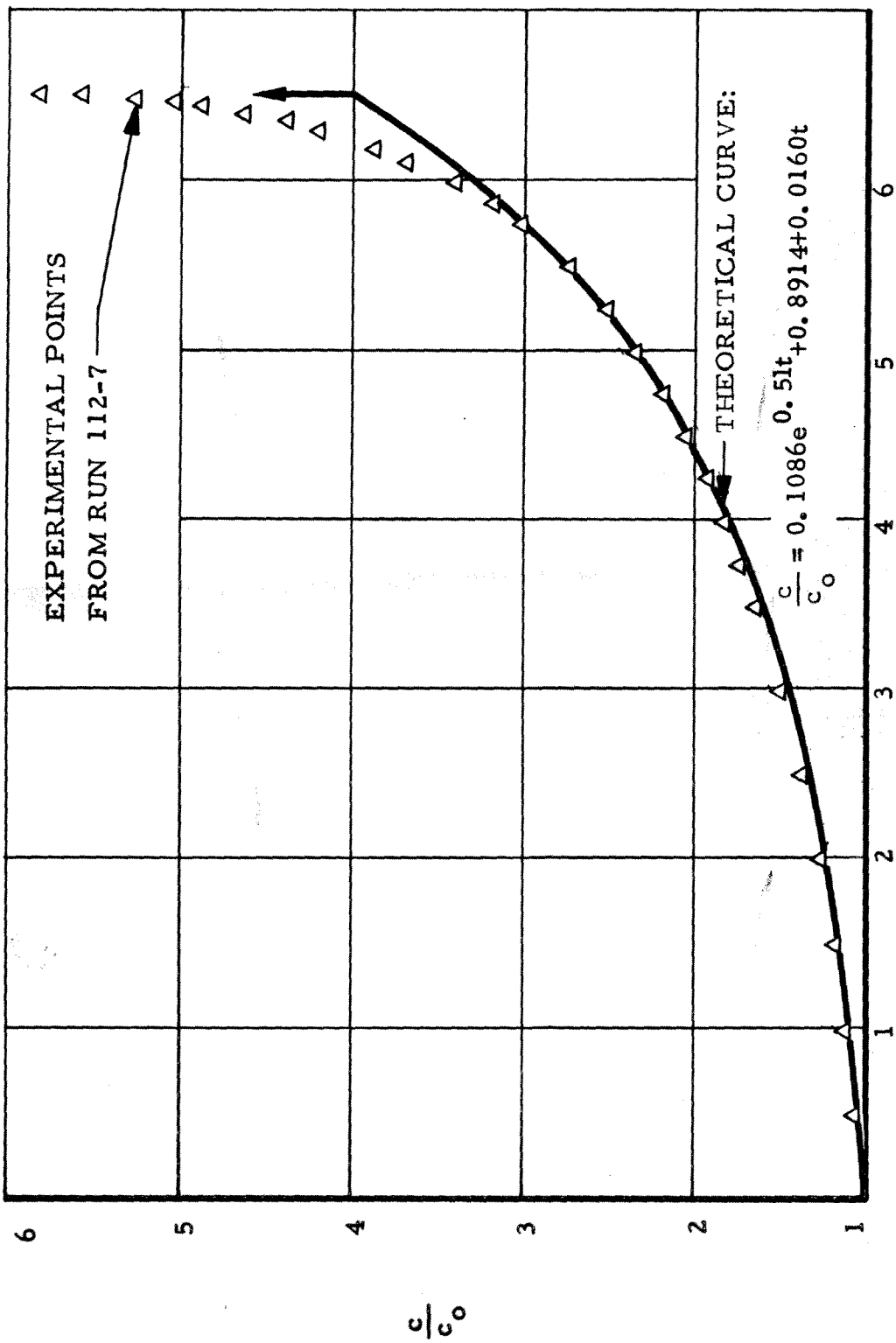

Figure 51 - Comparison of Experimental Data in Run 112-7 with Schapery and Williams Theory for Slow Crack Propagation in Viscoelastic Material

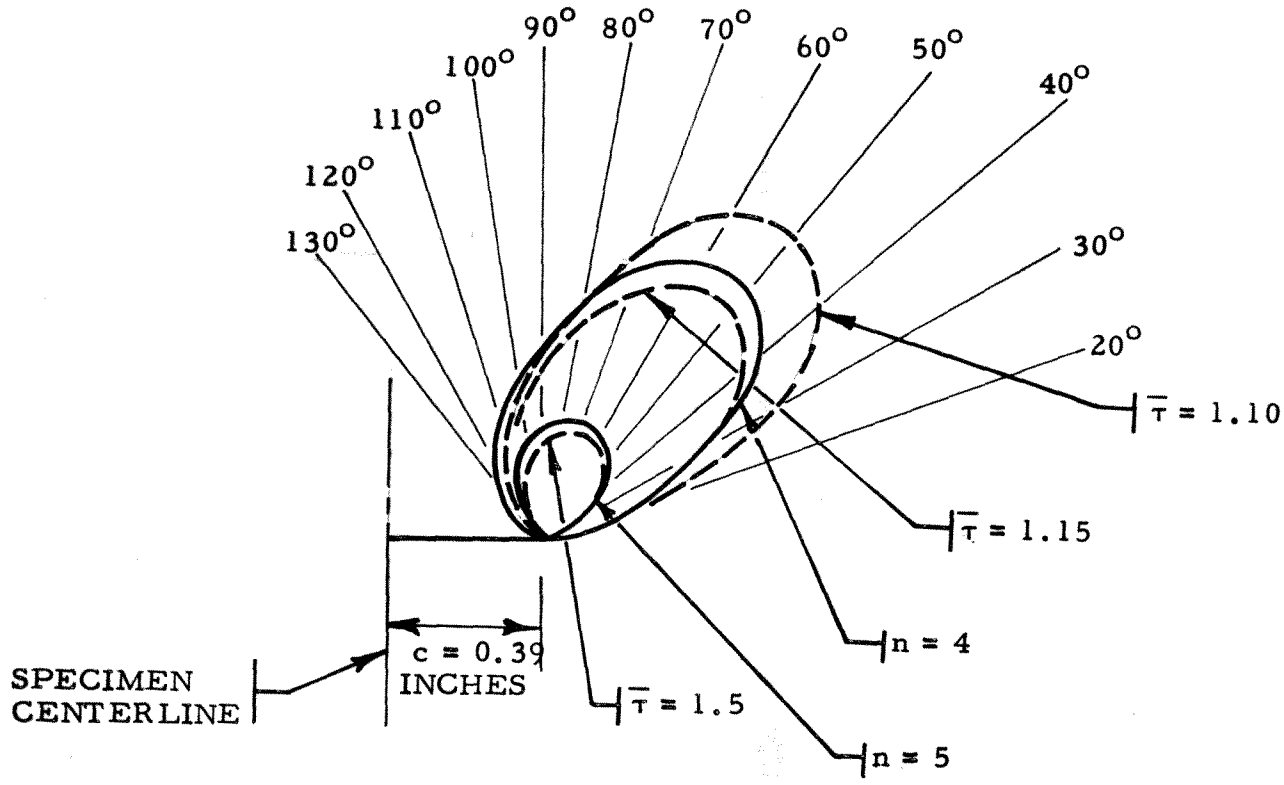

Figure 52. Comparison of Experimental and Theoretical Isochromatic Patterns for Test 112-6 (Solid Lines are Experimental Data - n = Fringe Order. Dotted Lines are Theoretical Curves for Static Loading of Plate with Stationary Crack (Ref. 23).

$$\bar{\tau} = \frac{\epsilon_1 - \epsilon_2}{\bar{\epsilon}_y} = \frac{\sigma_1 - \sigma_2}{\bar{\sigma}_y}$$. See Figure 36a.

t = 1.390 seconds, v = crack velocity = 0.09 in/sec

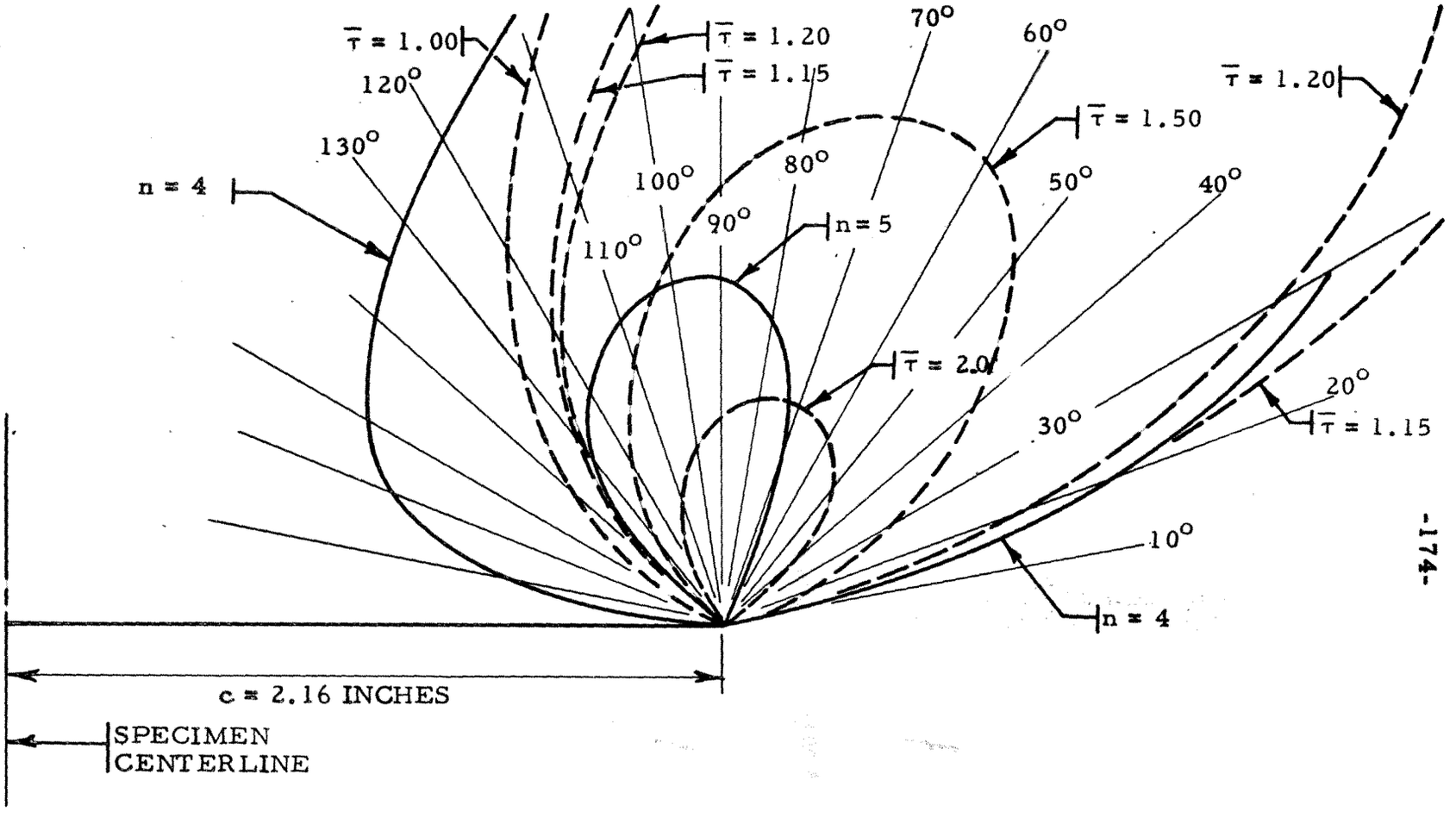

Figure 53. Comparison of Experimental and Theoretical Isochromatic Patterns for Test 112-6. (Solid Lines are Experimental Data; n = Fringe.Order. Dotted Lines are Theoretical Curves for Static Loading of Plate with Stationary Crack (Ref. 23); $\bar{\tau} = (\epsilon_1 - \epsilon_2)/\bar{\epsilon}_y$. See Figure 36b, Frame 9; t = 4.7535 seconds, v = 37.2 in/sec.

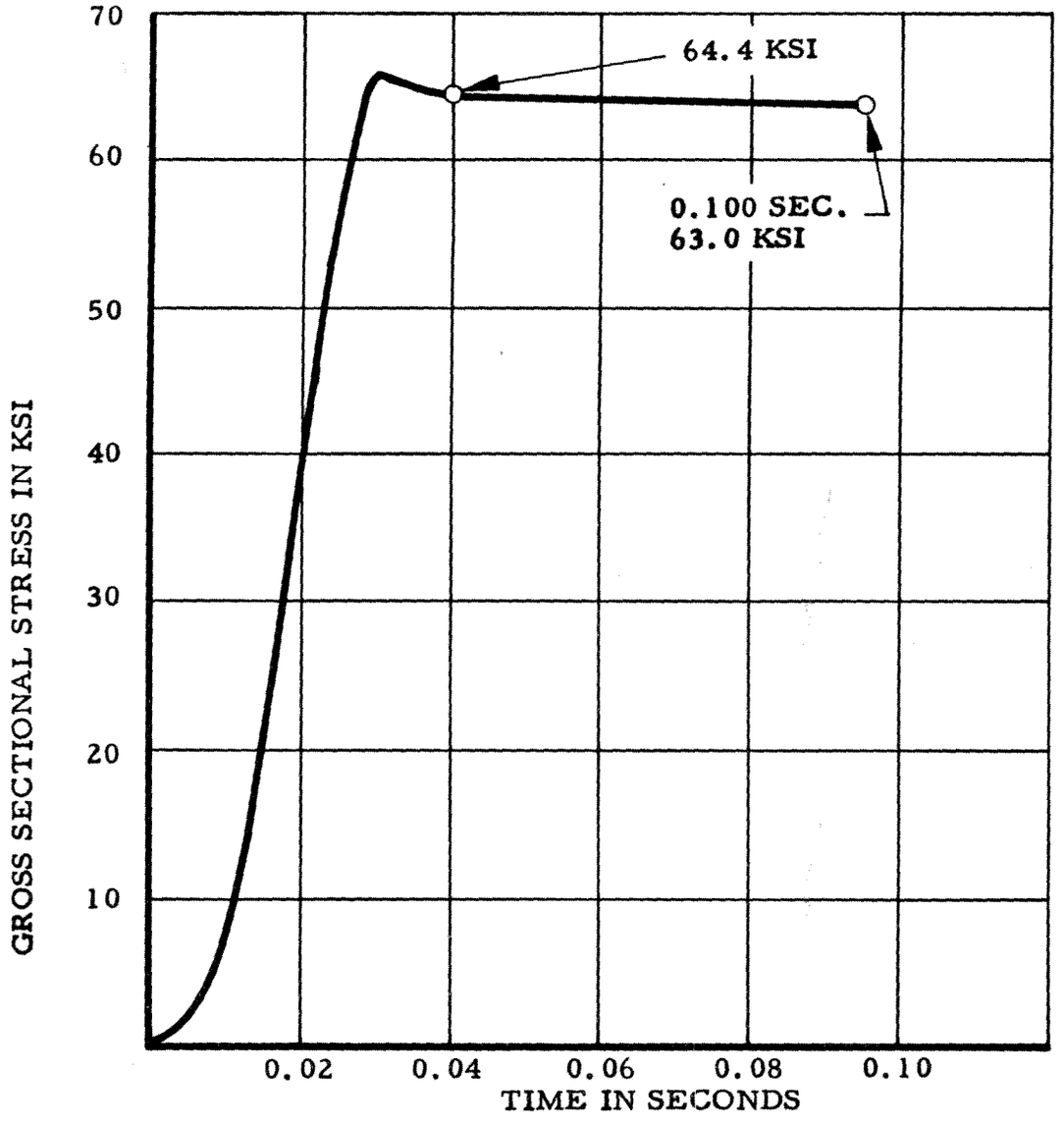

Figure 54a. Loading Curves for Silicon-Iron Test M-1

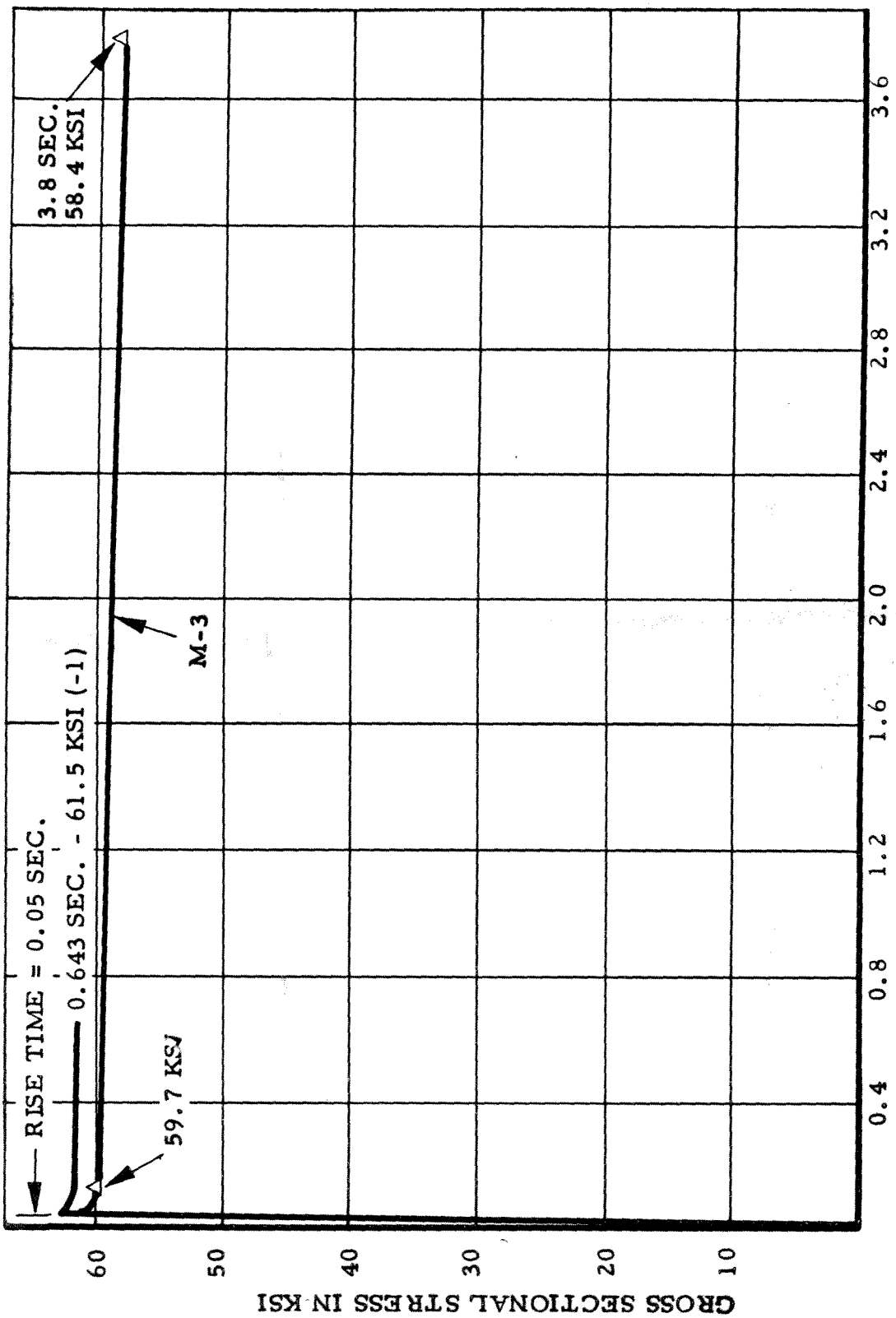

Figure 54b. Loading Curves for Silicon-Iron Tests M-2 and M-3

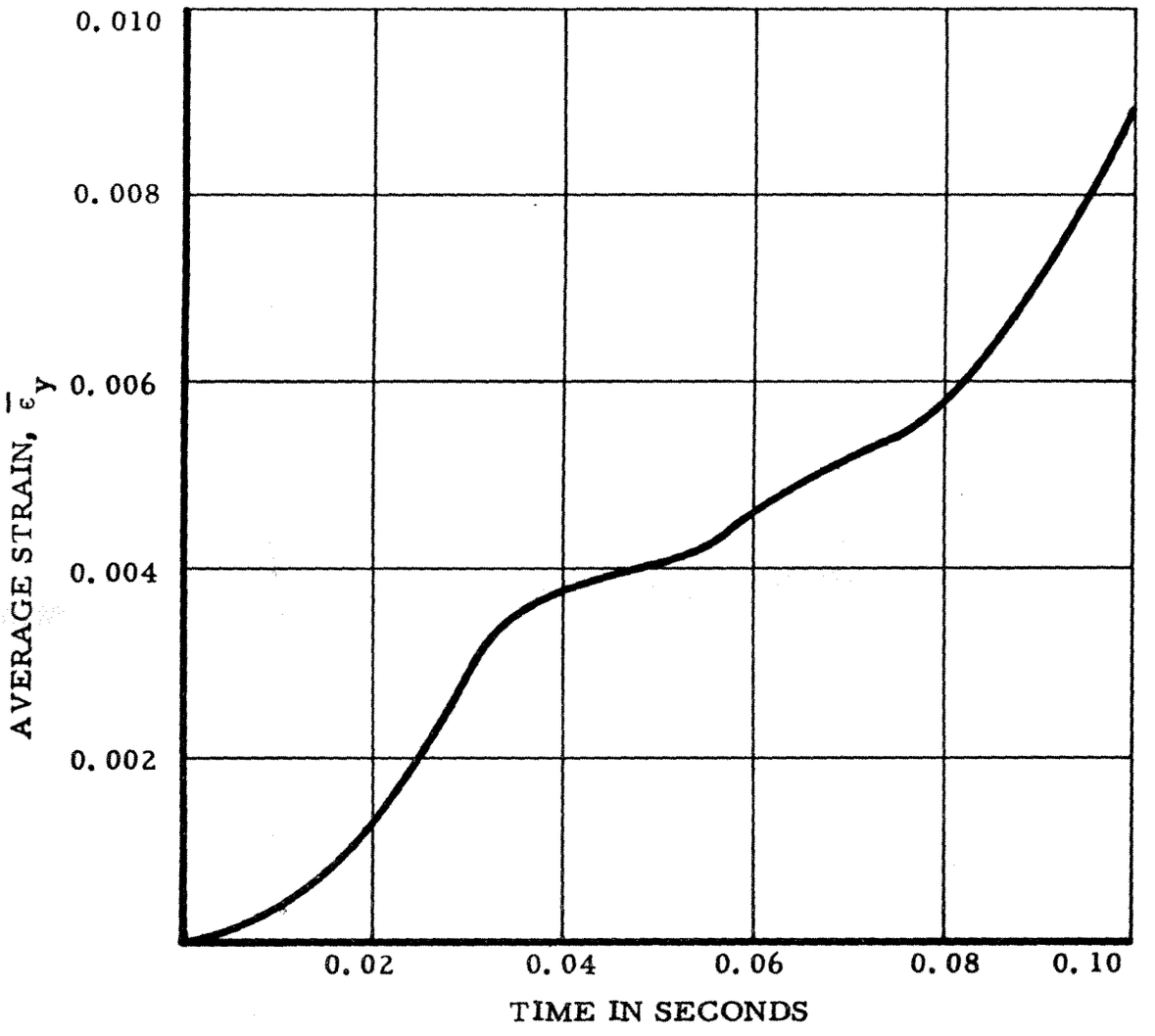

Figure 55a - Average Strain Curve for Test M-1
(Silicon-Iron)

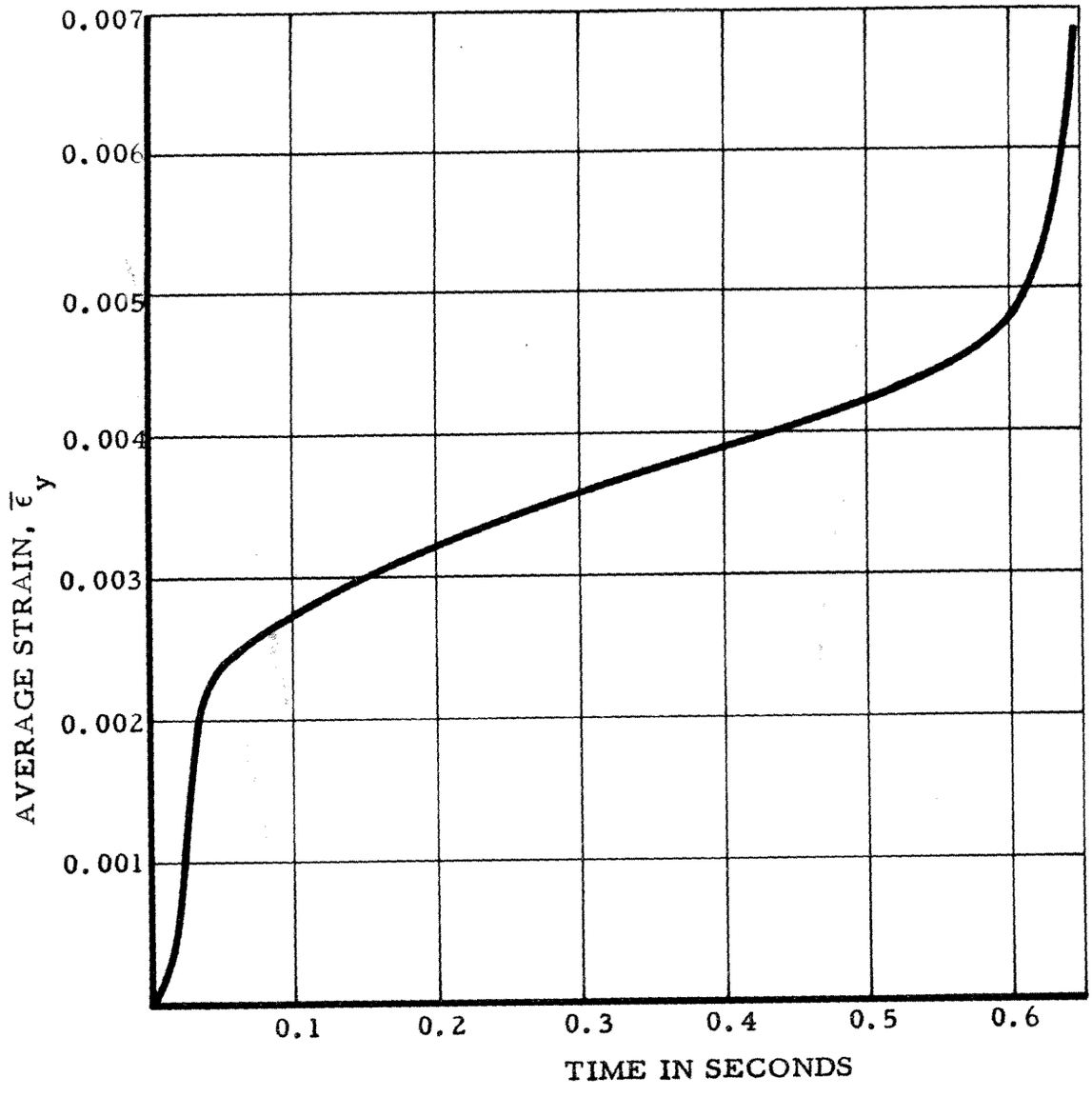

Figure 55b. Average Strain Curve for Test M-2 (Silicon-Iron)

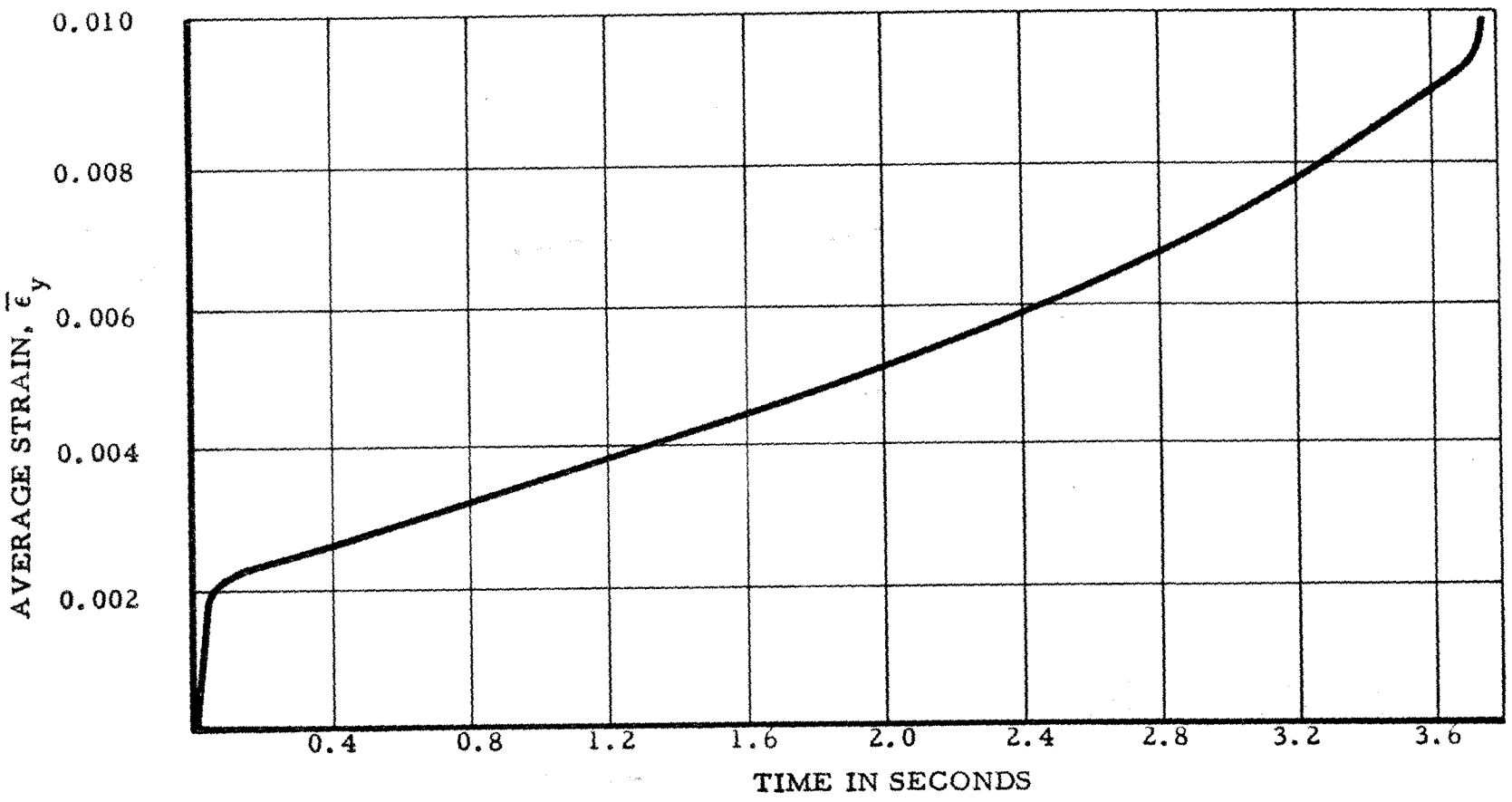

Figure 55c. Average Strain Curve for Test M-3 (Silicon-Iron)

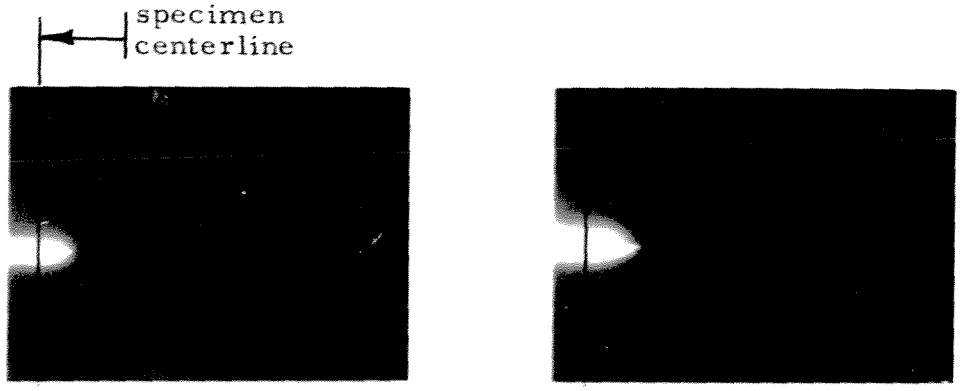

1. t = 0
   c = 0.350

2. t = 0.4940
   c = 0.600

3. t = 0.5470
   c = 0.925

4. t = 0.5602
   c = 1.400

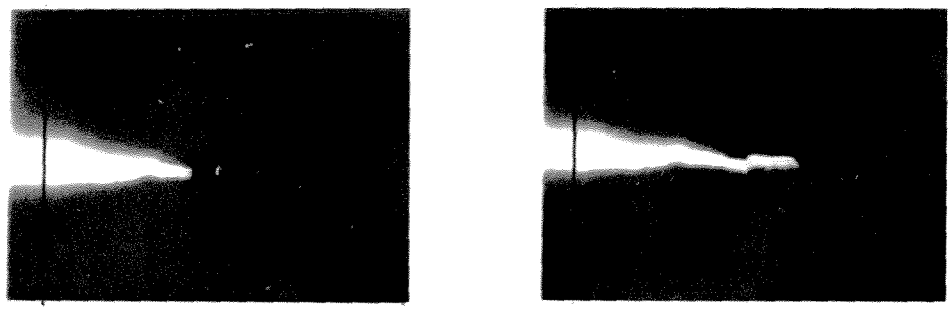

5. t = 0.5641
   c = 1.700

6. t = 0.5653
   c = 2.600

Figure 56a. Crack Propagation Photographs from Test M-2 (Silicon-Iron) (t in seconds, c in inches)

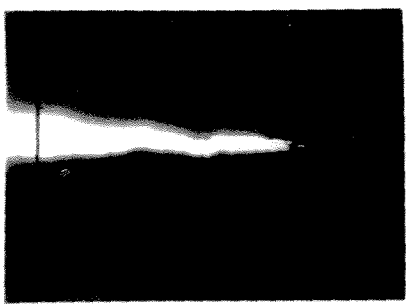

7. c = 3.150

t = 0.5673

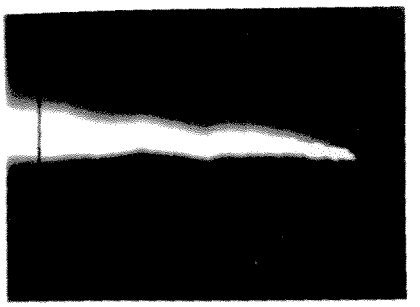

8. c = 3.625

t = 0.5689

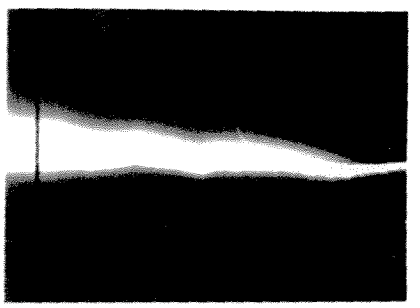

9. c > 4.00

t = 0.5692

Figure 56b. Crack Propagation Photographs from Test M-2 (Cont'd)

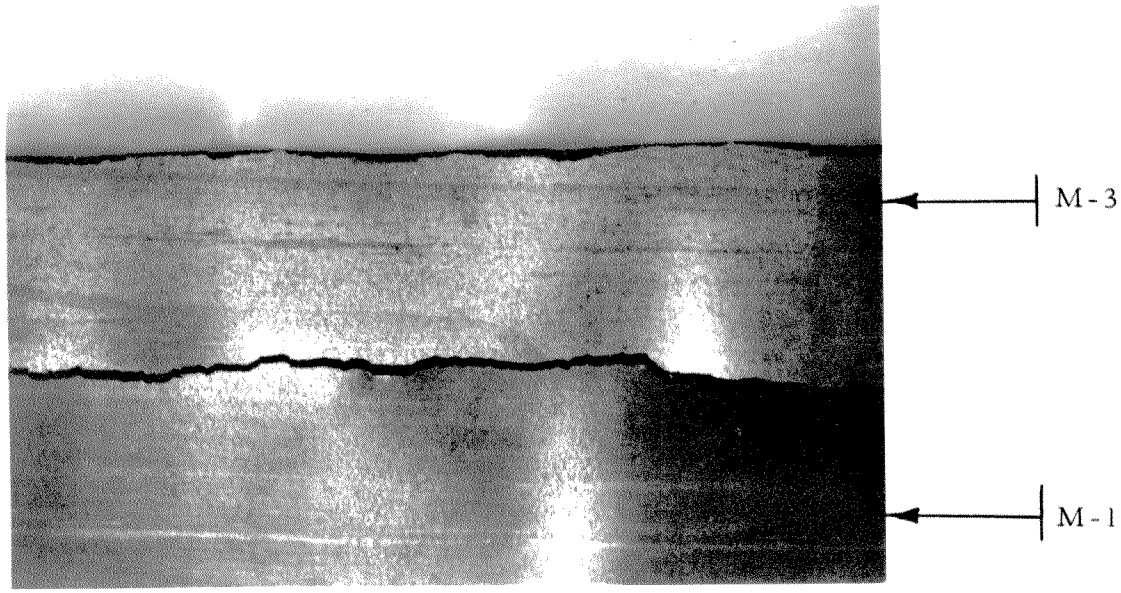

Figure 57. Side View of Fracture Surfaces from Test M-1 and M-3 (Silicon-Iron)

(a) Region where necking occurred

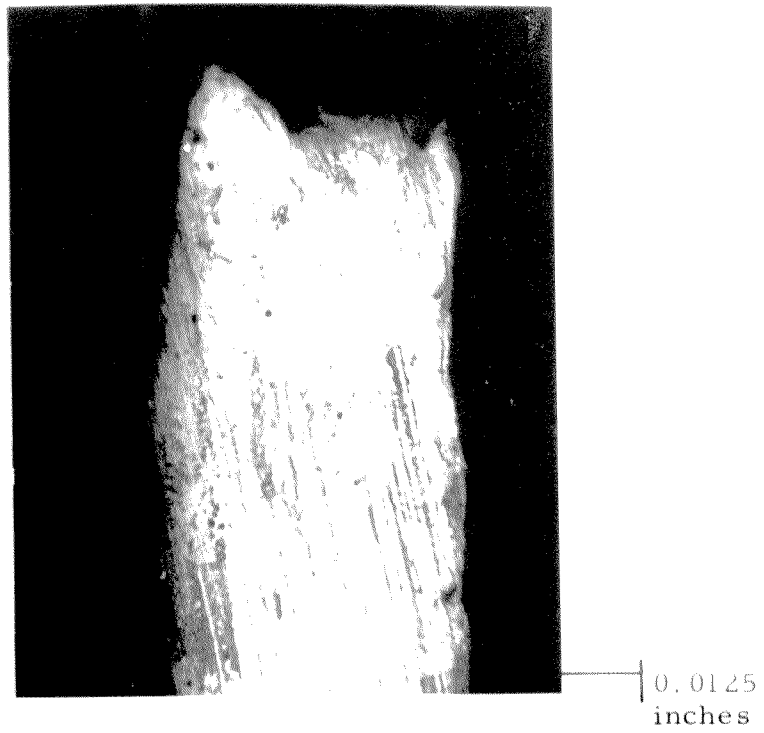

(b) Region of brittle type fracture - note that some deformation has occurred in thickness direction

Figure 58. Edge Views of Fracture Surfaces on Silicon-Iron Specimen Magnification 100x)

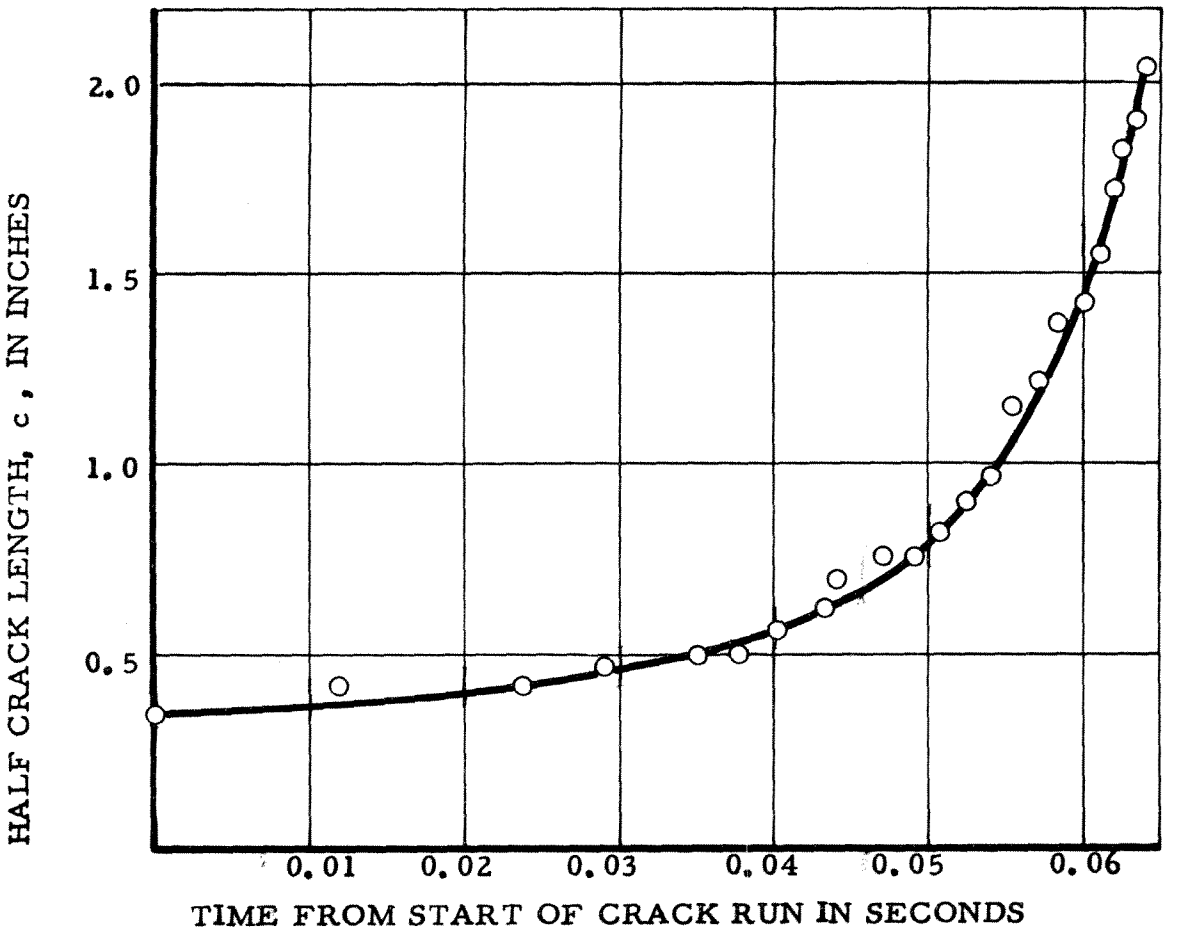

Figure 59a - Crack Length Versus Time Curve for Test M-1 (Silicon-Iron)

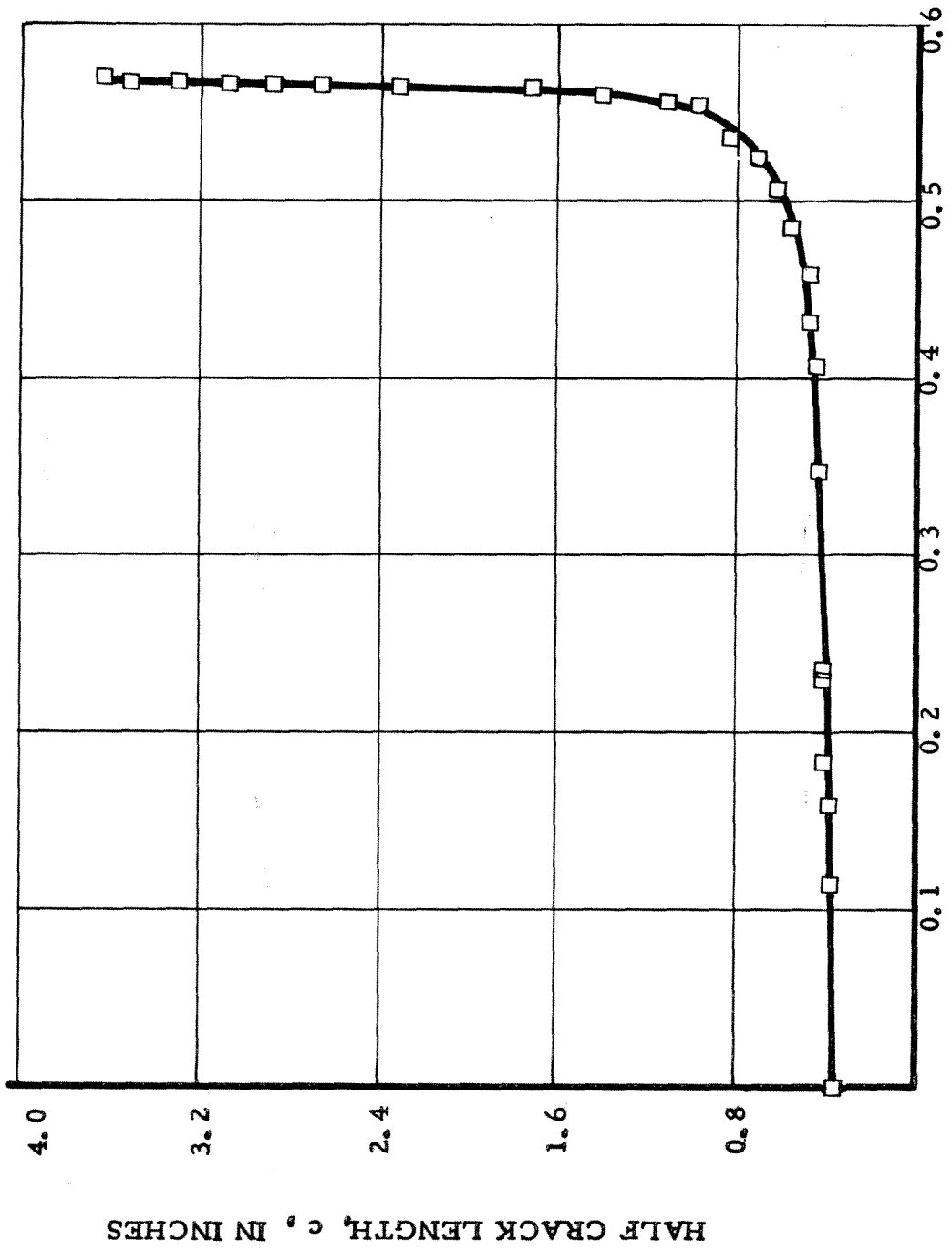

Figure 59b - Crack Length Versus Time for Test M-2 (Silicon-Iron)

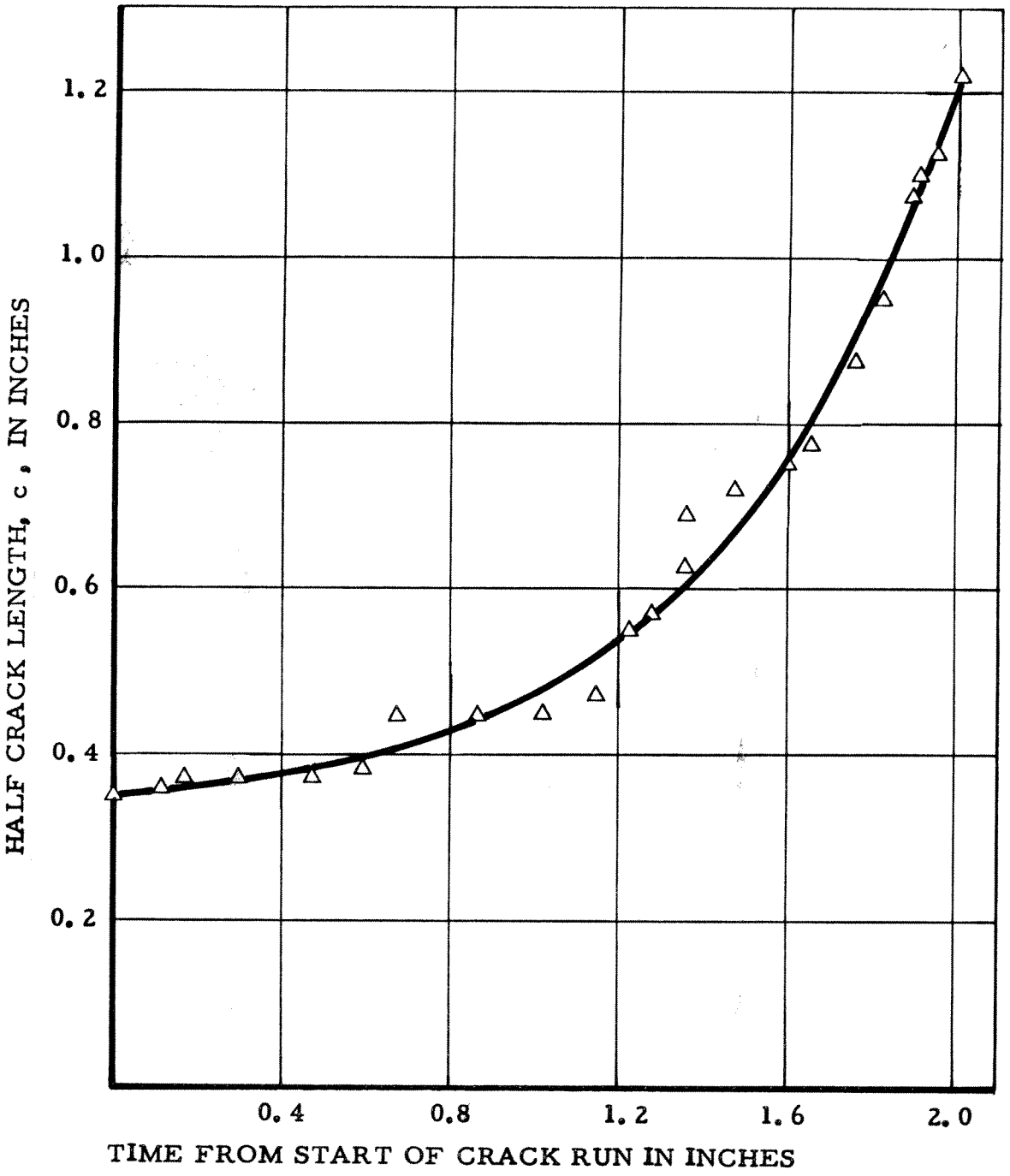

Figure 59c - Crack Length Versus Time for Test M-3 (Silicon-Iron)